



DEPARTMENT OF SCIENCE AND HUMANITIES  
(PHYSICS)  
INDIAN INSTITUTE OF INFORMATION  
TECHNOLOGY, DESIGN AND  
MANUFACTURING KANCHEEPURAM  
CHENNAI - 600127

**Synthesis, properties and applications of  
graphene oxide derivatives and their  
nanocomposites**

*A Thesis*

*Submitted by*

**T. ANUSUYA**

*For the award of the degree*

*Of*

**DOCTOR OF PHILOSOPHY**

May 2022



## QUOTATIONS

*In the history of science,  
we often find that, the study of  
some natural phenomenon has  
been the starting point in the  
development of a new branch of  
knowledge.*

C V RAMAN

# **DEDICATION**

*To my beloved  
Parents*

## **THESIS CERTIFICATE**

This is to undertake that the Thesis titled **SYNTHESIS, PROPERTIES AND APPLICATIONS OF GRAPHENE OXIDE DERIVATIVES AND THEIR NANOCOMPOSITES**, submitted by me to the Indian Institute of Information Technology, Design and Manufacturing Kancheepuram, for the award of Ph.D., is a bonafide record of the research work done by me under the supervision of Dr.Vivek Kumar. The contents of this Thesis, in full or in parts, have not been submitted to any other Institute or University for the award of any degree or diploma.

**Place: Chennai**

**Date:**

**T. Anusuya**

Research Scholar

**Dr. Vivek Kumar**

Research Guide

# LIST OF PUBLICATIONS

## I. REFEREED JOURNALS BASED ON THE THESIS

1. **T Anusuya**, Prakash J., Devesh K. Pathak, Kapil Saxena, Rajesh Kumar, Vivek Kumar, Porous graphene network from graphene oxide: Facile self-assembly and temperature dependent structural evolution, *Materials Today Communications* , 26, 101930, (2021).
2. **T Anusuya**, D. Prema, Vivek Kumar, Reduction controlled electrical conductivity of large area graphene oxide channel, *J Mater Sci: Mater Electron* , 33, 8935-8945, (2021).
3. **T Anusuya**, Veeresh Kumar, Vivek Kumar, Hydrophilic graphene quantum dots as turn-off fluorescent nanoprobe for toxic heavy metal ions detection in aqueous media, *Chemosphere* , 282, 131019, (2021).
4. **T Anusuya**, D.K. Pathak, Rajesh Kumar, Vivek Kumar, Deconvolution and quantification of defect types from the first order Raman spectra of graphene oxide derivatives, *FlatChem* , 35, 100422, (2022).

## II. UNDER REVIEW

1. **T Anusuya**, Vivek Kumar, Synthesis of porous reduced graphene oxide/nickel oxide (rGO/NiO) nanocomposite modified supercapacitor electrode for enhanced energy storage, *Under review*, (2022).

## III. REFEREED JOURNALS (Others)

1. Tanushree Ghosh, Suchita Kandpal, Manushree Tanwar, Devesh K. Pathak, Chanchal Rani, **T. Anusuya**, Vivek Kumar, Rajesh Kumar, and Anjali Chaudhary, Electrochemically reduced graphene oxide/nano- $WO_3$  composite-based supercapacitor electrodes for better energy storage *Eur. Phys. J. Spec. Top*, (2022)
2. Devesh K Pathak, Manushree Tanwar, Chanchal Rani, Suchita Kandpal, Tanushree Ghosh, Priyanka Yogi, **T Anusuya**, Puspen Mondal, Anjali Chaudhary, Vivek Kumar, Rajesh Kumar, Quantifying Size Dependent Electron Emission from Silicon Nanowires Array , *Silicon*. (2021).
3. Poudel, **T Anusuya**, K Saxena, R Kumar, V Kumar Back surface field approach and ITO/top electrode-based structural optimization of high efficient silicon solar cell *Advances in Materials and Processing Technologies*, 5, 338-347, (2019).

#### IV. PRESENTATIONS/PUBLICATIONS IN CONFERENCES BASED ON THE THESIS

1. **T Anusuya** and Vivek Kumar, Low temperature reduction with tuned electrical conductance of porous graphene oxide film: Correlating electrical conductance, *7th International Conference on Nanotechnology for Better Living*, (2021)
2. **T Anusuya**, Prakash J and Vivek Kumar, Structural evolution and defect study of thermally derived reduced graphene oxide, *17th International conference series on Advanced Nano Materials* , 258, (2021)
3. **T Anusuya** and Vivek Kumar, Three dimensionally delaminated reduced graphene oxide-nickel oxide porous hybrid structure for supercapacitor application, *8th Interdisciplinary symposium on Material chemistry* , 395, (2021)
4. **T Anusuya** and Vivek Kumar, Investigation on the synthesis of porous graphene network for energy application, *International Conference on Nanomaterials* (2021)
5. **T Anusuya**, Veeresh Kumar, Renu Pasricha and Vivek Kumar, Graphene quantum dots based optical nanosensor for detection of heavy metal ions, *6th International Conference of Nanoscience and Nanotechnology*, 289, (2021)
6. **T Anusuya**, K. Venkatesan, Rajesh Kumar and Vivek Kumar, Evolution of electrical conductance of low temperature reduced graphene oxide thin film, *6th International Conference of Nanoscience and Nanotechnology*, 281, (2021)
7. **T Anusuya** and Vivek Kumar, Raman microscopy of Graphene oxide under thermal reduction: Spectral analysis and structural information *6th International conference on Advanced Nanomaterials and Nanotechnology*, 143, (2019).

## ACKNOWLEDGEMENTS

I would like to express my deepest gratitude to my thesis supervisor **Dr. Vivek Kumar** for allowing me to pursue research under his supervision. His friendly demeanour, patience, and knowledge have been inspirational for me. His insightful feedback pushed me to upgrade my technical skills, sharpen my thinking, and bring my work to the next level. The intellectual freedom I have got working under him is the greatest gift of my research life. I cordially thank him for providing me with such an unparalleled gift.

I deeply thanks my doctoral committee chairman **Dr. Tapas sil** and members **Dr. Anushree P Khandale, Dr. Jayachandra Bingi** and **Dr. Gowthaman Swaminathan** for their regular feedback which strengthens my research outcomes. I would also like to express my gratitude for the financial support of half-time teaching research assistantship (HTRA) provided by the institute management through the Ministry of Human Resource Development (MHRD), Govt of India.

I thank my co-scholars Mr.Karthick Raja, Mr. Harishankar, Mr.Pritam Shetty, Ms. Hemalatha and Mr. P. V. Karthik Yadav for their constant support and encouragement. I want to express my heartfelt gratitude to them alongside Mr.Rajasekar and Mr. Chandrasekar for their selfless knowledge transfer on LaTeX technical writing software which was more helpful during my thesis writing.

Mere words are not sufficient to describe the support of my entire family. I express my heartfelt thanks to my father Mr. S. Thangaraj, mother Mrs. A. Esther Manorathy, mother-in-law V. Meenakumari Gopinath, brother Mr. T. Arun and sister Ms. T. Sumathy for their support and blessings. I wish to thank my husband Mr.G. Devanand Venkatasubbu and my son G. Siddharth Prabakaran for their enduring love, care, patience and support during research. Their wish for me to pursue the highest education inspired me to pursue my research into energy and power.



## ABSTRACT

**KEYWORDS:** Graphene; Graphene oxide; Porous graphene; Reduced graphene oxide; Thermal reduction; Electrical conductivity; Defects; Raman spectroscopy; rGO/NiO Nanocomposites, Energy storage devices, Graphene quantum dots; Optical nanosensor; Fluorescence quenching; Toxic heavy metal ions.

Graphene family materials such as, graphene oxide (GO), reduced graphene oxide (rGO) and graphene quantum dots (GQD) are extensively studied due to their fascinating properties such as larger surface area, surface functionalities, tunable bandgap, enhanced electrical and optical properties. These fascinating properties find many applications in various fields like energy storage, sensing, water purification, biomedical and so on. In this thesis work, GO was synthesized by chemical exfoliation of graphite through modified Hummer's method. Thermal reduction of GO was carried out to improve the physiochemical characteristics of GO through de-oxygenation and restoration of  $\pi$  conjugation. Further, the reduction temperature was optimized to obtain the porous graphene network (PGN) like structure. The surface morphology and structural transformation of GO during oxo-reduction stages are analysed. This work highlights a simple and template free method to synthesize PGN compared to conventional template assisted techniques. Further, a simple method to get the conductive rGO film and a method to analyze the electron transport behaviour is achieved. The gradual and controllable thermal reduction of GO film formed by drop-casting method was carried out. Here, the role of functional groups on the evolution of electrical conductance during reduction has been investigated by correlating the IR modes and electrical conductivity. This method enables one to control the electrical conductance of rGO by simply controlling the degree of reduction.

Furthermore, the first order Raman scattering has been employed to study the structural modifications and quantification of defect types in GO and thermally reduced GO.

The integrated Raman G and D peak intensities of GO and rGO annealed at different temperature with the intermixed (0D and 1D) defect density are analyzed with the theoretical defect diagram to extract information about the nature of defects and defect density over the structural evolution. This method provides a new insights to analyse the Raman scattering to study defects.

The synthesized rGO showed better conductivity and interconnect network, that provides an opportunity to synthesize the nanocomposites of three dimensionally interconnected rGO/nickel oxide (NiO) as electrode material for a enhanced electrochemical energy storage applications. The as synthesized nanocomposites of rGO/NiO with different weight percentage of rGO were analyzed. The incorporation of rGO increases the conductivity of bare NiO electrode by providing a interconnect network structure and thereby helps the transport of charge carriers. The enhancement in the electrochemical performance of rGO/NiO modified electrode exhibits this as a promising material for energy storage applications.

Further, the GQDs , a quasi zero dimensional GO derivative were synthesized from GO by hydrothermal method. Here, the hydrophilic GQD has been employed to devise an optical nano-sensor for the detection of toxic heavy metal ion. The metal ions of  $Hg^{2+}$ ,  $Cd^{2+}$  and  $Pb^{2+}$  showed a turn-off fluorescence effect upon coordinating with the surface functionalities of GQDs. The observed PL was analyzed by the Stern-Volmer equation to study the fluorescent quenching mechanism of the system. Nonlinear behavior of Stern-Volmer plot suggests that the reduction in fluorescent intensity is due to the combination of dynamic and static processes. This study shows the viability of GQD as a promising material for heavy metal ions sensing in aqueous solution. The GO derivatives and composites obtained in this present work, with the improved structural and electrical properties are highly capable of replacing the existing functional materials in distinct applications.

# TABLE OF CONTENTS

	<b>Page</b>
<b>ACKNOWLEDGEMENTS</b> . . . . .	i
<b>ABSTRACT</b> . . . . .	ii
<b>LIST OF TABLES</b> . . . . .	viii
<b>LIST OF FIGURES</b> . . . . .	xi
<b>ABBREVIATIONS</b> . . . . .	xiii
<b>NOTATION</b> . . . . .	xv
<b>CHAPTER 1: INTRODUCTION</b> . . . . .	1
1.1 Motivation . . . . .	4
1.2 Objective of present work . . . . .	6
1.3 Scope of the work . . . . .	7
1.4 Organization of work . . . . .	8
1.4.1 Synthesis of GO, rGO and electrical Properties . . . . .	9
1.4.2 First order Raman scattering to analyse defects in GO and rGO	10
1.4.3 rGO/NiO nanocomposite: synthesis and electrochemical prop- erties . . . . .	11
1.4.4 Synthesis of GQDs from GO and sensing application . . . . .	12
1.5 Summary and Conclusions . . . . .	12
<b>CHAPTER 2: Basic concepts and experimental techniques</b> . . . . .	14
2.1 Graphene based nanostructures and classification . . . . .	14
2.1.1 Graphite . . . . .	14
2.1.2 Graphene . . . . .	15
2.1.3 Graphene oxide . . . . .	18
2.1.4 Reduced graphene oxide . . . . .	19

2.1.5	Graphene quantum dots . . . . .	20
2.2	Synthesis methods of graphene oxide and derivatives . . . . .	21
2.2.1	Chemical oxidation of GO . . . . .	21
2.2.2	Brodie and Staudenmaier method of GO oxidation . . . . .	21
2.2.3	Modified Hummmer's method of GO synthesis . . . . .	22
2.2.4	Reduction of graphene oxide . . . . .	24
2.2.5	Thermal reduction of GO . . . . .	24
2.2.6	Chemical reduction of GO . . . . .	25
2.2.7	Synthesis of graphene quantum dots . . . . .	26
2.3	Defects in GO derivatives . . . . .	27
2.3.1	Vacancy defects . . . . .	27
2.3.2	Stone-Waals's defects . . . . .	29
2.3.3	Grain boundaries and line defects . . . . .	29
2.4	Experimental techniques . . . . .	30
2.4.1	X-ray diffraction . . . . .	30
2.4.2	Fourier transform infrared spectroscopy . . . . .	31
2.4.3	X-ray photoelectron spectroscopy . . . . .	32
2.4.4	Scanning electron microscope . . . . .	32
2.4.5	Transmission electron microscope . . . . .	33
2.4.6	Raman Scattering . . . . .	34
2.4.7	Cyclic voltammetry analysis . . . . .	37
<b>CHAPTER 3: Synthesis of GO, rGO and electrical properties . . . . .</b>		<b>38</b>
3.1	Introduction . . . . .	38
3.2	Synthesis and thermal reduction of GO . . . . .	40
3.2.1	Synthesis of GO . . . . .	40
3.2.2	Thermal reduction of GO . . . . .	41
3.2.3	Structural modification and surface morphology during reduction . . . . .	41
3.3	Electrical conductivity of rGO: effect of thermal reduction . . . . .	47
3.3.1	Experimental details . . . . .	48
3.3.2	Electical conductivity: Result and Discussion . . . . .	49

3.4	Conclusion . . . . .	57
<b>CHAPTER 4: First order Raman scattering to analyse defects in GO and rGO. . . . .</b>		<b>58</b>
4.1	Introduction . . . . .	58
4.2	Experimental method . . . . .	60
4.2.1	Synthesis of graphene Oxide . . . . .	60
4.3	Results and Discussion . . . . .	61
4.3.1	Structural analysis . . . . .	61
4.3.2	X-ray photoelectron spectroscopy . . . . .	64
4.3.3	Raman scattering . . . . .	65
4.4	Conclusions . . . . .	77
<b>CHAPTER 5: rGO-NiO nanocomposite: synthesis and electrochemical properties . . . . .</b>		<b>79</b>
5.1	Introduction . . . . .	79
5.2	Synthesis of rGO/NiO nanocomposite . . . . .	81
5.3	Preparation of rGO/NiO modified electrode . . . . .	82
5.4	Result and Discussion . . . . .	83
5.4.1	X-ray diffraction analysis . . . . .	83
5.4.2	Scanning electron microscopy . . . . .	84
5.4.3	Brunauer-Emmett-Teller analysis . . . . .	85
5.4.4	Electrochemical analysis . . . . .	87
5.4.5	Electrochemical impedance spectroscopy analysis . . . . .	94
5.5	Conclusion . . . . .	96
<b>CHAPTER 6: Synthesis of GQDs from GO and sensing application . . . . .</b>		<b>97</b>
6.1	Introduction . . . . .	97
6.2	Experimental method . . . . .	99
6.3	Result and discussion . . . . .	100
6.4	Conclusion . . . . .	109
<b>CHAPTER 7: CONCLUSIONS AND FUTURE SCOPE . . . . .</b>		<b>110</b>
7.1	Conclusion . . . . .	110

7.2 Future Scope . . . . .	112
<b>REFERENCES . . . . .</b>	<b>135</b>

## LIST OF TABLES

<b>Table</b>	<b>Title</b>	<b>Page</b>
4.1	$L_a$ and $L_D$ values calculated using eqn 4.7 as extracted with the aid of Figs. 4.6 and 4.7 for in samples S1 to S5 . . . . .	77
5.1	Comparison of specific capacitance values of rGO/Metal oxides based electrodes for efficient energy storage in supercapacitor . . . . .	92
6.1	Comparison of limit of detection (LoD) of quantum dots based sensor for $M^{2+}$ detection. . . . .	106

## LIST OF FIGURES

Figure	Title	Page
2.1	Schematic representation of graphite crystalline structure . . . . .	14
2.2	(a) Schematic representation of unit cell in graphene lattice (b) The Brillouin zone of graphene unit cell . . . . .	16
2.3	Schematic representation of energy band structure of single layer graphene lattice with zero band gap at the Dirac point . . . . .	17
2.4	Schematic representation of Lerf and Klinowski (L-K) model of GO structure . . . . .	19
2.5	Schematic representation of density of states (DOS) of GO and rGO structure . . . . .	20
2.6	Schematic representation of GO synthesis using modified Hummer's method . . . . .	23
2.7	Schematic representation of defective GO lattice (a) Vancancy (b) Stone-Waals's and (c) Grain boundary defect . . . . .	28
3.1	The XRD patterns of GO (S1) and rGO samples at 200 °C (S2), 300 °C (S3), 400 °C (S4) and 500 °C (S5). . . . .	43
3.2	SEM micrographs of Graphite (S0), GO (S1) and rGO reduced at 200 °C (S2), 300 °C (S3), 400 °C (S4) and 500 °C (S5). . . . .	44
3.3	Raman spectra of GO (S1) and rGO reduced at 200 °C (S2), 300 °C (S3), 400 °C and 500 °C (S5). . . . .	45
3.4	Temperature Vs Peak intensity ratio of D and G peak for GO (S1) and rGO annealed at reduction temperature of 200°C, 300 °C (S3), 400 °C (S4) and 500 °C (S5). . . . .	46
3.5	IV Characteristics of GO (S1) at room temperature and rGO annealed at 100 °C (S2), 150 °C (S3), 200 °C (S4), 250 °C (S5), 300 °C(S6) and 350 °C (S7) . . . . .	50
3.6	I-V Characteristics of rGO at fixed temperature of ramped down from 350 °C to 35 °C during cooling cycle. . . . .	51
3.7	HRTEM images of rGO at different reduction temperature: a and b high resolution (001) lattice plane images of rGO reduced 100 and 150 °C (S2 and S3) and c-f high resolution (002) lattice plane image of rGO reduced 200 °C (S4), 250 °C (S5), 300 °C(S6) and 350 °C (S7) . . . .	52
3.8	XPS spectra of GO at different annealing temperature: (a) survey spectrum of rGO @ 100 °C (S2), 150 °C (S3), and 350 °C (S7). High resolution deconvoluted C1s peak image of (b) rGO @ 100 °C (S2) (C and d) 150 °C (S3), and 350 °C (S7) . . . . .	54
3.9	FTIR spectra of as prepared GO (S1) and rGO @ 100 °C (S2), 150 °C (S3), 200 °C (S4), 250 °C (S5), 300 °C(S6) and 350 °C (S7) . . . . .	55



3.10	Correlative graph of electrical conductivity of GO/rGO channel and peak area of GO/rGO samples obtained from FTIR spectra with reduction temperature . . . . .	56
4.1	(a) The XRD pattern of GO (S1) and rGO samples at 200 °C (S2), 300 °C (S3), 400 °C (S4) and 500 °C (S5). (b) TGA curve of GO weight loss during the reduction process of GO in the temperature range of 30-600 °C in ambient conditions. (c) and (d) TEM images of GO (S1) and rGO at 500 °C (S5). . . . .	62
4.2	Deconvoluted C1s XPS spectra of (a) GO (S1) and (b) rGO reduced at 400 °C (S4), (c and d) XPS survey spectrum of GO (S1) and rGO reduced at 400 °C (S4). . . . .	64
4.3	First-order Raman spectra and fitted Raman peak of GO (S1) and rGO samples annealed at 200 °C (S2), 300 °C (S3), 400 °C (S4) and 500 °C (S5) . . . . .	66
4.4	Raman spectral behaviour of structural changes happened in graphene-based materials. $(A_D/A_G)*E_L^4$ as a function of $L_a$ and $L_D$ . The blue and red lines are the plots of equations 4.4 and 4.5 as a function of $L_a$ and $L_D$ , respectively. (b) $\Gamma_G$ as a function $L_a$ and $L_D$ using equation 4.6 . . . . .	71
4.5	(a) Integrated peak area $A_D/A_D*E_L^4$ as a function of G band spectral line width $\Gamma_G$ . (b) Schematic illustration of point defects and line defects in rGO sheets. (c) The scattered open symbols are data points obtained from experimental Raman spectra of GO (S1) and rGO samples at 200 °C (S2), 300 °C (S3), 400 °C (S4) and 500 °C (S5). (d) The inset graph shows the crystallite area ( $L_a^2$ ) Vs Defect density ( $\sigma$ ) in terms of $1/L_D^2$ of GO (S1) and rGO samples at 200 °C (S2), 300 °C (S3), 400 °C (S4) and 500 °C (S5). . . . .	73
4.6	Theoretical integrated Raman peak intensity ( $A_D/A_D*E_L^4$ ) as a function of G peak line width $\Gamma_G$ for different values of $L_a$ . The line connected by the symbols with different colour and shapes are obtained by numerical calculations by changing the $L_a$ value shown in the legend using the equation 4.7. . . . .	75
4.7	Theoretical integrated Raman peak intensity ( $A_D/A_D*E_L^4$ ) as a function of G peak line width ( $\Gamma_G$ ) for different values of $L_D$ . The line connected by the symbols with different colour and shapes are obtained by numerical calculations by changing the $L_D$ value shown in the legend using equation 4.7 . . . . .	76
5.1	The XRD patterns of NiO nanoflakes and rGO/NiO nanocomposites GN1,GN2 and GN3 at different proposition of rGO samples . . . . .	83
5.2	(a) The SEM image of NiO nanoflakes structure (b,c and d) rGO/NiO nanocomposites GN1,GN2 and GN3 at different proposition of rGO samples. . . . .	84
5.3	(a,b and c) EDS elemental mapping of GN1,GN2 and GN3 at different proposition of rGO samples.C-carbon element, O-Oxygen element and Ni-Nickel element . . . . .	85

5.4	$N_2$ adsorption-desorption isotherms of NiO nanoflakes structure and rGO/NiO nanocomposites GN1,GN2 and GN3 with different proposition of rGO samples. . . . .	86
5.5	Pore size distributions analysis using BJH data of NiO nanoflakes structure and rGO/NiO nanocomposites GN1,GN2 and GN3 with different proposition of rGO samples. . . . .	87
5.6	(a) The C-V curve of NiO nanoflakes and rGO/NiO nanocomposites GN1,GN2 and GN3 at different proposition of rGO samples at different scan rates from 10 to 100 mV/s with the increment of 20 mV/s. . . . .	88
5.7	(a) The C-V curve of NiO nanoflakes and rGO/NiO nanocomposites GN1,GN2 and GN3 at different proposition of rGO samples at the lower, higher, and highest scan rate of 10, 100 and 200 mV/s. . . . .	90
5.8	The variation in specific capacitance value at the different scan rates of 10, 20, 40, 60, 80 and 100 mV/sec for NiO and rGO/NiO nanocomposites (GN1, GN2 and GN3). . . . .	91
5.9	Nyquist plot of NiO and rGO/NiO (GN1,GN2 and GN3) electrodes. (inset shows the lower frequency region of the plot) . . . . .	95
6.1	(a) TEM image of GQDs (b) Lattice fringe image of as synthesized graphene quantum dots. Inset of 6.1(a) Size distribution of GQDs and inset of 6.1(b) FTIR spectra of GQDs. . . . .	101
6.2	Photoluminescence spectra of GQD in the presence of different concentration of (a) $Hg^{2+}$ (b) $Cd^{2+}$ (c) $Pb^{2+}$ (d) shows the schematic of fluorescence quenching. . . . .	102
6.3	Histogram shows the change in PL intensity with the increase of metal ion concentration for three different metal ions. Inset of the figure shows the PL intensity with different metal ion concentration. . . . .	103
6.4	Stern-Volmer plot for Intensity ratio with logarithmic concentration of GQDs with (a) Hg metal ion, (b) Cd metal ion and Pb metal ion. The open symbol represents the experimental point and solid line is the linear fit. . . . .	105
6.5	Schematic illustration of (a) GQDs synthesis process and (b) fluorescent quenching mechanism of the GQDs in presence of the metal ions . . . . .	108



## ABBREVIATIONS

<i>0D</i>	Zero dimensional
<i>1D</i>	One dimensional
<i>2D</i>	Two dimensional
<i>3D</i>	Three dimensional
<i>A</i>	Ampere
BET	Brunauer-Emmett-Teller
BJH	Barrett-Joyner-Halenda
<i>C</i>	Carbon
<i>Cd<sup>2+</sup></i>	Cadmium ion
<i>CO</i>	Carbon monoxide
<i>CO<sub>2</sub></i>	Carbon dioxide
<i>CO<sub>3</sub>O<sub>4</sub></i>	Cobalt oxide
<i>C-O</i>	Carbonyl
<i>C-O-C</i>	Epoxy
<i>COOH</i>	Carboxyl
DI water	Deionized water
EDLC	Electrical double layer capacitor
EDS	Energy dispersive X-ray spectroscopy
FTIR	Fourier transform infrared spectroscopy
<i>Fe<sub>3</sub>O<sub>4</sub></i>	Iron oxide
GO	Graphene oxide
GQD	Graphene quantum dot
<i>KMnO<sub>4</sub></i>	Potassium manganate
KOH	Pottasium Hydroxide
LoD	Limit of detection
<i>H<sub>2</sub>O</i>	Water molecule
<i>H<sub>2</sub>O<sub>2</sub></i>	Hydrogen peroxide
<i>H<sub>2</sub>SO<sub>4</sub></i>	Sulfuric acid

HCl	Hydrochloric acid
HRTEM	High resolution transmission electron microscopy
$Hg^{2+}$	Mercury ion
$M^{2+}$	Metal ion
$MnO_2$	Manganese oxide
NaOH	Sodium hydroxide
NiO	Nickel oxide
NiOOH	Nickel hydroxide
NMP	N-Methyl-2-pyrrolidone
OH	Hydroxyl
$OH^-$	Hydroxyl ion
$Pb^{2+}$	Lead ion
PGN	Porous graphene network
PL	Photoluminescence
PVDF	polyvinylidene difluoride
rGO	reduced Graphene oxide
$RuO_2$	Ruthium oxide
SC	Super capacitor
SEM	Scanning electron microscopy
$Sn_2O_5$	Stannic oxide
$V_2O_5$	Vanadium oxide
TCO	Transparent conducting oxide
TEM	Transmission electron microscopy
T-K	Tuinstra-Koenig
TGA	Thermogravimetric analysis
XRD	X-ray diffraction
XPS	X-ray photoelectron spectroscopy

## NOTATION

$^{\circ}C$	Degree celcius
$C_s$	Specific capacitance
$cm^3/g$	Cubic centimeter per gram
$DC$	Direct current
$eV$	electron volt
$d$	Interplanar distance
$L_c$	crystalline stack height
$n_c$	number of average Graphene layers in Graphene stack
$I$	Current
$E_L$	Energy of laser beam
$F/g$	Farad per gram
$g$	gram
$h$	hour
$L_a$	Crystallite size
$L_a^2$	Crystallite area
$L_D$	Distance between the point defect
$L_{D^2}$	Point defect density
$I_G$	Peak intensity of Raman G mode
$I_D$	Peak intensity of Raman D mode
$I_{D'}$	Peak intensity of Raman $D'$ mode
$K$	Scherrer constant
$ml$	milli liter
$mV/s$	milliVolt per second
$m^2/g$	square meter per gram
$nm$	nano meter
$R_s$	Solution resistance
$R_{ct}$	Charge transfer resistance
$S/cm$	Siemens/centimeter
$V$	Voltage
$W$	Warburg resistance
$Z$	Impedence
$\lambda$	Wavelength of X-rays
$\theta$	angle of diffraction
$\beta$	Full width half maximum
$\Gamma_G$	Line width of Raman G peak
$\Delta V$	Scan rate of potential window
$\Omega$	Ohm

# CHAPTER 1

## INTRODUCTION

The extensive study of carbon materials such as activated carbon, carbon nanotubes, fullerenes, graphene and derivatives such as GO, rGO and GQD has been carried out for the past few decades due to their simple processability, structural stability and ecofriendly properties. On owing to their unique properties they find significant applications in many fields like optoelectronic devices, flexible electronics, defence, agriculture, environmental sensing, water purification, biomedical and so on Savchak *et al.* (2018); Ramu *et al.* (2021); Ramesh *et al.* (2019); Munief *et al.* (2019); Akinwande *et al.* (2019); Iqra *et al.* (2022); Khaliha *et al.* (2021). Among all carbon allotropes, graphite is one of the most abundant and inexpensive material in nature. The graphite structure is made up of carbon atoms with  $sp^2$  hybridization as a form of two-dimensional (2D) sheets stacked with multiple layers and combined together by van der Waals forces. The economical and easily modifiable property of graphite allows this element for the synthesis of numerous graphene-based derivatives such as carbon nanotubes (CNT), fullerenes, graphene, GO, rGO and GQD for various industrial and societal needs.

Graphene is one of the modern-day carbon allotropes with the surprising and extraordinary physical, chemical and mechanical characteristics. A single layer graphene sheet has a young modulus of 1 TPa and an ultimate strength of  $> 100$  GPa. It possesses extreme thermal conductivity of more than  $5000$  W/m.K. The carrier mobility of exfoliated graphene sheets at room temperature is around  $200000$   $cm^2 V^{-1} s^{-1}$  Yang *et al.* (2018). These phenomenal characteristics of graphene greatly finds applications in many technologies like nanoelectronics, sensing, photovoltaic, energy storage and so on Schwierz (2010); Cao *et al.* (2021); Murugadoss *et al.* (2019). So, the isolation of graphene layer has initiated an immense interest in the area of graphene research to explore its exceptional properties. The most common methods to synthesize and isolate the graphene layers are the micro-mechanical exfoliation of graphite, epitaxial

growth, and chemical vapor deposition (CVD) Berger *et al.* (2006); Wang and Bocquet (2011); Kim *et al.* (2009). But the large-scale synthesis of graphene is still a real hurdle for researchers and industrial experts which restricts the usage of this material towards new inventions. However, it is compensated by the evolve of graphene-based derivatives such as GO, rGO and GQD that meets the expectations by the similar structural characteristics and simple fabrication techniques. These graphene based materials are often recognized by their size, surface functionalities, type and distribution of structural defects and dopants Tang *et al.* (2013).

The GO is a functional derivative of graphene. Their exceptional material characteristics arise due to the presence of  $sp^2$  carbon domains enclosed by  $sp^3$  domain. The distinct surface chemistry with the cost-effective mass synthesis process of GO has increased the interest on materials based on GO derivatives Brisebois and Sijaj (2020); Iqra *et al.* (2022). It has a unique structure of atomically thin and stacked 2D sheet with the existence of oxygenated functional groups such as hydroxyl (-OH), epoxy (C-O-C), carboxyl (-COOH) and carbonyl (C = O) attached over it as impurities. The polar oxygen functionalities improves the material solubility and bring hydrophilic nature to the GO structure. These  $sp^2/sp^3$  defective domain of GO provides a effective binding site for the adsorption of distinct analyze molecules and improvises the surface grafting ability of GO. During the oxidation processes, the random distribution of surface functionalities with the evolution of  $sp^3$  bond on the GO reduces the electrical conductivity by directing the conducting electron away from the basal plane of graphitic lattice. This makes the GO structure more insulating in nature with the lower electrical conductance of nearly  $0.4 \text{ Sm}^{-1}$  and energy band gap of  $\approx 3.5 \text{ eV}$  Aliyev *et al.* (2019); Dreyer *et al.* (2009). Tailoring the bandgap of GO significantly improves the electrical properties which can be assisted with the reduction of GO using different reduction techniques. The rejuvenation of C-C bonds and removal of oxygen groups during reduction stimulates the recovery of graphene characteristics on the GO lattice.

The rGO sheets can also be called as chemically, electrochemically or thermally modified graphene because it features the characteristics of graphene Chen *et al.* (2016a). The unique structural morphology, large specific surface area and good chemical stability make rGO as a prominent material for various applications. Due to the ultra-small



thickness, intrinsic charge mobility and transparency of rGO they are very much contributing in the making of MEMS and NEMS devices Mao *et al.* (2012). As well as, the three dimensional porous reduced GO network with enhanced porosity and structural diversity are very much useful in energy storage, chemical adsorbent and sensing devices such as batteries, supercapacitors, chemical and bio sensors Whitby (2014); Smith *et al.* (2019); Tian *et al.* (2021). The rGO in combined with other materials as rGO/polymer, rGO/metal and rGO/transition metal oxides/transition metal chalcogenides shows great potential in many fields as photo and electrocatalysts by improving the catalytic activity and useful in several applications such as energy storage, dye degradation, water purification, sensing and so on. Sachdeva (2020).

The GQDs are the fragments of graphene with the size of nanometer (nm). The remarkable physicochemical characteristics of GO derivatives like tunable bandgap, quantum confinement, edge effects, surface functionalization and hydrophilicity renders an exceptional opportunity to fabricate nanoscale devices in various technological fields. In general GQDs are considered as a zero-dimensional (0D) GO based conjugated structure with the average size of less than 100 nm. Also GQDs dots are functionalized with oxygen functional groups like OH, C-O-C, COOH and C=O due to the oxidation process. The band gap of the GQD can be tailored and modified by the rearrangement of the surface functionalities which helpful in the improvement of light absorption and optical properties of the material. The distinct photoluminescent mechanism with the edge effect, quantum confinement effect, surface state emission, molecular state emissions are specifically offered by the unique molecular structure of GQDs. With the exceptional properties of high stability, low toxicity, hydrophilicity, high quantum yield and biocompatibility, the GQDs are becoming an alternative to the existing toxic semiconductor quantum dots.

In this present study, the improved material characteristics of GO derivatives finds more applications in the field of energy storage Askari *et al.* (2020), sensing Baig *et al.* (2021), photovoltaic Wen *et al.* (2022), biomedical Lee *et al.* (2021), flexible and optoelectronics Iqra *et al.* (2022) and so on. Understanding the different synthesis methodologies and physicochemical properties of the GO derivatives will expands the future perspective and facilities to bring it towards advanced quantum technologies. Defec-

tive graphene structures have also attracted significant attention in energy storage and conversion as an effective electrode material. Porous graphene nanostructures facilitate the ion transport behaviour with wider conductive network that considerably enhances electrochemical energy storage Liu *et al.* (2020b). Defect engineering of graphene oxide based modified electrocatalyst sufficiently enhances the amount of active site and improves the accessibility of electrolyte ions Zhang and Lv (2018). The presence of defects on GO based biodevices with increased adsorption sites are highly required to dock the biomolecular structures like DNA Kumar *et al.* (2020), protein and drug molecules on graphene. This will play a major role in biosensors Haghayegh *et al.* (2022), tissue engineering Seonwoo *et al.* (2022) and cancer therapy Kalkal *et al.* (2020).

## 1.1 Motivation

The conventional methods of rGO synthesis like chemical, electrochemical, high temperature thermal reduction and laser ablation etc includes the usage of toxic chemicals and hazardous bi-products, high temperature process techniques, longer reduction time, requirement of highly equipped laboratory and instruments which impedes the production of rGO at a larger scale Savchak *et al.* (2018); Chen *et al.* (2016a); Shi *et al.* (2019); McAllister *et al.* (2007); Aminuddin Rosli *et al.* (2021). The low temperature thermal reduction at ambient condition is still unexplored and highly suitable for the industrialization of rGO based products. The strategy of rGO reduction at the ambient condition renders substantial advantages in achieving restored graphene structure with lesser annealing time and temperature than other techniques. Understanding the defect evolution during the oxo-reduction stages of GO helps to unveil the new insights on the GO based structures and their properties. These defective reduced GO structures are capable of improving the device performance with their improved physicochemical characteristics in various field including sensors and energy storage. The existing research gaps which motivates the present thesis work are given as follows.

Few layer rGO sheets are considered as a valuable alternative to single layer graphene due to their simplicity in the fabrication methods with mass production towards practical applications. In a few rGO structures, experimentally obtainable surface area is far

below the theoretical value due to the strong  $\pi$ - $\pi$  stacking and Vander Waals interactions between graphene tends to aggregation of GO the sheets Baig *et al.* (2021) . To overcome this problem and to achieve higher surface area, graphene porous structures have received increasing interest due to their unique morphology with interconnected networks, high surface area and high pore volume. The conventional method of PGN synthesis with the template assisted and template free techniques possess a main disadvantage of expensive methodology and low yield with the template residues as impurities Zhou *et al.* (2020) Abdolmohammadi and Afsharpour (2021) . So, the major challenge in developing a PGN structure with low reaction temperature, template free, chemical free and ecofriendly techniques can be achieved through the method of thermal reduction. A effective method to understand the rGO conductivity in analogy to the variation in the infrared modes of rGO is achieved in this research work.

The identification and quantification of defect types are often determined with the aid of Raman peak intensity values as reported earlier Tuinstra and Koenig (1970); Lucchese *et al.* (2010); Eckmann *et al.* (2012). Up to now researchers apply following proposed relation eqn 4.1 and 4.2 to understand the different types of defects (point( $L_D$  and line( $L_a$ ) present in GO/ rGO Tuinstra and Koenig (1970),Cançado *et al.* (2006) Lucchese *et al.* (2010).

$$\frac{A_D}{A_G} = \frac{560}{(E_L)^4} X \frac{1}{(L_a)} \quad (1.1)$$

$$\frac{A_D}{A_G} = \frac{4300}{(E_L)^4} X \frac{1}{(L_D)^2} \quad (1.2)$$

But in Raman spectra of GO both kind of defects will be present at the same time since it is inherent. Thus, by applying above relations, it will give an over/ under estimation of final conclusions. To avoid this, we have taken the contribution of both type of defects as shown in eqn 4.3 at the same time in the first order Raman spectra and analysed the experimental data. Cançado *et al.* (2017).

$$\left(\frac{A_D}{A_G}\right) E_L^4 = \left(\frac{A_D}{A_G}\right)_{0D}^{(s)} + \left(\frac{A_D}{A_G}\right)_{1D}^{(s)} + \left(\frac{A_D}{A_G}\right)_{0D,1D}^{(A)} \quad (1.3)$$

This work will provide a new insight in field of GO and other 2D related materials for further enhancement of material quality and integrating into the device.

Metal oxide nanostructures like NiO are highly preferred as an efficient supercapacitor electrode material due to its high theoretical capacitance, larger availability, nontoxicity and physicochemical stability. The intrinsic electrical conductivity and surface active sites of NiO nanostructures could be tailored to improve the electrochemical performance as reported by Z J le et.al Li *et al.* (2018). This can be overcome by synthesizing rGO/NiO nanocomposite with new structures. The incorporation of rGO with the NiO nanostructure favorable in minimizing the charge transport length and improving the charge conducting network Zhou *et al.* (2018). Herein, the facile synthesis of rGO/NiO nanocomposite was carried out with different ratios of rGO on NiO. So, in this study three dimensional interconnected network rGO/NiO nanocomposite was synthesized for supercapacitor electrode application. The as prepared rGO/NiO based modified electrode material showed better electrochemical performance with increased specific capacitance than pure NiO nanostructure.

Strategies based on selective fluorescence emission and quenching is an extraordinary tool for the optical sensing of heavy metal ions due to its higher sensitivity and simplicity. PL sensors using inorganic semiconductor quantum dots based on the PL turn-on and turn-off mechanisms were explored earlier by Chowdhury *et al.* (2021) Li *et al.* (2020). Low water solubility and higher toxicity are the main limitation in many fluorescent sensors for the sensing of metal ions in aqueous medium. Hence, it remains essential to develop a simple, effective and robust methods for toxic heavy metal ion sensing in water. Also, to date much work is not done on GQD compared to functionalized GQDs for sensing applications and so the sensing mechanism. In this work, GQD based PL sensor for heavy metal ion detection was done. The photoluminescence (PL) property of these intrinsic and label free GQD has been employed to devise an optical nano sensor for toxic heavy metal ions detection in aqueous medium.

## **1.2 Objective of present work**

The main objective of this work is to synthesize and analyze the properties of GO derivatives and GO composites such as rGO, rGO/NiO and GQD. Further their physicochemical properties will be studied to explore different applications such as energy

storage and sensing. The point wise objectives of the present thesis work are as follows.

1. To synthesize GO, rGO and to develop a simple, cost-effective, and template free method to synthesize PGN. And to study the electrical properties of GO and rGO.
2. To study the defect type (like 0D and 1D) and defect density evolved in the structurally reconstructed GO and rGO using Raman scattering.
3. To develop a rGO based metal oxide nanocomposite (rGO/NiO) as a modified electrode material with the improved electrochemical performance for energy storage application.
4. To devise a intrinsic, label free and hydrophilic graphene quantum dots as an optical nanosensor for the effective sensing of toxic heavy metal ions in water based on fluorescent quenching.

### **1.3 Scope of the work**

The surface functionalized GO and reduction controlled conductive nature of rGO structures are suitable for many essential applications like energy storage, sensors, flexible electronics and photovoltaics etc. The unique physiochemical characteristics of GO derivatives provides an alternative to the single layer graphene due to their simplicity in the fabrication methods with mass production towards diverse applications. Here, the obtained GO derivatives with the facile, low cost and scalable synthesis methodology has the following scope.

1. The chemically exfoliated graphene oxide by the modified Hummer's method will be used as a precursor materials for the synthesis of different GO derivatives. The GO structure with the  $sp^2/sp^3$  can be reduced further with the removal of oxygen functionalities through thermal annealing. The major challenge in developing a porous graphene network (PGN) structure with low reaction temperature, template free, chemical free and ecofriendly techniques can be achieved through the method of

thermal reduction of GO. A simple method to get the conductive rGO film and a method to analyse the electron transport behaviour of rGO film is achieved.

2. The experimental Raman parameters of GO and rGO samples annealed at different temperature with the intermixed defect density are analyzed with the theoretical defect diagram. This will be useful to extract information about the defect contribution and nature of disorder over the structural evolution. This method provides new insight into the defect type analysis generated on the GO based 2D material system with a better understanding of the atomic structure during structural transformation for further enhancement of material quality and integrating this material into the device.
3. Nanocomposites of rGO/NiO were synthesized for the supercapacitor electrode application. The incorporation of rGO with the NiO nanostructure favorable in minimizing the charge transport length and improving the charge conducting network. The change in specific capacitance with enhanced electrochemical performance of rGO/NiO modified electrode can be understood through increase of rGO concentration on NiO.
4. Hydrophilic graphene quantum dots (GQDs) based optical nanosensor for the sensing of heavy metal ions has been developed. The Stern-Volmer (S-V) plot analysis useful in understanding the mixed phenomenon of dynamic and static processes of PL quenching mechanism with the turn-off fluorescent effect of  $GQD/M^{2+}$ .

## 1.4 Organization of work

The thesis would comprise of seven chapters starting from introduction as the first chapter, which presents the brief introduction of different carbon nanostructures and their significance. It also includes the motivation, objective, existing research gaps and important contribution of the proposed research work. In chapter 2, the Basic concepts and experimental techniques about the graphite, graphene, graphene oxide derivatives

are discussed. The experimental methods and material characterization techniques for crystalline nature, structural information, chemical composition and morphology of GO derivatives has been discussed in this chapter. Chapter 3 presents the synthesis of GO by the chemical exfoliation of graphite precursor using modified Hummer's method. The formation of interconnected porous graphene network (PGN) like structure due to thermal exfoliation of GO sheets at different temperature is discussed. The gradual and controllable thermal reduction of GO at different reduction temperature. The role of functional groups on the evolution of electrical conductance during the rGO reduction was discussed. The temperature dependent defect evolution and defect identification of GO using the nondestructive Raman spectroscopy is studied in chapter 4. The contribution of different types of defects (0D and 1D) during the structural reconstruction of GO was analyzed with the comparing the experimental and a well known theoretical Raman model. The chapter 5 reports the synthesis of rGO incorporated NiO nanocomposite. The significance of rGO ratio on the rGO/NiO nanocomposites and their electrochemical performance has been studied. The hydrothermal synthesis of GQD by using GO as a precursor material is described in chapter 6. The photoluminescence (PL) property of label free GQDs towards the detection of heavy metal ions such as  $Hg^{2+}$ ,  $Cd^{2+}$  and  $Pb^{2+}$  in aqueous medium is discussed. Chapter 7 deals with brief summary of the research work and the future scope of this work.

### **1.4.1 Synthesis of GO, rGO and electrical Properties**

The GO was synthesized from graphite powder by the well known modified Hummers method through chemical oxidation and exfoliation. A facile cost-effective and template free method was developed to synthesize PGN based on thermal reduction of GO. During this reduction process, the reduction temperature and reduction time was optimized to get the PGN. The effect of annealing temperature on the morphology of rGO samples is explored using SEM. Structural and spectroscopic investigations shows that GO starts reducing at the temperature of 200 °C that is explicitly clear from the change in interlayer spacing, XRD and removal of functional groups, FTIR. The interconnected pore like structure was obtained from the reduction temperature of 300 °C. The experimental results reveal an exciting method of PGN synthesis that may have

a wide range of applications in sensing, energy storage and conversion. Gradual and controllable thermal reduction of GO film was carried out at low temperature regime. The conductivity of GO film depended on the degree of reduction. The influence of functional group over the electrical conductance of rGO during reduction is correlated with FTIR peak analysis. It is shown that the changes in conductivity is governed by two processes. The first process is mainly associated with water and OH groups desorption and second process is mainly associated with restored graphene  $sp^2$  network along with elimination of residual surface functionalities. Thermal reduction above 200 °C enhances the  $sp^2$  conjugations between the carbon atoms thereby improves the electrical conductance. This method enables one to control the electrical conductance of rGO by simply controlling the degree of reduction.

#### **1.4.2 First order Raman scattering to analyse defects in GO and rGO**

The complete analysis of structural transformation in a disordered structure like GO is very important to realize the structure-property relationship. Besides, the density, type and distribution of defects remarkably influence the characteristics of the material by the initiation of new properties and expanding their potential application in diverse fields. The experimental Raman parameters of GO and rGO samples annealed at different temperature with the intermixed (0D and 1D) defect density are analyzed with the theoretical defect diagram to extract information about the defect contribution and nature of disorder over the structural evolution. This method provides new insight into the defect type analysis generated on the GO based 2D material system with a better understanding of the atomic structure during structural transformation for further enhancement of material quality and integrating this material into the device. The structural transformation during reduction of GO was investigated using TEM, XRD, X-ray photoelectron spectroscopy and Raman scattering. The dependence of Raman scattering over the structural reconstruction of GO could be well understood by the analysis of integrated peak area ( $A_D/A_G$ ) and G band spectral line width  $\Gamma_G$ . This method is helpful to extract information about the defect contribution and nature of disorder over



the structural evolution. Also it provides new insight into the defect type analysis of GO based material system for the better understanding of structural transformation, material quality and integrating this material into the device.

### **1.4.3 rGO/NiO nanocomposite: synthesis and electrochemical properties**

The evitable demand on energy storage systems such as supercapacitor with higher power density and longer cycle stability than batteries increases due to the requirement of advanced technologies such as portable electronic devices, back up power sources, hybrid electric vehicles, flash cameras and so on. The type of nanostructured electrode material plays a significant role in the determination of supercapacitor performance. The supercapacitor electrode materials of higher surface area, better porosity revamps the electrochemical performance by improving the conductivity and charge storage. In that regard, nanocomposites of three dimensionally interconnected porous and conductive rGO/NiO based structures was synthesized and used as modified electrode material to enhance the specific surface area and conductivity. The assembly of three dimensional porous rGO network and nanoflakes like NiO nanostructure promotes the accessibility of electrolyte ions and improves the charge transport (both electrons and ions) inside the electrode. The enhanced electrochemical performance with higher specific capacitance is mainly attributed to the improved porous structure and increase surface area of the rGO/NiO composite. The rGO/NiO nanocomposite modified electrode showed a four fold increase in specific capacitance value when compared with the bare NiO structure. The specific capacitance ( $C_s$ ) values are 262.92, 350.28 and 417.52 F/g at a minimum scan rate of 10 mV/s for the corresponding rGO ratio of 5%, 10% , and 20% on NiO. The as prepared rGO/NiO composite nanostructure improves the electrochemical performance of the modified electrode with the increase of rGO addition on NiO.

#### 1.4.4 Synthesis of GQDs from GO and sensing application

Water contamination by toxic heavy metal ions severely impacts the health of human beings and environment. Sensors based on graphene based materials like GO, rGO, GQD and carbon nanotubes are being proposed for the detection of heavy metals. The oxygenated functional groups decorated GQD effectively enhances the aqueous solubility and considered as a more desirable and simple sensing material with high sensitivity. Hydrothermal method was employed to synthesize highly fluorescent and water soluble GQD from GO as a precursor material. Detection of toxic heavy metal ions is based on photoluminescence (PL) quenching mechanism of GQD. The fluorescent intensity of GQD@ $M^{2+}$  system quenches with the increase in the concentration of metal ions. This is possibly due to strong interaction between the metal ion and the GQD that enables effective energy transfer followed by the non-radiative recombination of charge carriers improves the quenching process. The change in PL intensity was analyzed by the Stern-Volmer equation to study the fluorescent quenching mechanism of the system. Nonlinear behavior of Stern-Volmer plot suggests that the reduction in the fluorescent intensity is due to the combination of dynamic and static processes. The fluorescence quenching results showed that, the as synthesized GQD are efficient fluorescent probe for the sensing of heavy metal ions viz.  $Hg^{2+}$ ,  $Cd^{2+}$  and  $Pb^{2+}$  with the limit of detection of 1.171  $\mu$ M, 2.455  $\mu$ M and 2.011  $\mu$ M respectively. Furthermore, this work indicates that, the biocompatible GQD are a viable and high potential material which could be extended as an attractive sensing unit for real time detection of heavy metals in water with good sensitivity and cost-effective.

### 1.5 Summary and Conclusions

In this research work, GO was synthesized by the modified Hummer's method. Thermal reduction of GO was used to improve the physicochemical characteristics of rGO through de-oxygenation and restoration of  $\pi$  conjugation. The thermal reduction provides interconnected porous graphene network (PGN) like structure at elevated reduction temperature. Reduction of GO films showed enhanced electrical conductivity with the increment of temperature. The structural reorientation with the contribution of point

and line defects of GO and rGO during oxidation and reduction was well understood by comparing the experimental and theoretical analysis of Raman spectral features. The thermally reduced GO with porous interconnected network was employed to synthesis rGO/NiO nanocomposite. The as synthesized rGO/NiO hybrid nano structure was developed as an modified electrode materials and their electrochemical performance was analysed. The hydrophilic GQDs was synthesized hydrothermally using GO as a precursor material. It has been developed as an optical nanosensor for the detection of toxic heavy metal ions in aqueous media. Here, the charge transfer between the GQD and metal ions followed by the non radiative recombination was employed as an effective sensing phenomenon of GQD based PL sensor.

# CHAPTER 2

## Basic concepts and experimental techniques

### 2.1 Graphene based nanostructures and classification

#### 2.1.1 Graphite

Graphite is the high crystalline, largely available allotropes of carbon. It composed of multiple layer of carbon atoms with the hexagonal honeycomb lattice. All the atoms in the graphitic lattice are  $sp^2$  hybridized, covalently bonded with the C-C bond length of  $1.42 \text{ \AA}$ . The graphite layers are stacked along the C axis crystallographic direction. Layer of 2D graphitic sheets will stack on each other and bonded with the Van der Waals interaction and forms a 3D graphite structure. The multistacked graphite layer in general aligned in two way namely ABAB and ABCABC. The nonequivalent surface layer arrangement brings structural site assymetry to the hexagonal graphite structure and facilitates the changes in the local density of states Atamny *et al.* (1999).

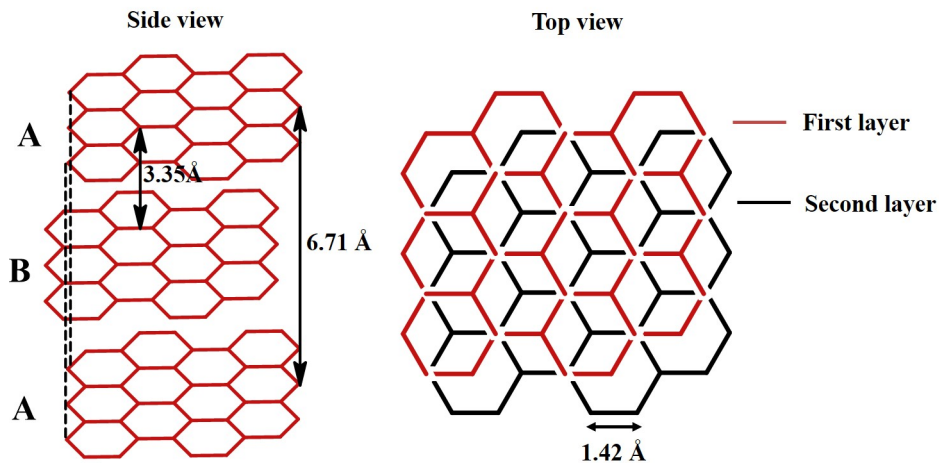


Fig. 2.1: Schematic representation of graphite crystalline structure

The delocalized electrons of the carbon atoms provides conductive nature to the graphite structure. The interplanar distance ( $d$ ) between the respective graphitic plane

is 3.35 Å. The spacing between the two identical layers is 6.71 Å. The respective space group is  $P6_3/mmc(=D_{6h}^4)$  for a graphite with the hexagonal lattice. The six notable phonon modes of graphite structures are  $2B_{2u} + 2E_{2g} + A_{2u} + E_{1u}$ . Among  $2E_{2g}$  vibration mode is Raman active, in which the vibration of adjacent planes are in phase or opposite with each other Tuinstra and Koenig (1970). By virtue of their reliable electrical conductivity ( $\approx 102 \text{ S cm}^{-1}$  at room temperature) and structural stability, graphite structure finds more application in many field as electrodes in energy storage devices, filler in polymer composites and also electromagnetic shielding material in many electronic devices Bhattacharjee *et al.* (2020).

### 2.1.2 Graphene

The graphene structure with a 2D honeycomb lattice comprises of isolated one atomic thick sheet of carbon atoms tightly bonded together with  $sp^2$  hybrid orbital with covalent bonds like in graphite Novoselov *et al.* (2004). Graphene is one of the lightest and thinnest 2D structure with the specific surface area of  $2630 \text{ m}^2 \text{ g}^{-1}$  and a single layer thickness of only 0.335 nm. Some of the unique characteristics of graphene are conjugated network, zero bandgap, as the energy band structure is symmetric around K point, massless Dirac fermion like behavior of the charge carriers and lower density of states Li *et al.* (2017b). The term graphene was proposed and recommended by the international union of pure and applied chemistry in the year of 1986. The name graphene evolves from the suffix "ene" meant for polycyclic aromatic hydrocarbons like naphthalene and prefix "graph" from graphite. Single layer  $sp^2$  hybridized orbitals with the flat and curved like graphene and fullerene holds six and five membered carbon rings possesses electron clouds on both sides of the layer. Each carbon atom in the six carbon ring of graphene lattice are joined together by three nearby carbon atom through a sigma ( $\sigma$ ) bond. The  $\pi$  bond are formed by the bond formation of remaining electrons with the nearby atoms. The  $\pi$  bond is perpendicular to the graphene lattice plane. The bond length of C-C bond is 0.42 nm. Their structural tolerance towards the external forces provides more stability to the graphene lattice Yu *et al.* (2020). The above structure provides a broad diversity in the characteristics of graphene materials. Carbon has 4 valence electrons at their outer orbit in which 3 electrons occupies  $2S$ ,  $2P_x$  and  $2P_y$

states and forms  $sp^2$  hybridization. The remaining fourth electrons forms the  $\pi$  bonds and free to move freely in graphene plane.

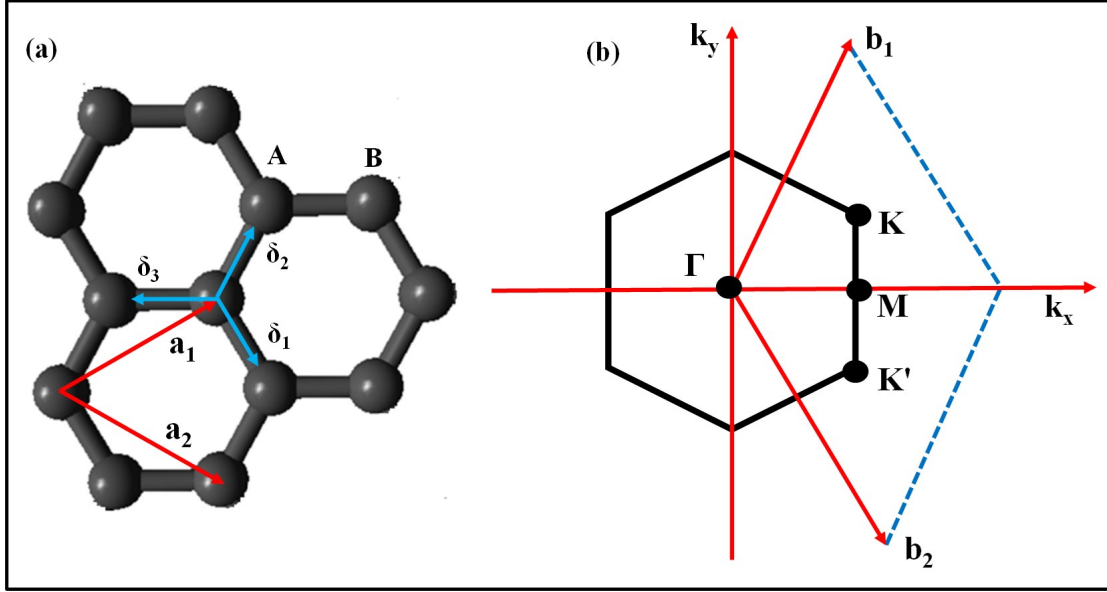


Fig. 2.2: (a) Schematic representation of unit cell in graphene lattice (b) The Brillouin zone of graphene unit cell

The lattice vectors values are given in eqn 2.1 2.2 Sang *et al.* (2019)

$$a_1 = \frac{a}{2}(3, \sqrt{3}) \quad (2.1)$$

$$a_2 = \frac{a}{2}(3, -\sqrt{3}) \quad (2.2)$$

The reciprocal lattice vectors are written in eqn Sang *et al.* (2019)

$$b_1 = \frac{2\pi}{3a}(1, \sqrt{3}) \quad (2.3)$$

$$b_2 = \frac{2\pi}{3a}(1, -\sqrt{3}) \quad (2.4)$$

The K point at the Brillouin zone edges of graphene unit cell is termed as the Dirac points. The position of K points at the momentum space and the value of nearest neighbour points are given in Sang *et al.* (2019)

$$K = \frac{2\pi}{3a}, \frac{2\pi}{3\sqrt{3}}, K' = \frac{2\pi}{3a}, -\frac{2\pi}{3\sqrt{3}} \quad (2.5)$$

$$\delta_1 = \frac{a}{2}(1, \sqrt{3}), \delta_2 = \frac{a}{2}(1, -\sqrt{3}), \delta_3 = -a(1, 0) \quad (2.6)$$

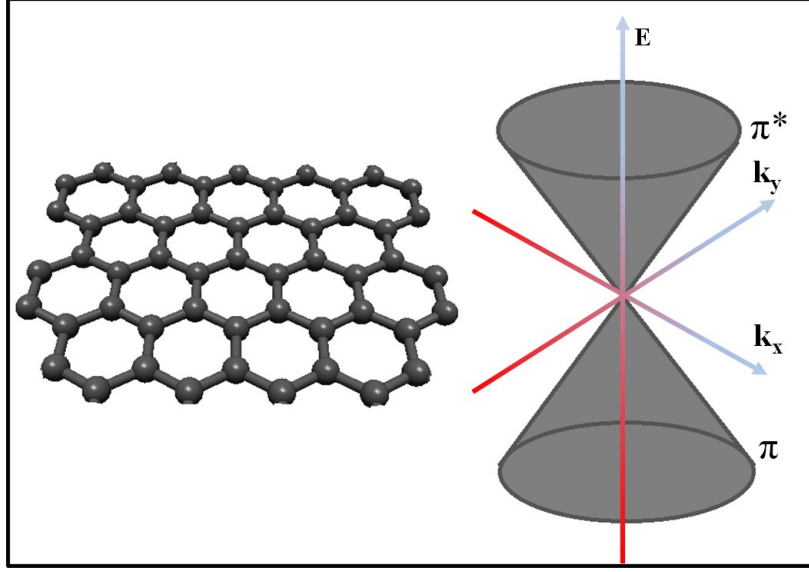


Fig. 2.3: Schematic representation of energy band structure of single layer graphene lattice with zero band gap at the Dirac point

In fig 2.3,  $k_x$  and  $k_y$  are known as momentum values along the x and y direction. The energy dispersion value of graphene single layer is given in eqn 2.7 Li *et al.* (2017b)

$$E_{\pm}(k) = \pm v_F |k|; \text{ where, } v_F = 3at/2 \quad (2.7)$$

In eqn 2.7, ' $k$ ' denoted as the relative momentum. Fermi velocity is defined as the  $v_F$  ( $10^6$  m/s). The lattice vector and hopping energy are denoted as ' $a$ ' and ' $t$ '. The plus and minus signifies the upper and lower energy levels ( $\pi$  and  $\pi^*$ ). From the energy dispersion diagram it is observed that, at the Dirac point ( $k$  or  $k'$ ), the graphene possesses a zero bandgap nature. The energy  $E(k)$  makes a linear relationship with the momentum  $k$  and  $v_F$  is independent of energy. But in a three dimensional material systems the E-K relationship will be  $E_k = k^2/2m$ . With its unusual structure and remarkable properties, graphene is considered as a base structure for the exploration of new graphene-based materials for the advancement of modern technologies. Some fascinating physical phenomena of graphene are room temperature quantum hall effect, ballistic transport of charge carriers with an ambipolar electric field effect and higher

elastic strength Novoselov *et al.* (2007); Lee *et al.* (2008) mainly arises due to the lower density of states, zero bandgap and dirac fermion like behaviour. These unique properties of graphene finds application in many technological fields such as nanoelectronics Akinwande *et al.* (2019), photodetector, energy storage Wei *et al.* (2019), sensor Kamat *et al.* (2019), photovoltaics Paul *et al.* (2020) and biomedical Tadyszak *et al.* (2018) and so on. Due to the higher conductivity, disadvantages like lower on-off ratio are also observed in single layer graphene FET devices Schwierz (2010). Despite having distinct material characteristics, the zero bandgap intrinsic nature of graphene structure limits the practical application of this material in many fields. The semi metallic property with the zero bandgap of graphene single layer is mainly contributed by the symmetric crystalline nature of graphene structure. Breaking the graphitic symmetry through doping, defect formation, surface functionalization are the possible way to tune the energy gap of the graphene structure. Also, defect engineered graphene structure with substitutional doping and oxygen functionalities initiates new improved properties such as increased biocompatibility and reduced toxicity.

### 2.1.3 Graphene oxide

The GO is an oxidized form of graphene layer decorated with several functional groups such as hydroxyl, epoxide, carbonyl, and carboxylic groups on the basal plane and the edges. The hydrophilicity of GO arises from oxygen containing groups. The structural model of GO (L-K model) with random distribution of oxygen groups was reported by Lerf and Klinowski *et al.* (L-K) Lerf *et al.* (1998). The surface functionalities like hydroxy (-OH) and epoxy (C-O-C) are usually arranged on the basal plane of single layer GO sheet. Whereas, the functional groups like carbonyl(C-O) and carboxyl (C=O) mostly distributed on the sheet edges. The schematic representation of GO structure based on the well known L-K model is shown in Fig 2.4. In addition to the oxygen functionalists, the GO structures comprises of oxidized  $sp^2$  region and defective regions due to over oxidation and layer exfoliation of the GO lattice as reported by Erickson *et al.* Erickson *et al.* (2010). The interaction of oxygen functionalities with the carbon atoms forms a  $sp^3$  hybridization and brings hydrophilic nature to the GO sheets. So, the  $sp^2$  (aromatic) and  $sp^3$  (aliphatic) hybridized nature of GO shows more hydrophilicity and



surface activity than the graphene single layer.

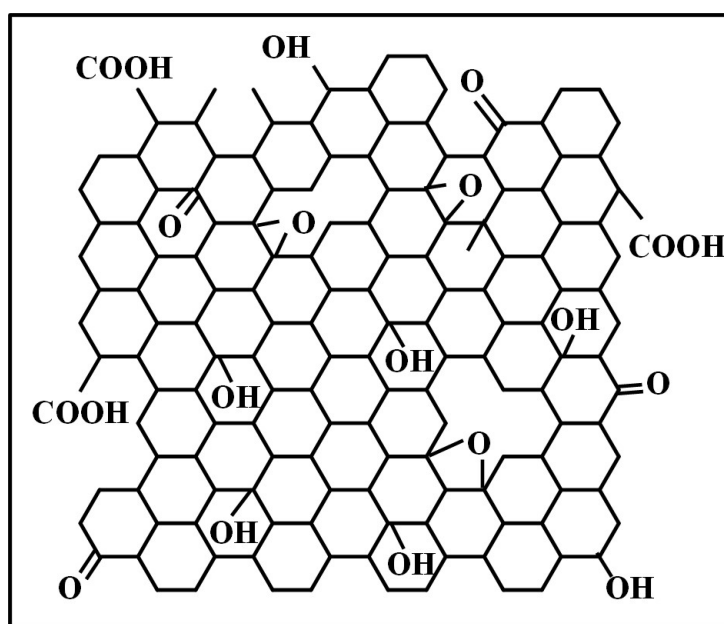


Fig. 2.4: Schematic representation of Lerf and Klinowski (L-K) model of GO structure

#### 2.1.4 Reduced graphene oxide

The few layer GO sheets with the oxygen functionalities of  $sp^2/sp^3$  hybridization exhibits the electrical insulator sort of behavior with the wider band gap value of  $>2.7$  eV. The material characteristics are contributed by the intercalated water molecules and oxygen groups on the surface of GO. The Fig 2.5 shows the schematic band structure diagram of GO and rGO layers. The line near the edges of the bandgap signifies the localized energy states of GO and rGO. The density of states value varies with respect to the density and type of defects exist on the GO lattice. Manipulating the density of surface functionalities on the GO structure through different reduction techniques like chemical, thermal, microwave, electrochemical and optical protocols severely alter the intrinsic properties of the GO. The structural characteristics such as conductivity, stability, solubility, surface activity, density of states, mobility of charge carriers of GO are modified during the reduction process. During the reduction process, the carbon to oxygen (C/O) ratio of the GO layer increased with the expulsion of oxygen functionalities and carbon lattice restoration. The defect engineered hexagonal graphitic lattice

with the reduced oxygen functionalities on the rGO sheet significantly tunes the bandgap of the rGO and thereby increases the conductivity. Meanwhile, the defects in the rGO lattice enhances the structural characteristics by providing increased surface area and active sites. So, the rGO can also be called as modified graphene because it features the characteristics of graphene with improved conductivity than the GO. So, the synthesis of rGO from GO is a simple way to fabricate defect induced graphene sheet of fewlayer with residues of surface functionalities in large quantity. The physicochemical properties of rGO largely depends on the method of fabrication as this governs the formation of graphene layers, degree of oxidation and partial restoration of carbon lattice.

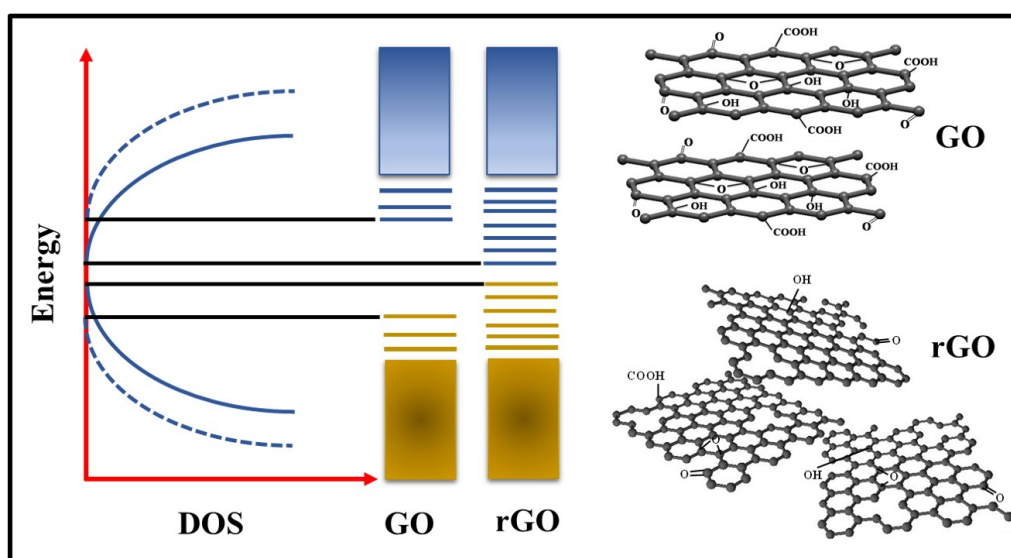


Fig. 2.5: Schematic representation of density of states (DOS) of GO and rGO structure

### 2.1.5 Graphene quantum dots

The GQDs, a quasi-zero-dimensional carbon nanostructure are the fragmentation of 2D graphene oxide sheets. They are constructed by the graphene lattice, interlayer defects, edges and decorated with the surface functional groups. The GQDs with the quasi 0D structure and lateral dimension of less than 100 nm exhibits quantum confinement effect and edge effects mainly contributed by the size and basal plane defects on the  $\pi$  conjugated domain which promotes the photoluminescent characteristics. The size dependent characteristics of the zero dimensional (0D) GQD comparable to the exciton bohr radius offers unique quantum confinement effects. The major property with the

higher edge to basal plane ratio provides the edge effect to the GQDs with enhanced physical and optical property.

## **2.2 Synthesis methods of graphene oxide and derivatives**

### **2.2.1 Chemical oxidation of GO**

The distinct surface chemistry with the cost-effective mass synthesis process of GO has increased the interest on materials based on GO derivatives. There are numerous numbers of physicochemical techniques that focus on synthesizing GO in order to use their remarkable characteristics for distinct applications. One of the most inexpensive ways to synthesize graphene oxide is the top-down approach through chemical oxidation by using graphite as a precursor material. The chemical synthesis of GO generally a two step process. First is the intercalation and oxidation with the heavy oxidant followed by the graphene layer exfoliation. Synthesis with distinct oxidants, reaction time, reaction temperature with different proportion were proposed by Brodie (1859), Staudenmaier (1898), Hummers Jr and Offeman (1958) et.al.

### **2.2.2 Brodie and Staudenmaier method of GO oxidation**

The well-known method of chemical oxidation of GO established in the middle of eighteenth century by Schafhaeutl (1840) Brodie (1859) and L. Staudenmaier (1898) Brodie (1859); Staudenmaier (1898); Scharfenberg *et al.* (2011). The GO synthesis reaction proposed by Brodie in the year of 1859 used the graphite powder with potassium chloride ( $KClO_3$ ) with 1:3 ratio in fuming nitric acid ( $HNO_3$ ). L. Staudenmaier method (improved Brodies method) of GO synthesis was improvised with the addition of Sulfuric acid ( $H_2SO_4$ ) for substituting two third quantity of  $HNO_3$  in order to increase the acidic nature of the reaction in addition to  $KClO_3$ . The achieved level of oxidation and carbon to oxygen molecule ratio (C/O) of the product was less by the above methods.

### 2.2.3 Modified Hummmer's method of GO synthesis

Hummers and Offeman at the year of 1959 proposed a chemical route for the oxidation of graphite with increased C/O ratio by using heavy oxidative reagents such as Potassium permanganate ( $KMnO_4$ ), Sulfuric acid ( $H_2SO_4$ ) and Sodium nitrate ( $NaNO_3$ ) Hummers Jr and Offeman (1958). Graphite powder is mixed with the  $NaNO_3$  and  $KMnO_4$  oxidizing agent at a 1:0.5:3 ratio with concentrated ( $H_2SO_4$ ) solution for the oxidation and exfoliation process. In acidic medium  $KMnO_4$  plays a role of strong oxidant and ( $H_2SO_4$ ) acts as a molecular scissor or chemical driller for graphite lattice plane to enable the infusion of oxidation agent Dreyer *et al.* (2009). Thus, the concentrated  $KMnO_4$  useful in the intercalation of graphite layer with the penetration of  $KMnO_4$  oxidizing agent and enhances the oxidation process. The protocol of chemical oxidation proposed by Hummers and Offerman later called as Hummers and modified Hummers method to synthesize GO is showed in Fig 2.6. In addition to the chemical oxidation subsequent ultrasonic exfoliation process helpful in the formation the GO layers during the process steps. Other exfoliation process like mechanical and thermal exfoliation are also for breaking the graphite oxide structure in order to delaminate the graphite oxide into two dimensional GO nanostructure Cai *et al.* (2012). Some reports on GO synthesis by the modifying the hummers method with the increasing amount of  $KMnO_4$  and varying the ratio of  $H_2SO_4$  and  $NaNO_3$  Chen *et al.* (2013). Further, phosphoric acid is also used as the replacement of  $NaNO_3$  in the improved Hummers approaches in order to avoid the emission of toxic gases like  $NO_2/N_2O_4$  during the reactions and also used to enhance the product yield Marcano *et al.* (2010). The obtained chemical composition of GO by the chemical oxidation methods comprises of layered graphite with increased interlayer spacing or interstices of above 7 Å due to the insertion of oxygen functionalities Asgar *et al.* (2018). The basal plane and interstices functional groups facilitates the chemical reactivity through improved the adsorption/desorption characteristics of the molecular species on GO.

In modified Hummer's method, during the initial stage of oxidation reaction, the concentrated  $H_2SO_4$  performs as an intercalation agent by open up the graphite layers and make this more opt for the oxidation process without much change in the graphite structure. Then the oxidation is spread towards the basal plane of the GO sheet.

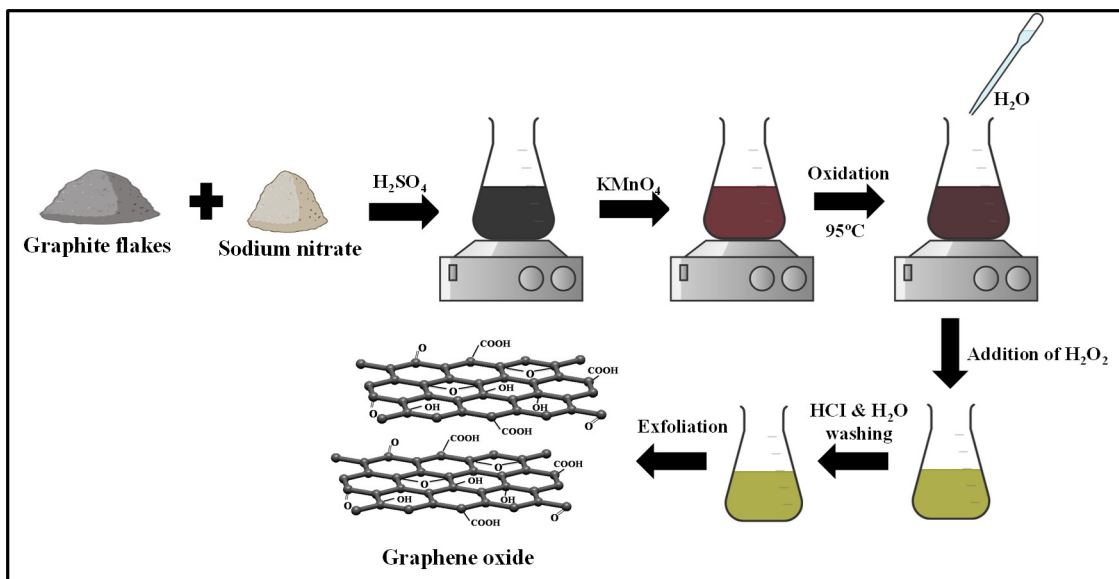


Fig. 2.6: Schematic representation of GO synthesis using modified Hummer's method

The hybridization of the C=C atom in native graphitic lattice changes from  $sp^2$  to  $sp^3$  as the functional groups have interacted with carbon atoms. During the above process, the condensation of phenolic groups (like hydroxy) on the carbon lattice will form the epoxy groups (C-O-C) or quinone groups. The residual functional groups from the edge of the carbon lattice are oxidized and forms ketone groups. These will be formed as carbonyl and carboxylic groups ((O-C=O) and COOH) at the edges along with the degassing of  $CO$  and  $CO_2$  and distortion of carbon lattice. So, the hydroxyl and epoxy groups distributed randomly on the basal plane while the carboxylic and carbonyl will form on the edges of the GO lattice Shao *et al.* (2012); Guo *et al.* (2019); Aliyev *et al.* (2019). The oxo-functionalities in GO are polar molecules offers effective hydrogen bonding with the solvent and improves the dispersion stability thus increases the hydrophilicity Gupta *et al.* (2017). Thus, the GO structure with hydrophilic functionalities helpful in improves the physicochemical characteristics and elevating its significant application such as catalytic, sensing and storage. Though there are lots of significant modification are carried out in the existing hummers method of GO synthesis yet this method is considered as a basis of liquid based chemical exfoliation of GO.

## 2.2.4 Reduction of graphene oxide

The rGO can also be called as chemically or thermally modified graphene because it features the characteristics of graphene Sharma *et al.* (2020); Eda *et al.* (2009). The physicochemical properties of rGO largely depends on the method of fabrication as this governs the formation of graphene layers, degree of oxidation and partial restoration of carbon lattice Voiry *et al.* (2016). Fabrication of rGO, having similar characteristics like single layer graphene excepts the defects from GO is the most exciting segment in the era of graphene. Reduction with the optimum method favorable in minimizing the oxygen functionalities and advantageous in the defect engineering through the restoration of graphitic lattice of rGO. GO reduction is generally happened through chemical, thermal and hydrothermal, and microwave assisted techniques Quezada-Renteria *et al.* (2019); Savchak *et al.* (2018); Huang *et al.* (2018); Voiry *et al.* (2016). Alternatively, the direct reduction of GO thin films over the substrate like silicon wafer, glass and polymer (polyether sulfone, polyimide, polycarbonate, polyethylene naphthalate, and polyethylene terephthalate) with the subsequent reduction either by chemically, thermally, hydrothermally, laser and microwave assisted reduction are also a versatile methodology in GO reduction techniques Zeng *et al.* (2019); Okhay *et al.* (2016); Voiry *et al.* (2016); Feicht and Eigler (2018). These type of rGO film reduction will be more desirable in the field of graphene-based electronics and device applications. Among all the methods, thermal annealing is evolved as a simple technique by caring advantages like ecofriendly reduction process and controlled degree of oxidation with the simultaneous structural reconstruction.

## 2.2.5 Thermal reduction of GO

The rGO structure obtained by the thermal annealing of GO is termed as thermally reduced GO. The exfoliation of graphene oxide in order to obtain the graphene like structure with the reconstructed carbon lattice usually happened at inert condition, vacuum and a very high annealing temperature of  $>2000$  °C as reported earlier Zhuo *et al.* (2018); Schniepp *et al.* (2006); Silipigni *et al.* (2019); McAllister *et al.* (2007); Zhang *et al.* (2011). The low temperature thermal redcuton of GO at ambient condition are

also reported by Yang *et al.* (2020); Shen *et al.* (2013a); Tegou *et al.* (2016); Sengupta *et al.* (2018). During rGO reduction, the elimination of surface functionalities from the GO is considered as main key factor of rGO synthesis. As reported by Wei *et al.*, the low temperature thermal reduction of GO below 500 °C has two main weight loss stages Wei *et al.* (2010b). The first weight loss of GO at 100 °C mainly attributed by the water molecule evaporation. The second main weight loss from 200 °C is due to the removal of surface functionalities. During the second stage of thermal reduction process, the de-gassing of surface oxygen groups ejected from the graphitic lattice with the expulsion of innate carbon atoms and forms deformed graphene lattice. So, the thermal reduction used to happen at optimum temperature. Also it could be attained by maintaining the stress evolved inside the GO lattice due to the expulsion of oxygen functionalities. The effective thermal exfoliation is possible when the rate of decomposition exceeds the rate of diffusion of evolved gas molecules from the GO lattice. The thermal pressure exerted by the decomposition of oxygenative functional groups is 40 MPa at 300 °C and 130 MPa at 1000 °C. The pressure value of 2.5 MPa is an adequate value for the GO layer exfoliation with respect to Hamaker constant as reported by McAllister *et al.* McAllister *et al.* (2007).

## 2.2.6 Chemical reduction of GO

Reduction of GO through chemically by using different reducing agents is considered as one of the easiest and cost effective method to obtain rGO at room temperature. Chemical reduction of GO prone to yield rGO with higher C/O ratio as reported earlier Sharma *et al.* (2017). Among distinct chemical reductants (like sodium borohydrate, citric acid, dimethylhydrazine and hydrohalic acids) the hydrazine hydrate is the largely used reducing agent by researchers due to the rGO yield with higher C/O ratio Guex *et al.* (2017); Sharma *et al.* (2020). During addition of hydrazine hydrate  $N_2H_4$  on GO, the reducing agent produces Hydrozoic ions  $N_2H_3^-$  and  $H^+$  ions. Predominant reaction of  $N_2H_4$  happens with the epoxy (C-O-C) group of GO lattice Gao *et al.* (2010). The  $H^+$  ion reacts with the oxygen functionalities and they are ejected out from the GO surface in the form of  $H_2O$ . In such a way, the GO is reduced during the process steps of chemical reduction. Owing to the many advantages, the chemical reagents used in

the chemical reduction processes are highly toxic to the environment. As an alternative green reduction of GO using various plants extracts are proposed by researcher in order to minimize the hazardous byproducts. GO reduction using the leave extract of Hibiscus Sabdarriffa, Azadirachta indica, Lycium barbarum are repoted earlier with the higher C/O ratio than chemical the reduction Kurian (2021); Ismail (2019). The phytochemicals in the plants extracts like flavanones and terpenoids are behave as a surfactants and effective reducing agents simultaneously.

### **2.2.7 Synthesis of graphene quantum dots**

The size and surface charge severely modifies the bandgap of the GQD and its becomes responsible for development of different physicochemical characteristics. Size controlled synthesis of GQD is still a challenging task for researchers since it reflects on the fluorescent behaviour of the GQD. However, the commonly used top-down approaches for GQD synthesis are, electrochemical treatment of GO, hydrothermal treatment of GO, e-beam lithography and laser ablation. Bottom-up approaches like pyrolysis and carbonization process using the organic carbon precursors such as citric acid, trisodium citrate, oxalic acid, glucose, poly ethylene glycol (PEG) are also involved on the self-assembled synthesis of GQDs Naksen *et al.* (2022); Yang *et al.* (2019); Ganganboina *et al.* (2018); Kalkal *et al.* (2020). Among all other methods hydrolysis and pyrolysis are explored as a simple and economical way of bottom-up approaches for the synthesis of GQD. The quantum dots of inorganic elements such as CdS, CdSe, CdTe, ZbS, PbS are highly preferred due to their explicit properties such as improved sensitivity, photo stability and many more Duan *et al.* (2011); Chowdhury *et al.* (2021); Mahmoud (2012). The major disadvantage of this quantum dots are low solubility and higher toxicity which restricts this material utility towards environmental and biological applications. In comparison to the conventional inorganic quantum dots, GQDs shows unusual material characteristics such as reduced toxicity, higher dispersibility or solubility, improved surface grafting and enhanced photoluminescence building them as a potential material for various applications such as biosensing, molecular imaging and optoelectronic devices Wang *et al.* (2014). So, the GQDs are emerges as an eco friendly substitution to the existing toxic semiconductor quantum dots.



## 2.3 Defects in GO derivatives

In general, GO and derivative have an exceptional structural property such as lattice disorientation and defects like dopant atom, lattice strain, phase, pores, wrinkles and corrugation in their lattice structure Song *et al.* (2019); Eigler *et al.* (2012); Khaliha *et al.* (2021); Nandanapalli *et al.* (2019). Thus, the defects are important in determining the properties of two-dimensional (2D) materials. Material structure with the defect dispersal significantly alters the inherited properties like band structure, charge carrier density, charge mobility and thermal conductivity, light absorption and mechanical stability Zeng *et al.* (2018); Thangamuthu *et al.* (2019); Ding *et al.* (2018); Abid *et al.* (2018). Defects are generated mainly during the synthesis and processing steps. Exploring and quantifying the defects is more beneficial for taking this structural modification towards specific applications. Some of the explicit characterization techniques reported by the researchers for defect analysis are Raman scattering, AFM, STM, TEM and optical microscopy.

Defects in the graphene and graphene derivative structures are generally categorized into intrinsic or in-plane lattice defects and extrinsic or on-plane lattice defects Ahmad *et al.* (2021). Structural deviation from the hexagonal graphitic lattice due to external stimuli are often termed as intrinsic type of defects. The introduction of dopants or oxygen functionalities during oxygenation and functionalization with the transformation in hybridization from  $sp^2$  to  $sp^3$  stimulates extrinsic type of defects on the graphitic lattice Feicht and Eigler (2018). Point, vacancy, dislocations and grain boundaries are the distinct kind of zero and one dimensional (0D and 1D) defects typically generated on the graphitic lattice Schweizer *et al.* (2018); Meyer *et al.* (2008); Qin *et al.* (2020). The schematic representatoin of distinct types of defects evolved on the GO lattice is shown in Fig 2.7.

### 2.3.1 Vacancy defects

By purposely removing the carbon atom from the graphene lattice during the fabrication process is often leave vacancy on the 2D lattice Qin *et al.* (2020). These sort of defect are generated during the processing stages are called as vacancy type defects. Single

and double vacancy are possible by the ejection of single and two carbon atoms from the carbon lattice. The total energy of the 2D lattice got reduced which makes a nearby carbon bonds to move towards the vacancy with the formation of carbon dangling bonds Banhart *et al.* (2011); Chisholm *et al.* (2012). The above process will increase the local density of states at the fermi energy level and facilitates the protruding graphene lattice Banhart *et al.* (2011). Lattice formation with single vacancy with 5/9 carbon ring formation and double vacancy with double octagon and single pentagon (8-5-8) and three pentagons and three heptagonal (555-777) carbon ring formation are the types of vacancy defects in 2D graphene lattice Boas *et al.* (2019). Defective graphene with the vacancies has more chemical stability, absorb more energy and promotes the molecular interaction than the pristine graphene layers. Introduction of vacancies on the graphene lattice improves the mechanical stability with the improved flexibility behavior at the contact edges and the vacancy controlled contact friction enhances the conductivity Gajurel *et al.* (2017).

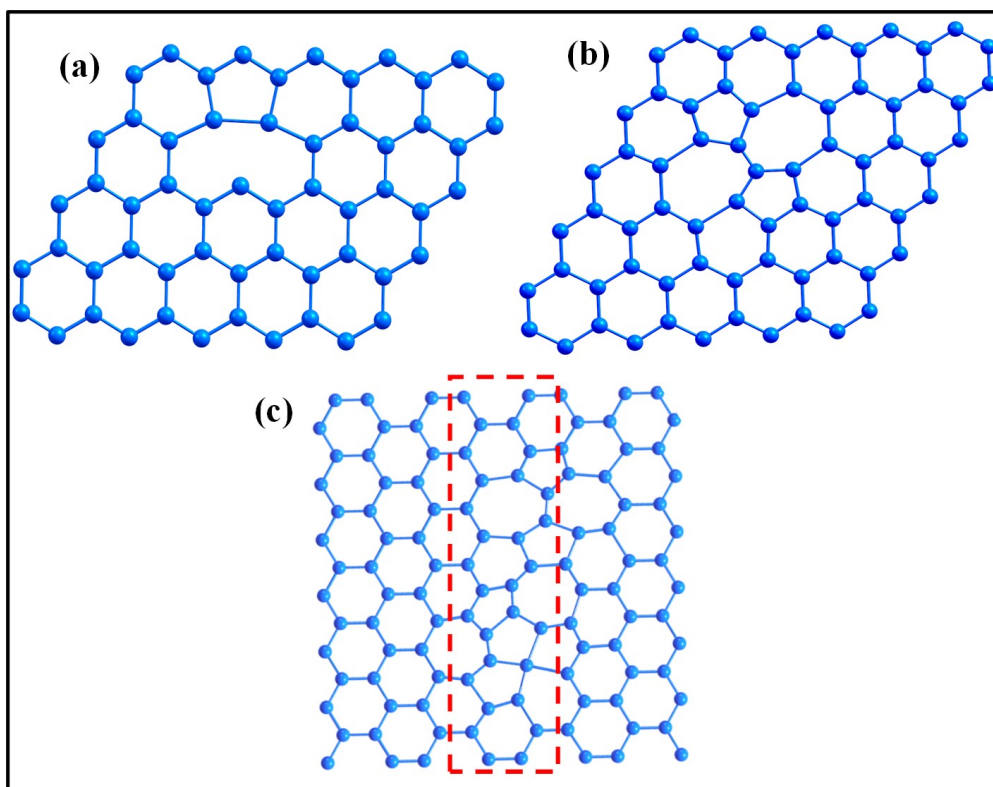


Fig. 2.7: Schematic representation of defective GO lattice (a) Vancancy (b) Stone-Waals's and (c) Grain boundary defect

### 2.3.2 Stone-Waals's defects

Graphene lattice developed with non-hexagonal rings are often called as StoneWaals's defects. The hexagonal carbon rings are included or detached with any extra carbon atoms either the carbon bond length is stretched or rotated to a specific angle ( $\approx 90^\circ$ ) due to external stimuli like irradiation. This process does not involve in any removal of carbon atom from the graphene layer. The carbon atoms in these defected region coordinated with the nearby atom without creating any dangling bonds makes this defect more nonreactive. So, it have the larger formation energy of 5 eV. The defects of the above type are often termed as topological defects Ahmad *et al.* (2021). They are unusual type of defect in a pristine graphene layers. Electron beam (E-beam) is the most common method to induce these types of defects in the graphene-based 2D nanostructures.

### 2.3.3 Grain boundaries and line defects

Graphene derivatives like GO and rGO during their large-scale synthesis may evolve as polycrystalline nanostructures which always comprises random atomic arrangement and orientation Xu *et al.* (2021). Grain boundaries formed during the above growth process are often called as grain boundary defects and line defects. Also, grain boundaries formed during the structural modification stimulated by the periodic array of defects mostly commonly initiated by the Stone-Wales types of defects. But the presence of grain boundary defects can significantly reduce the mechanical strength of a graphene and graphene oxide derivates. In a polycrystalline graphene with the grain boundaries the mechanical strength of GO sheet varies from five carbon ring to six carbon ring due to different orientation C-C bonds inside the structure. So, the instability in term of stretching, crack formation and fracture will occur more easily near the grain boundaries under tension due to higher potential energy. Due to uneven stress distribution near the grain boundaries where the Stone-Wales defect are more the C-C bonds are twisted as a effect of in plane tension and out of plane weak forces and then leads to rupture. As a sequential event, the tensile fracture propagates along the grain boundaries of polycrystalline structures and leads to material failure. So grain boundaries types of defects

severely plays an significant role in mechanical stability of polycrystalline graphene derivatives.

The defective graphene structure and nanocomposites of graphene are widely useful in various application like supercapacitors, biomedical devices, transparent electrode, environment and chemical sensors. Holey and porous graphene nanostructures facilitates the ion transport behaviour with wider conductive network that considerably enhances electrochemical energy storage reported by Liu *et al.* (2020b). Defect engineering of 2D graphene based modified electrocatalyst sufficiently enhances the amount of active site and improves the accessibility of electrolyte ions reported by Zhang and Lv (2018). The presence of defects on graphene based biodevices with increased adsorption sites are highly required to dock the biomolecular structures like DNA , protein and drug molecules on graphene reported by Kumar *et al.* (2020). The gas sensor device based on defective graphene of point like defects based hybrid structure for high sensitive detection of nitrogen oxide gas is reported by Ma *et al.* (2019b). The increment in the point defect concentration of the defective graphene through the silicon  $Si^+$  ion bombardment improves the sensor response intensity. With the increased number of adsorption sites and strong molecular interaction between the substrate and analyte molecules offered by the defective graphene significantly enhances the sensor performance with high response than the pristine graphene as reported by Ma *et al.* (2019b).

## **2.4 Experimental techniques**

### **2.4.1 X-ray diffraction**

The XRD is used to analyse the crystal structure, crystallite size and phase composition of a crystalline material. When the X-rays fall on a sample it leads to the formation of constructive interference if it satisfies Bragg's law ( $n\lambda = 2d \sin \theta$ ). In the XRD instrument the X-ray is obtained from a cathode tube. Generally copper is the target metal for the production of X-ray. X-ray is obtained from Copper K1. The sample is kept in the sample holder. Inside the XRD instrument detector is mounted at different position. The XRD instrument is connected with a computer to collect the data. The diffraction data is collected and processed. When the X-ray falls on the sample the electrons in

the sample vibrates in the same frequency that of the X-ray and gets accelerated. The electrons after acceleration emit radiation with frequency equal to the incident X-rays. Since the wavelength of the X-rays are equal to the atomic dimensions, they produce constructive and destructive interference. If the material is single crystalline then the XRD analysis will give a sharp peak. If the material is polycrystalline in nature and the grain size is small then the peak will be broad. This is because the diffraction takes place at an angle close to Bragg's angle. It's not the same as that of Bragg's angle. The crystallite size is calculated by the formula called Scherrer formula as  $D = 0.9 (\lambda/\beta \cos\theta)$ . Where,  $\lambda$  = wavelength of X-rays,  $\theta$  = Bragg's angle of the peak in degree. In this work, X-ray Diffraction (XRD) was obtained by PANalytical XPERT powder diffractometer with a high intensity CuK radiation ( $= 1.540 \text{ \AA}$ ) in the range from  $10^\circ$  to  $90^\circ$  at  $2\theta$  angle.

#### **2.4.2 Fourier transform infrared spectroscopy**

The FTIR spectroscopy is used to confirm the different chemical groups present in the sample. It can be used for both organic and inorganic samples. FTIR can be used to analyse solid, liquid and gaseous samples. Every functional group or chemical bond absorbs a particular wavelength of light. FTIR can be coupled with NMR, mass spectrum and other techniques to find out the unknown sample. The bonds in a molecule will vibrate at different frequency. This depends on the type of sample and the type of functional group present. The frequency of vibration can be related to ground state or excited state. The frequency of vibration is increased by exciting the chemical bonds with high energy. The infrared light from the source travels through the Michelson interferometer. The monochromatic source contains waves of similar frequency. If all the waves are in phase with each other then the light intensity will be high. When the phase difference increases then the light intensity decreases. A mirror is used to vary the phase difference. The interferometer is made up of a beam splitter, moving mirror and a fixed mirror. The beam splitter splits the light beam into two beams. Reciprocating movements are seen in moving mirror. The fixed mirror changes its path difference. Then the beams are combined to give an interference signal. This is decoded with Fourier transformation based mathematical model. The FTIR spectrum is generated by separating every

wavenumber. Here, the identification of functional groups was investigated by Fourier Transform Infrared (FTIR) Spectroscopy using PERKIN ELMAR; SPECTRUM RXI.

### **2.4.3 X-ray photoelectron spectroscopy**

The XPS is used to quantitatively analyse the chemical composition of distinct type of sample. It is a surface analysis method. In XPS, low energy X-ray is used to bombard the sample. This leads to photoelectric effect. The photoelectrons are recorded by electron spectrometer. Under high vacuum these photoelectrons reach the analyser. In XPS the sample is analysed for few nanometer (nm). When the sample is irradiated with X-rays of low energy, it can able to penetrate only up to few microns. Due to the interaction between the photons and the surface atoms the photoelectrons are emitted. The emitted photoelectrons are specific to the elements present in the surface of the sample. These electrons will have kinetic energy (K.E) given by  $K.E. = h\nu - B.E. - \phi_s$ ,  $h\nu$  = Photon energy, B.E = atomic orbital binding energy,  $\phi_s$  = work function of spectrometer. The incident X-rays are absorbed by the sample followed by the ejection of surface electrons. Detector will measure the energy of this ejected electron. The XPS contains an ultra-high vacuum system, X-ray source, detector and ion gun. The X-ray sources are Mg K and Al K radiation. The electron present in the sample surface will absorb the X-ray. A part of the photons energy will be converted to kinetic energy. When the electrons are ejected from the surface, a part of its energy is used to counter the coulombic attraction. This reduces its energy. The XPS spectrum is created by analyzing the kinetic energy and the number of electrons ejected from the surface of the sample. The obtained XPS results were taken by physical electronics PHI5000 XPS model and sample was excited by Al Ka source

### **2.4.4 Scanning electron microscope**

The SEM is a kind of microscope that scans a material surface with the aid of high energy e-beam in a raster scan mode. The electrons are ejected from a source called electron gun. The electron beams are focused by the aid of magnetic lenses to hit the sample at a particular precise point. There are two types of electron guns; thermionic

gun and field emission gun. In thermionic gun thermal energy is applied to a filament mostly made of tungsten. This will eject the electrons towards the sample. In field emission gun a strong electric field is used to eject the electrons. The magnetic lenses is an important component of SEM. These magnets are capable of controlling, bending and focussing the electron beam on the sample. During scanning, movement of the electrons are controlled by the magnetic coils. Fluctuating voltage is applied to these coils to create the magnetic field. The electron beam is moved on the sample by using these coils.

The sample is placed in the sample chamber to avoid vibration. When the electron beam interacts with the sample, it ejects secondary electrons from the surface of the sample. Detector is an important component of SEM. It detects the interaction between electrons and the sample surface. The secondary electrons ejected from the sample are detected by the detector. These electrons are gives the image of the sample. The back scattered electrons and the X-rays, detected by the detectors, are used to find out the composition of the sample. To avoid the interference between the electron beam and the air particles, vacuum is maintained in the sample chamber.

The brightness of the image depends upon the number of electrons reaching the secondary electron detector. Backscattered electrons from the sample surface and X-rays from below the sample surface are detected by separate detectors. The quantity of secondary electrons that enter the detector is heavily influenced by the nature of the specimen. Sample with elevated surfaces receives more electrons. So more electrons enters the detector. Whereas depressed surfaces receive fewer electrons and therefore less number of electrons enter the detector. As a result, higher objects appear brighter on the screen, while depressed ones appears dark. In thesis work, the scanning Electron Microscope (SEM) images of GO and rGO samples were obtained using FEI31 Quanta-FEG 200 high resolution SEM instrument with the accelerating voltage range of 200V-30 kV.

#### **2.4.5 Transmission electron microscope**

In TEM, the electron beam transmits through a very thin object. The interaction of electrons with the sample gives the image. This image is formed on the fluorescent

screen and then it is magnified. Electrons from the source are passed through the sample and the focusing lenses. The lens is an electric coil which generates electromagnetic field. The electrons are focused by the condenser initially then they are focused on the sample. The sample deflects the electrons partially. The electron density and the lattice parameter of the sample decides the degree of deflection. TEM will give high resolution up to  $\text{\AA}$ . When the wavelength of the irradiation reduces the resolution increases. The wavelength of electron is 100,000 X smaller than the visible light. So the resolution of TEM is 100,000X higher than light microscope. The electrons are produced by a heated tungsten filament which is called as electron gun. This is the cathode. The electrons move from the cathode towards the anode with high energy. The condenser lenses focuses the electrons on the sample. Collision between the electrons and air may deflect them. So, vacuum is maintained to obtain a clear image. The electrons are scattered by the sample. If the sample is very dense then more electrons will be scattered and the image will be darker. If the sample is not dense then very less electrons will be scattered and the image will be brighter. The image system consists of an objective lens. It also has intermediate and projector lenses. The objective lens gives a medium image. It is further magnified by projector lens. The sample image is recorded by a fluorescent screen. This fluorescent screen is located at the bottom. To take TEM images, the powder samples are dispersed in ethanol for 15 min. They are ultrasonicated. From this solution few drops are placed on the copper grid. It is 32 then dried and taken for TEM imaging. In this work, HRTEM analysis obtained using (JEOL JEM 2100 operated at an acceleration voltage of 200 kV).

#### **2.4.6 Raman Scattering**

The fundamental phenomenon behind the Raman scattering process is the inelastic scattering of light. It is the technique widely useful for the better understanding and identification of molecular structure either in a crystalline and nanocrystalline phase. Raman spectrum arises from the polarization of electric dipole happened due to light scattering and other factors like dopants, defects, vibrational models of molecules and phonon in a material system. It is a versatile technique for the characterization of 2D material systems like graphene, metal dichalcogenides and many more. Number of layers,



lattice strain, thermal conductivity, defect density are some of most common material characteristics can be studied using Raman microscopic analysis. The laser energy is more important parameter in Raman spectroscopy since it influences the scattered light wavelength.

The experimental setup of Raman spectroscopy consist of a sample stage, laser unit, monochromatic, charged coupled device (CCD) and a monitor. The light from the laser source interact with the sample surface and generate different types of scattered photos (elastically and inelastically). Filters are used to diminish the intensity of other signals like fluorescent signal and elastically scattered photons during the process. The inelastically scattered photons are further dispersed with the aid of monochromator and transmitted into the CCD array. The weak input signal are multiplied and processed into electronic signals inside the CCD. Finally the computer monitor used to store and display the output signal. The spectral resolution can be determined by type of diffraction grating, focal length of spectrometer, type of detector are some of the important factor,

Raman peaks in Graphite and Graphene: The Raman scattering of graphite based structures was reported very earlier by Tuinstra et.al Tuinstra and Koenig (1970). Later the names for the Raman peaks was proposed by Vidona et.al Vidano and Fischbach (1978). The Raman G band at  $1580\text{ cm}^{-1}$  signifies the  $E_{2g}$  phonon mode vibration of carbon atoms (in plane stretching vibration of C-C bond). The another Raman D band at  $1350\text{ cm}^{-1}$  arises from the  $A_{1g}$  breathing mode of hexagonal carbon lattice at the K point. It is also evolved due to the defects on the carbon lattice structure with the relaxation of Raman selection rule ( $q=0$ ). The above Raman G and D modes can also be recorded on a polycrystalline defective materials. Because, the Raman band of high frequency G peak arises even from the bond stretching of  $sp^2$  hybridized carbon atoms either in a form of polycrystalline chain or hexagonal rings. Also, the D mode becomes absent with nonexistence of hexagonal carbon rings. The existance D peak is due to intervally one phonon double resonance process. D ' band observed as a shoulder peak near G band results from the intravalley one-phonon DR scattering process between K and K'points Carozo *et al.* (2011); Ferrari and Robertson (2001). These detected D' band with weak intensity and minimal dispersion arises from the crystal defects acti-

vated by the phonon scattering with smaller wave vector  $q$  Ferrari (2007). Other peak of Raman spectrum at  $\approx 2700\text{cm}^{-1}$  (pristine graphite and graphene) and is termed as 2D arises due to the intervalley two phonon double resonance process. So, the Raman peaks are known as the molecular finger prints of carbon based materials. In this work, the structural analysis of GO and rGO was obtained by recording Raman spectra using LabRAM HR Evolution (Horiba-JYmake) micro-Raman spectrometer with the excitation wavelength of 633 nm at room temperature.

A theoretical Raman model supported by experimental data helpful in describing the dependence of the Raman scattering signal on the evolution of structural parameters along the structural transformation trajectory of graphene systems. The lattice dynamics and the procedure to measure the crystallite size ( $L_a$ ) and defect density ( $1/L_D^2$ ) of graphitic structures using Raman spectroscopy was handled many times before fifty years. Many reports have explained the detailed analysis of structure and defect mechanism on graphitic structures through a phenomenological theory useful in exploring the density, type and functionality of defects Tuinstra and Koenig (1970); Ferrari (2007); Cançado *et al.* (2007); Cançado *et al.* (2017); Lucchese *et al.* (2010); Ribeiro-Soares *et al.* (2015). Up to now researchers apply following proposed relation using intensity ratio ( $I_D/I_G$ ) and integral area ratio ( $A_D/A_G$ ) to understand the different types of defects present in GO/ rGO Cançado *et al.* (2017); Lucchese *et al.* (2010); Cançado *et al.* (2007) .

$$\frac{A_D}{A_G} = \frac{560}{(E_L)^4} X \frac{1}{L_a} \quad (2.8)$$

$$\frac{A_D}{A_G} = \frac{4300}{(E_L)^4} X \frac{1}{(L_D)^2} \quad (2.9)$$

But in Raman spectra of GO both kind of defects will be present at the same time since it is inherent. Thus, by applying above relations, it will give an over/ under estimation of final conclusions. In this present work, the contribution of both type of defects are taken at same time in the first order Raman spectra and analysed with our experimental results. The Raman analysis on the structural evolution of GO annealed at different temperature with the theoretical defect diagram to extract information about the defect contribution and nature of disorder over the structural evolution is discussed briefly in chapter 4.

## 2.4.7 Cyclic voltammetry analysis

Electrochemistry is a vital tool to identify the reaction involving electron transfer between the electrode and electrolyte. Very useful modern electrochemical technique is a cyclic voltammetry, this technique commonly employed for investigating the reduction and oxidation processes of molecular species. The cyclic voltammetry setup consists of electrochemical cell, electrolyte, counter electrode and reference electrode. Electrochemical cell is a vessel used in cyclic voltammetry setup, to keep all the electrode and electrolyte solution. In the electrolyte solution electron transfer will be occurred and the electro neutrality can be maintained by the ion migration through this electrolyte solution. Three electrode setup is used in cyclic voltammetry, glassy carbon electrode, platinum electrode, and Ag/AgCl electrode in common cyclic voltammetry experiment which represent a working electrode, counter electrode, and reference electrode, respectively. Working electrode carry out the electrochemical process of our interest and which contains the redox inert materials. The potential of the working electrode, as a function of reference electrode, is controlled by potentiostat. The equilibrium potential of the reference electrode is stable. It serves as a reference point to the other electrode in an electrochemical cell. The current flowing through the working and counter electrode can be accurately estimated by measuring the applied potential relative to a stable reference electrode. Counter electrode which completes the electrical circuit, when potential applied on the working electrode reduction or oxidation occur and current begins to flow, current is recorded as an electron flow from working electrode to counter electrode. Duck shaped plot which was generated from cyclic voltammetry is called cyclic voltammogram. In the cyclic voltammetry plot initially the potential is not sufficient to oxidise the analyte if the potential reaches specific value, oxidation occur and current is exponentially increasing. The current reaches the point of maximum which is anodic peak current and the voltage is anodic peak voltage which represent oxidation of material. In the reduction process the voltage is reversed to opposite scan direction and cathodic peak current and cathodic peak voltage is measured due to deduction process. If the anodic and cathodic peak current are equal and opposite in direction means the process is reversible. In this thesis work, the electrochemical performance of the rGO/NiO modified electrodes was analyzed with the aid of Orygalys 500 electrochemical setup.

# CHAPTER 3

## Synthesis of GO, rGO and electrical properties

### 3.1 Introduction

Owing to the outstanding properties of individual graphene layers, the GO derivatives like rGO, PGN, GQDs and their nanocomposites has significantly drawn more attention in sensing, photovoltaic, energy storage and healthcare Munief *et al.* (2019); Puah *et al.* (2018); Liu *et al.* (2016); Yadav and Kaur (2016); Singh *et al.* (2019) etc. The exceptional material characteristics such as improved surface area and porous nature along with the inherent material characteristics like surface grafting, tailored bandgap, improved electrical conductivity and optical absorption increases the demand of GO derivatives towards various industrial and societal needs.

The GO has a much similar structure like graphene with hexagonal carbon lattice and differs by the number of stacking layers accompanied by the defects. It also possesses active functional groups such as hydroxyl and epoxy formed at their basal plane in addition to carboxyl and carbonyl groups formed at their edges Acik *et al.* (2011); Rezvani Moghaddam *et al.* (2019). Functional groups decorated GO increases the possibility of surface functionalization and it has many fascinating applications than graphene due to its high solubility. The insertion of oxygenated functional groups in between the crystalline plane during the synthesis of GO modifies the electronic bandgap. This changes the local charge carrier mobility and becomes responsible for the new electronic and optical behaviour of the material.

The tuneable bandgap and carrier density is the noticeable property as it can be controlled by the reduction of GO Jung *et al.* (2008); Wei *et al.* (2010a); Gómez-Navarro *et al.* (2009); Yalcin *et al.* (2015). By opening up the bandgap, the charge carrier recombination is reduced with increased photon absorption efficiency Shen *et al.* (2013b). This could be achieved by the transformation of graphene into few layer GO and rGO. The reduction of GO is carried out with distinct methods such as chemical, electrochem-

ical, thermal, laser and microwave Pham *et al.* (2017); Aliyev *et al.* (2019); Quezada-Renteria *et al.* (2019); Sengupta *et al.* (2018); Iskandar *et al.* (2017). Among, temperature controlled reduction of GO In layered graphene like structures experimentally obtainable surface area is far below the theoretical value due to the strong - stacking and van der Waals interactions between graphene sheets. To overcome this problem and achieve higher surface area, graphene porous structures have received increasing interest due to their unique structure with interconnected networks, high surface area and high pore volume Yan *et al.* (2015). These unique properties have highly promising applications in sensing, energy storage and conversion applications Antink *et al.* (2018); Choo *et al.* (2017); Wang *et al.* (2019)

Template dependent and template free protocols are the conventional ways to synthesize porous graphene. The three dimensional macroporous graphene films have been synthesized by Chen and co-workers using uniform polymethyl methacrylate (PMMA) spheres as hard templates Chen *et al.* (2012). Similarly, Zhao *et al.* has utilized hydrophobic interactions with a hard template method to synthesize porous graphene foams Huang *et al.* (2012). Huh *et al.* has utilized polystyrene as sacrificial template with chemically modified graphene to synthesize a 3D macro porous graphene structure Choi *et al.* (2012). Yadav and co-workers have used polymer pyrolysis single step catalyst free process to synthesize single layer graphene assembled porous carbon Yadav *et al.* (2012). Fan and co-workers has demonstrated microwave irradiation using  $KMnO_4$  as oxidizer to synthesize porous graphene Fan *et al.* (2012). There are many other methods such as templating, chemical etching, doping, chemical vapour deposition and ion bombardment reported by different groups to synthesize the porous graphene Chen *et al.* (2011). The current techniques reported are very expensive, low yielding and leaves template residues after etching. These are not viable for practical applications. Therefore, it still remains a major challenge to develop low cost, scalable and template free method to synthesize porous graphene by simple technique.

Moreover, the GO electrical conductivity can be improved by the process of reduction. These rGO structure becomes a more suitable modified transparent and conductive electrode material in numerous applications such as photovoltaic, energy storage, flexible and wearable electronic devices.

In this chapter, the GO was synthesized from graphite powder by the modified Hummers method. GO was further reduced thermally at different annealing temperatures in ambient conditions to obtain the rGO. During this reduction process, the reduction temperature and reduction time was optimized to get PNG. The morphology and structural transformation of GO and rGO were investigated by scanning electron microscopy, X-ray diffraction, and Raman spectroscopy. Further, the a simple route for the reduction of GO films in ambient conditions showing enhanced conductivity has been studied. The observed change in electrical conductance at different reduction temperature has been correlated with infra-red modes. The quantitative analysis of FTIR spectra at different reduction temperature reveals that the change in electrical conductance is related to the degree of reduction which is interconnected to the decrement of functional group and recovery of native carbon bonds in the rGO structure. In comparison with the already existing methods as discussed above, reported results demonstrate a very simple and low cost protocol to synthesize the PGN from GO and a simple way to analyze and relate the electrical properties of rGO films with the structural changes.

## **3.2 Synthesis and thermal reduction of GO**

### **3.2.1 Synthesis of GO**

Initially, GO was synthesized from synthetic graphite powder by the modified Hummers method. In this synthesis, 2 g of graphite powder and 2 g of  $NaNO_3$  were dissolved in 50 ml of  $H_2SO_4$  with stirring for 2 h under ice bath and the black suspension was obtained. Subsequently, 6 g of  $KMnO_4$  which acted as an oxidizing agent was added very slowly with the continuous stirring for 24 h, while the reaction temperature was slowly increased to 35 °C. Brown colour viscous slurry was obtained due to the oxidation of synthetic graphite powder. The viscous slurry comprises GO along with chemically exfoliated sheets and non-oxidized graphite precursor and unconsumed oxidizing agents. Afterwards, 100 ml of distilled water was added in it and put for stirring for an hour at 95 °C. Further, the solution was kept for 24 h without stirring after adding 8 ml of  $H_2O_2$  and 200 ml of  $H_2O$ . Thereafter, this GO solution was ultrasonically exfoliated by keeping it in sonicator bath for an hour. This GO solution was centrifuged at 10,000

rpm and the obtained supernatant solution was washed with 10 % HCl solution and DI water for more than 20 times successively. Finally, the as obtained GO mixture was dried in hot air oven at a temperature of 60 °C for an hour to obtain the GO powder.

### 3.2.2 Thermal reduction of GO

The obtained GO was further reduced thermally at different annealing temperatures (from 200 to 500 °C with an increment of 100 °C) for 10 min in ambient conditions to obtain the rGO. The different samples are named as GO (S1) and rGO at 200 °C (S2), 300 °C (S3), 400 °C (S4) and 500 °C (S5). Thermal annealing of GO at 550 °C showed drastic weight loss and yielded a very less amount of reduced GO which showed the eviction of carbon atoms due to volume expansion of the sample at high temperature Sengupta *et al.* (2018).

### 3.2.3 Structural modification and surface morphology during reduction

The XRD spectrum of GO sample at room temperature and GO annealed at 200 °C, 300 °C, 400 °C and 500 °C in the range of 10° to 80° is shown in Fig 3.1. It clearly exhibits the difference in the XRD patterns of GO and rGO samples. The crystallographic parameter, from the XRD characteristic peaks of each sample, such as interplanar distance ( $d$ ), crystalline stack height ( $L_c$ ), number of average graphene layers in graphene stack ( $n_c$ ) are analysed using Braggs law ( $d = \lambda/2\sin\theta$ ) and Scherrers formula ( $L_c = 0.9\lambda/\beta\cos\theta$ ). The ( $n_c$ ) can be derived using the 'd' value calculations given by ( $n_c$ ) = ( $L_c/d_{001}$  (or)  $d_{001}$ ). The XRD reflection of (001) and (002) planes are taken into account to calculate the above mentioned structural values of GO and rGO samples. The precursor graphite sample normally have sharp diffraction peak at  $2\theta = 26^\circ$  due to (002) plane with the d space value of 0.34 nm. It possesses the maximum number of stacking order with multilayer structure.

The XRD patterns of as prepared GO sample shows a new diffraction peak at  $2\theta = 12.02^\circ$  corresponding to (001) reflection which is a typical characteristic peak of GO. In GO, diffraction peak at  $2\theta = 12.02^\circ$  and corresponding interplanar distance of 0.73 nm,

indicates the oxidation of graphitic layers is due to the chemisorption of oxygenated functional groups and intercalation of water molecules between the graphene oxide layers. It is observed that, with increasing annealing temperature, diffraction peak at (001) gets eliminated and a new intense and broad peak appears at  $2\theta \approx 24^\circ$  in samples S2 to S5. Decrease in interlayer spacing value of 0.36 nm from the annealing temperature of  $200^\circ\text{C}$  clearly exhibits the elimination of functional groups from the GO structure. The peak shift towards higher diffraction angle is related to the turbostratic nature and disordered lattice of the graphitic structure due to reduction. Since the peak width influences the basal spacing parameter, the broadening in the peak width (FWHM) also inhibit the direct change in grain size of graphene sheets during reduction process Claramunt *et al.* (2015). Further, the calculated stacking height ( $L_c$ ) in GO is 7.75 nm with 10-11 layers of GO sheets. Whereas in rGO, S2 sample, the stacking height is reduced to 1 nm with 3 rGO layers per stack. Thus, there observed a reasonable difference in stacking height and decline in average number of layer. The changes in peak width (FWHM) of the (002) peak and the decrease in crystalline stack height indicates the existence of rGO sheets with reconstructed graphitic lattice. Thus, the maximum reduction of GO happens at the annealing temperature of  $300^\circ\text{C}$  and continue up to  $400^\circ\text{C}$  due to the intense dispersion of inserted oxygenated functional groups on the graphene oxide sheets.

The (002) peak of rGO annealed at  $500^\circ\text{C}$  indicated the continuation of reduction. But the peak broadening and appearance of new shoulder peak near  $2\theta = 26.4^\circ$  confirms the change in crystalline size via structural modification at higher annealing temperature. The hydrophilic GO moves towards disordered structure by the loss of functional groups and change of hybridization in between the carbon atoms during reduction.

The (002) plane of GO at  $300^\circ\text{C}$ ,  $400^\circ\text{C}$  and  $500^\circ\text{C}$  is seen at  $2\theta = 24.13^\circ$ ; d-spacing =  $3.62 \text{ \AA}$ ,  $2\theta = 24.93^\circ$ ; d-spacing =  $3.60 \text{ \AA}$ , and  $2\theta = 24^\circ$ ; d-spacing =  $3.65 \text{ \AA}$  respectively. The obtained 'd' value are comparable with some of the previously reported rGO sheets with the  $2\theta$  and d value of  $2\theta = 24.4^\circ$ ; d-spacing =  $3.7 \text{ \AA}$  Mungse and Khatri (2014),  $2\theta = 24.07^\circ$ ; d-spacing =  $3.69 \text{ \AA}$  Qian *et al.* (2021),  $2\theta = 24^\circ$ ; d-spacing =  $3.7 \text{ \AA}$  Tian *et al.* (2017),  $2\theta = 24.1^\circ$ ; d-spacing =  $3.68 \text{ \AA}$  Iskandar *et al.* (2017), and  $2\theta = 25.2^\circ$ ; d-spacing =  $3.5 \text{ \AA}$  Joshi *et al.* (2020) reduced by the techniques like chemical, thermal,



microwave and vacuum assisted high temperature reduction methods. This suggests that the obtained rGO by thermal annealing at ambient condition can also provide ordered rGO sheets with the adequate expulsion of surface functional groups and reconstructed carbon lattice like other reduction techniques

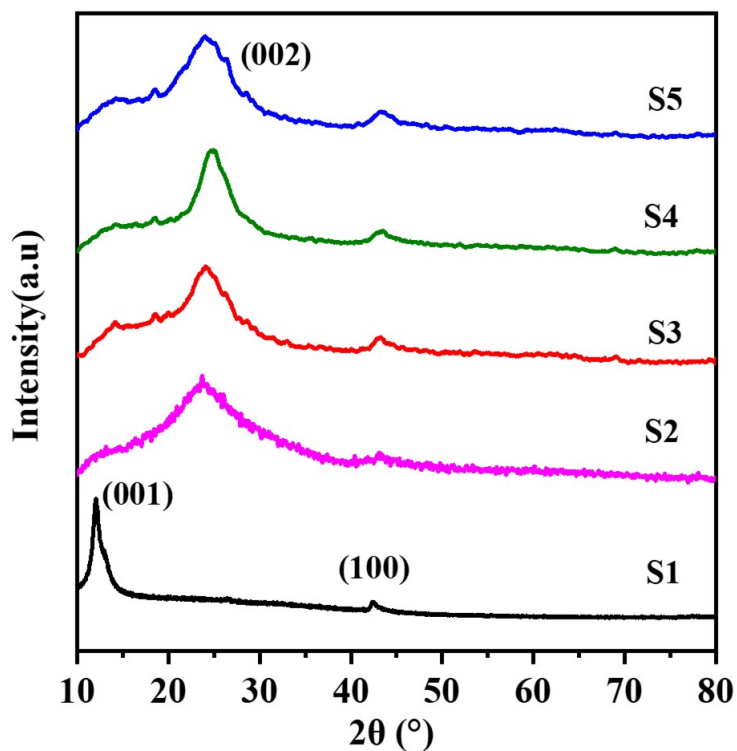


Fig. 3.1: The XRD patterns of GO (S1) and rGO samples at 200 °C (S2), 300 °C (S3), 400 °C (S4) and 500 °C (S5).

Figure 3.2 shows the high resolution scanning electron microscopy images of graphite (S0), GO (S1) and rGO (S2,S3,S4 and S5) samples. The effect of annealing temperature on the morphology of rGO samples is explored using SEM. The SEM micrograph of precursor graphite shows the compressed sheet like multi stack graphitic structure. The oxidation and exfoliation of graphite severely alters the surface morphology of GO with the formation of new grain boundaries. Significant structural changes occurs when the rGO samples were reduced from 300 °C under ambient atmospheric conditions. When, rGO sample is annealed from 300 °C, the SEM image visibly shows the morphology of corrugated and wrinkled rGO sheets with increment in the distance between the GO layers. The formation process of PGN is as follows. During oxidation and reduction, the functional groups will react and yield by-products such as  $CO$  and  $CO_2$  which leads

to the dissociation of carbon atoms and forms carbon dangling bonds Hu *et al.* (2012); Gong *et al.* (2012). The thermal pressure yielded during the release of  $CO$  and  $CO_2$  helps in the exfoliation GOe layers Okhay *et al.* (2016); McAllister *et al.* (2007). This supports the evolution of disordered carbon lattice and increase in the number of defect sites due to the removal of native carbon atoms.

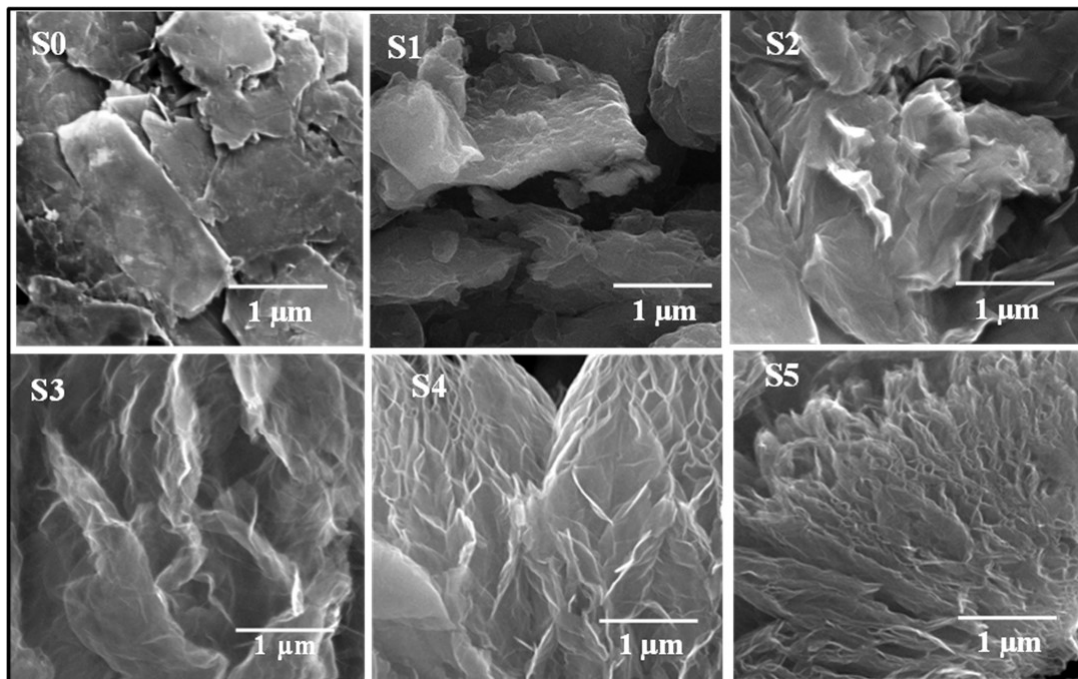


Fig. 3.2: SEM micrographs of Graphite (S0), GO (S1) and rGO reduced at 200 °C (S2), 300 °C (S3), 400 °C (S4) and 500 °C (S5).

So, desorption of oxygenated functional groups supports the delamination effect of the graphene sheets with the formation of wrinkles. But the delamination of GO layers is not fully completed due to the van der Waals interaction Sharma *et al.* (2020); Carrera *et al.* (2020). So, from the temperature of 300 °C, the interconnected pore like structure were opened up compared to 200 °C. This process initiates the significant physical changes in the morphology of rGO samples in terms of wrinkles and pores. The changes in GO structure with the removal of functional groups and residual water molecules also consistent with the obtained XRD spectrum of GO and rGO by the decrement of interlayer spacing from 0.73 nm to 0.36 nm. Thus, the morphology of the as prepared GO samples gets strongly modified by annealing.

Raman scattering can be assigned to investigate the structural changes of oxidized

and reduced graphitic materials. The shape of G mode and the relative intensity ratio of G and D mode are mainly analysed to explore the influence of temperature in GO structure during annealing process.

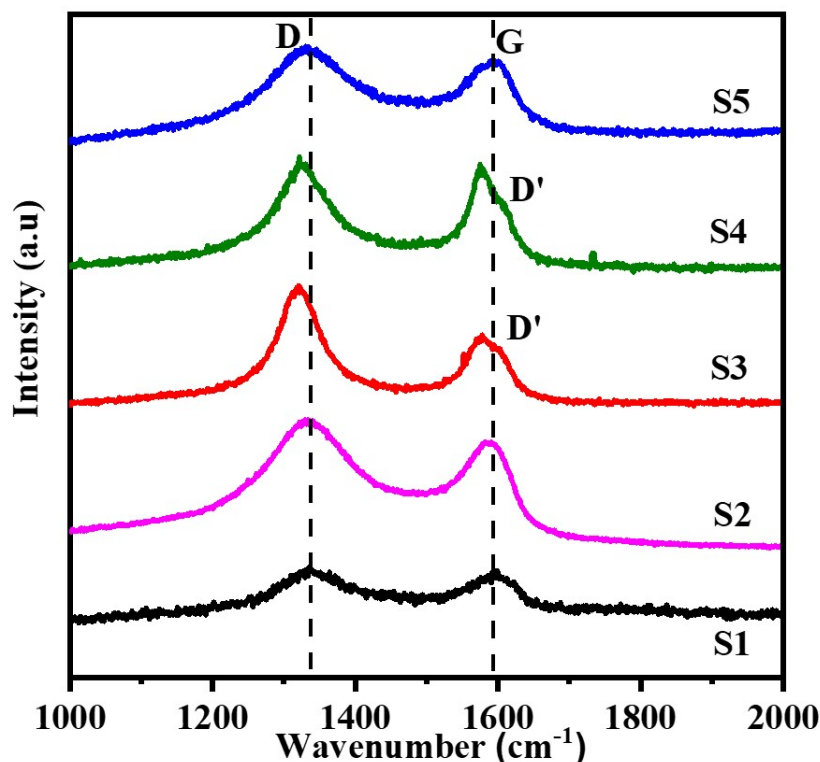


Fig. 3.3: Raman spectra of GO (S1) and rGO reduced at 200 °C (S2), 300 °C (S3), 400 °C and 500 °C (S5).

Figure 3.3 shows the Raman spectra of GO and rGO samples annealed at different temperature. The graphitic and defect modes are denoted by G and D respectively as shown in Fig. 3.3. Here, The intensity ratio of D and G peak (i.e.)  $I_D/I_G$  and peak shift of Raman D and G modes are analysed to get the information about the structural transformation during reduction. Prominent Raman peaks (D and G peak) show the change in peak intensity and peak shift in all the samples. In GO, the peak at  $\approx 1331 \text{ cm}^{-1}$  is denoted as defect induced D peak. This is due to the presence of disorder/defect. Tuinstra and Koenig (1970) have allocated the D band as longitudinal acoustical  $A_{1g}$  phonon vibration mode of the smaller crystallites or boundaries of larger crystallites of graphitic like structures. Here, red shift of D mode is observed from samples S3 to S5. This observed shift may be due to the distortion of carbon bonds during elevated

annealing temperature and the curvature effect at the grain boundaries of carbon lattice.

In GO, the Raman G peak is observed at  $1598\text{ cm}^{-1}$ . This corresponds to the longitudinal optical (LO) phonon mode at the zone centre of the graphitic lattice. In G peak, a new shoulder peak (called D peak) is observed at  $1603\text{ cm}^{-1}$  and  $1608\text{ cm}^{-1}$  in samples S3 and S4 respectively. This D' peak is, also due to the defects as same as the D peak but due to the scattering of the smaller wave vector optical phonons.

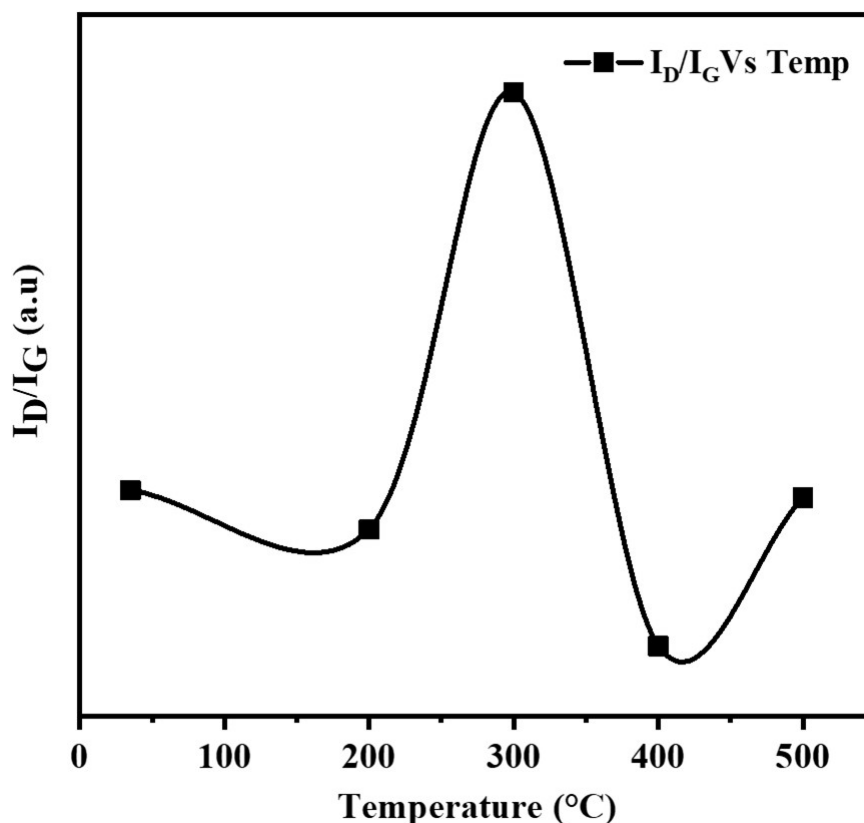


Fig. 3.4: Temperature Vs Peak intensity ratio of D and G peak for GO (S1) and rGO annealed at reduction temperature of  $200^\circ\text{C}$ ,  $300^\circ\text{C}$  (S3),  $400^\circ\text{C}$  (S4) and  $500^\circ\text{C}$  (S5).

Peak broadening and red shift of the G mode was observed when GO was annealed from  $200^\circ\text{C}$  to  $400^\circ\text{C}$  and returns back to the position  $\approx 1594\text{ cm}^{-1}$ , which is closer to the G mode frequency of GO at  $500^\circ\text{C}$  as shown in the Fig.3.3. This may be due to the deformation of carbon lattice by the intensification of larger defect concentration which stimulates the incorporation or merge of G and D' peak Eckmann *et al.* (2012). So, the splitting of G peak as G and D' will be only visible at the moderate concentration of defects.

The intensity ratio of D and G peak  $I_D/I_G$  shows a nonlinear relationship with increase in annealing temperature from samples S1 to S5 as shown in Fig 3.4. The maximum intensity ratio is observed for rGO 300 °C (S3) that indicates the higher lattice deformation since the intensity ratio is related to the defect density Ferrari (2007). Further,  $I_D/I_G$  decreases for S4 sample again a slight increase in intensity ratio was observed for S5 sample. These results are following similar behaviour as the observed shift in Raman G mode in samples S1 to S5. This also indicates the possible structural reconstruction with the recovered carbon lattice and change in defect concentration during thermal annealing of GO in ambient conditions.

Thus, the changes in physical and chemical structure of carbon lattice happen during the oxy-reduction stages. Oxygenation induces the insertion of functional groups which alter the bond length between the carbon atoms and initiates the defects formation Larciprete *et al.* (2011). During the reduction, rigid topological and/or structural deformation happens in the samples due to thermal expansion of carbon lattice followed by eviction of in- plane carbon atoms. The GO and rGO samples show the peak shift due to thermal strain induced lattice distortion contributed by the anharmonic phonon coupling effect Calizo *et al.* (2007); Martins Ferreira *et al.* (2010); Eigler *et al.* (2012). The defects induced in the graphitic structure by external perturbation are mainly responsible for the observed shift in Raman peaks. The lattice reconstruction due to thermal annealing in GO and rGO is also evident from the change in XRD peak position and peak broadening, which is directly related to the interplanar spacing and crystalline size of GO sheets.

Further, the better understanding of structural modification in GO during the oxo-reduction stages, a methodology based on Raman scattering is proposed and discussed in chapter 4.

### **3.3 Electrical conductivity of rGO: effect of thermal reduction**

Different approaches had been involved in the reduction process of GO such as thermal, chemical, photochemical, electrochemical, microwave and laser assisted methods Shi

*et al.* (2019); Kumar *et al.* (2015); Zeng *et al.* (2019); Faucett *et al.* (2017); Liu *et al.* (2013); Aminuddin Rosli *et al.* (2021). But unlike other techniques, thermal reduction allows us to manipulate the degree of reduction by simply varying the reduction temperature Savchak *et al.* (2018); Bernal *et al.* (2017). During the reduction, the GO will form the restored  $sp^2$  hybridized carbon nano clusters with the adequate removal of oxygenated functional groups Wang *et al.* (2018b). This will provide the percolation pathway for the hopping of charge carriers, as reported by Gómez-Navarro *et al.* (2010).

Thus, the rGO with tailored bandgap behaves like semi metal or semiconductor and its electrical conductivity can be tuned by controlling degree of reduction Tu *et al.* (2015). Thermal reduction of rGO was reported by Dolbin *et al.* (2017); Chua and Pumera (2012); Slobodian *et al.* (2018); Sengupta *et al.* (2018). Zhang *et al.* (2018) has shown high reduction degree is possible in thermal reduction than chemical reduction. Muchharla *et al.* (2014) reported a green chemically reduced rGO structures and exposed the Arrhies like temperature dependence of conductivity and Motts two dimensional variable range hopping mechanism of rGO at different temperature regime. Bhaskaram and Govindaraj (2018) described the variable range hopping type electrical conductivity of chemically reduced rGO via temperature dependent Raman spectroscopy analysis by exploring the electron-phonon coupling behaviour. Ma *et al.* (2019a) reported the temperature dependent conductivity and the semiconduction behaviour of chemically reduced rGO by comparing different charge conduction models. There still require a simple method to get the conductive rGO films and a simple method to analyse the electron transport behaviour, as rGO is quite different from graphene but have equivalent potential applications.

### **3.3.1 Experimental details**

The obtained GO powder using Hummer's method was dispersed in ethanol with 1 mg/ml of concentration and ultrasonicated for 60 min. It makes the graphene oxide powder to distribute uniformly over the solution. A glass substrate was cleaned with soap solution and bath sonicated with acetone, ethanol and deionized (DI) water, respectively. The GO solution was drop casted over the glass substrate in the form of small channel 1.0 cm (L)  $\times$  0.5 cm (W) by using a micropipette and dried at room

temperature. Al electrodes were deposited for contact. The corresponding IV characteristics have been measured using Keithley, 2614b source meter, four probe technique at different annealing temperatures. Thermal reduction of the samples was performed in the temperature range from 100 to 350 °C in ambient atmosphere. Here, the different samples are named as GO (S1) and rGO at 100 °C (S2), 150 °C (S3), 200 °C (S4), 250 °C (S5), 300 °C (S6) and 350 °C (S7).

### 3.3.2 Electrical conductivity: Result and Discussion

The accurate measurement of electrical conductivity is a real hurdle for materials like rGO due to discontinuity in film thickness along with the concomitant effect of substrate and electrode materials. The electrical conductivity characteristics of the GO on the glass substrate was studied with Keithley Source Meter 2614B. **Totally five samples have been analysed. All the I-V measurements done are reproducible in these samples within the error range of 2-3 %.** The Current-Voltage loop of the few layer GO and rGO were analyzed using DC voltage sweep measurements at ambient atmosphere and it is illustrated in a semilogarithmic scale. Figure 3.5 shows the I-V curve of GO and rGO samples at different annealing temperature with an input voltage range of -3 to +3 V.

The maximum current obtained for S1 is  $2 \times 10^{-8}$  A and it shows lower conduction value. The GO exhibits a high electrical resistance state at room temperature. During the initial stage of reduction, the volatile by-products evolved from the solvent and the surface functional groups were diffused and trapped in between the GO layer thus dropping the charge transport Slobodian *et al.* (2018). When the temperature was increased above the room temperature, there observed a noticeable change in the conductivity of GO. The insulating nature of GO might be due to the mixed  $sp^2$ - $sp^3$  bond nature, edge defects and the residual moisture present in the as dried GO sample Okhay *et al.* (2016); Zeng *et al.* (2018).

When GO sample was heated from room temperature to 100 °C, it shows the current value in the range of  $10^{-12}$  to  $10^{-10}$  A. Heating sample S2 at 100 °C, the moisture and the residual ethanol content exist on the sample is evaporated from the GO layers. This leads to the constriction of the charge carriers and discontinuity in charge transport by the formation of low conductive GO island structure Chen *et al.* (2016b). Hence there

exists more resistance between the charge carriers that results in the reduction of current in sample S2. Further annealing of samples S3, S4, S5, S6 and S7 at temperatures 150, 200, 250, 300 and 350 °C respectively shows an enhancement in current value.

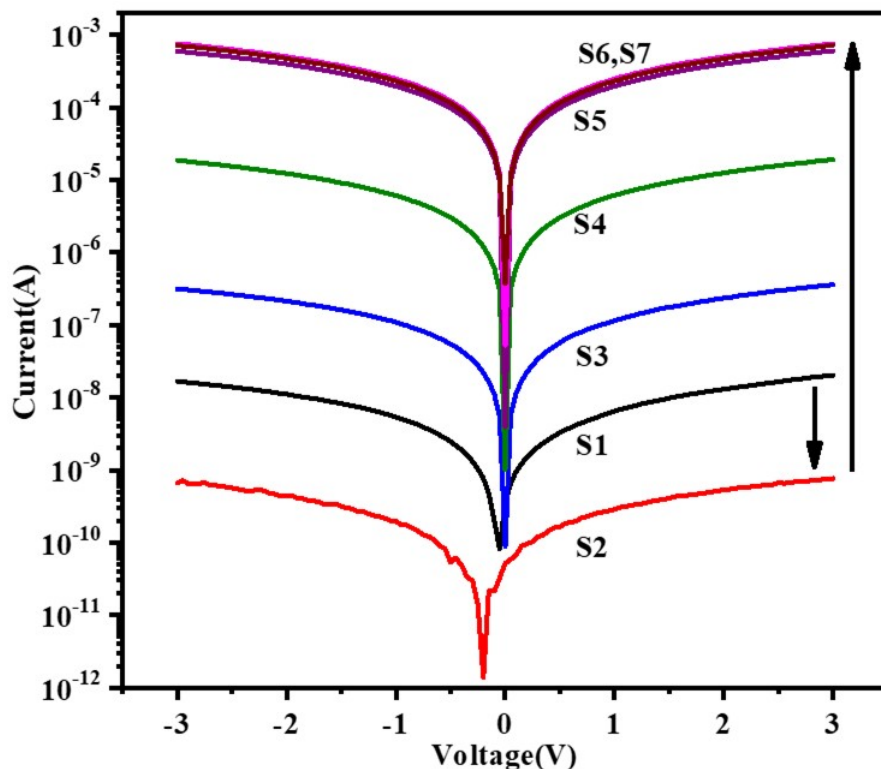


Fig. 3.5: IV Characteristics of GO (S1) at room temperature and rGO annealed at 100 °C (S2), 150 °C (S3), 200 °C (S4), 250 °C (S5), 300 °C(S6) and 350 °C (S7)

Among others, the sample S6 shows the maximum conductivity with the observed value of 2.4 S/cm. Also, the obtained current value for the sample S6 and S7 was almost same with the negligible difference in electrical conductance. Further increase the annealing temperature above 350 °C shows very slight changes in current value due to the adequate level of GO reduction. So the electrical conductance is shown upto 350 °C without further increase of annealing temperature. Thermal reduction brings more restored  $sp^2$  carbon bonds to the rGO structure and improves and carrier transport with increases in conductivity. The I-V Characteristics has also been measured during the cooling cycle after annealing at 350 °C. It hardly shows variation in current value and falls in the same range between  $10^{-4}$  to  $10^{-3}$  A for all the temperatures. This might be due to the fact that the rGO has reached the adequate level of reduction at 350 °C. Hence it could not be reversed to form GO due to the removal of enough functional



groups present from the rGO. On this factor it shows a poor variation in the current from GO 350 °C to GO room Temperature. The I-V characteristic of rGO during the cooling cycle is provided in Fig. 3.6.

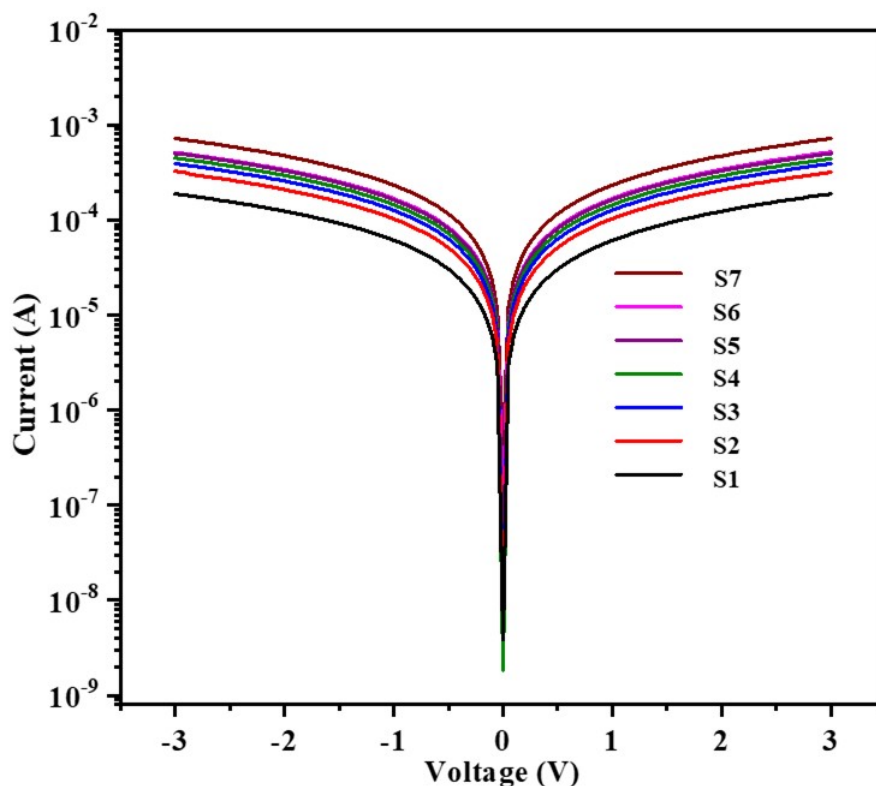


Fig. 3.6: I-V Characteristics of rGO at fixed temperature of ramped down from 350 °C to 35 °C during cooling cycle.

Structural transformation during annealing plays an important role in the conductivity of graphene derived materials due to regeneration of  $sp^2$  domain and formation of defect sites during heating Okhay *et al.* (2016). The HRTEM images of GO at different reduction temperature in Fig 3.7 visibly indicates the lattice fringes with the change in interplanar spacing during the reduction process. From 100 °C, interlayer spacing of GO started to decrease slowly due to the evaporation of intercalated water molecules and other functional groups. The lattice distortion is more visible for S6 and S7 at the higher annealing temperature of 300 °C and 350 °C. **The term lattice distortion signifies the disorientation of atoms from the lattice structure in an ideal crystal structure. This will create a structural disorder due to the misalignment and eviction of native atoms from the lattice.** In the present study, the expulsion of native carbon atom along with desorption of oxygenated functional groups create defects in the graphitic lattice during

the reduction process. Therefore, the defects are seen as structural modification over the graphitic plane during reduction of GO.

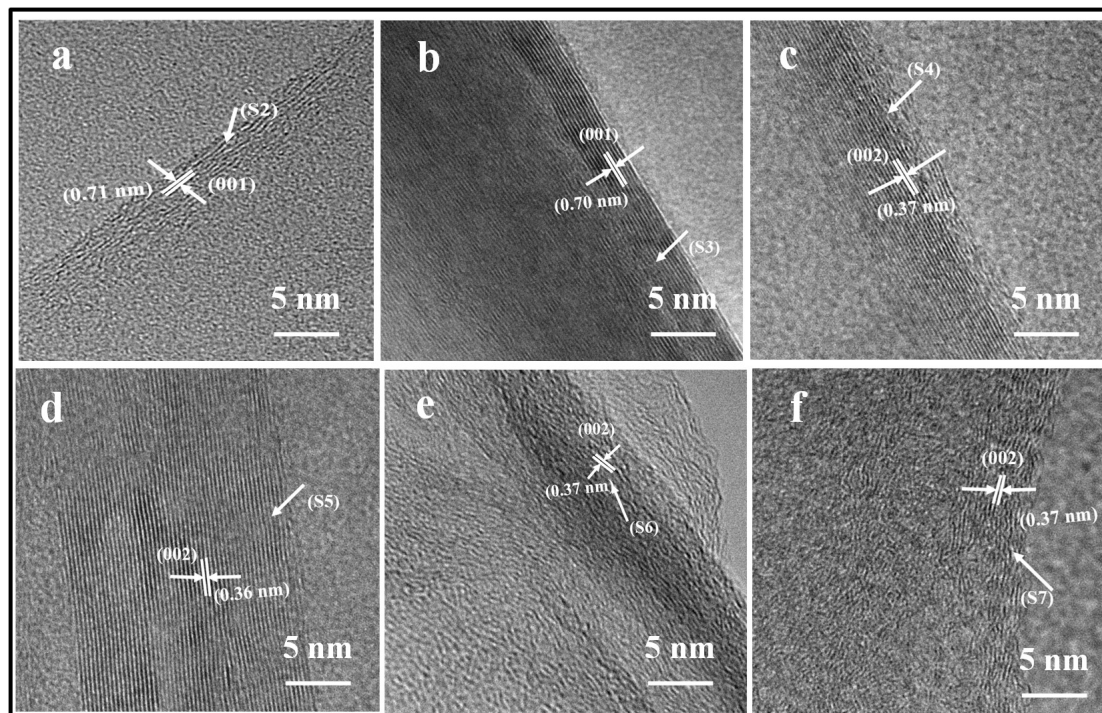


Fig. 3.7: HRTEM images of rGO at different reduction temperature: a and b high resolution (001) lattice plane images of rGO reduced 100 and 150 °C (S2 and S3) and c-f high resolution (002) lattice plane image of rGO reduced 200 °C (S4), 250 °C (S5), 300 °C (S6) and 350 °C (S7)

Unlike the vacuum and inert conditions, annealing at ambient condition activates both oxidation and reduction in the GO samples. Thermal reduction of GO is called principally as an organic disproportionation or decomposition reaction reported earlier by Y. Qiu et al Qiu *et al.* (2016).

The reaction step of thermally assisted GO reduction is expressed in eqn 3.1 Soni *et al.* (2018).



Thermal reduction of GO is definitely a discrete process. The deoxygenation of GO is assisted with the degassing of  $H_2O$ ,  $CO_2$ ,  $CO$  and during thermal annealing Soni *et al.* (2018).

The elimination of surface functionalities and the formation of carbon bonds during GO reduction was studied using XPS analysis. Figure 3.8 a shows the XPS survey

spectrum of S2, S3 and S7 samples. The deconvoluted peak of C1s signal from S2, S3 and S7 is comprised of four different signals as shown in Fig 3.8 b, c and d. They are C-C/C=C in aromatic rings (284.4 eV), C-O (285.2 eV), C=O (286.7 eV), and O=C-O (287.9 eV) groups observed in XPS spectrum of rGO samples.

The C-C bonds corresponds to the  $\pi$  conjugated carbon atoms in the GO lattice. The C-O bonds evolves from hydroxyl and epoxy groups exist in the GO basal plane. The C=O group arises as carbonyls from the edges of the GO lattice plane as well as from the basal plane. The carboxyl groups (O=C-O) are mainly developing from the edges of the graphitic lattice. Different C-O bonds develops during the different phases of oxidation and reduction process.

The level of oxidation was calculated from the peak area ratio of C1s and O1s using XPS spectra. The XPS peak reveals that the S2 has a very less C/O ratio of 2.2 than other annealed rGO samples. This shows the higher oxidation level of S2 sample with less reduction of other functional groups at the annealing temperature of 100 °C. The evaporation of  $H_2O$  from the GO layer accompanied with the trapping of C-O species by introducing carbon dangling bonds with the atmospheric oxygen. This progresses the oxidation level of S2 and decreases the C/O ratio.

In contrast, increasing of reduction temperature above 100 °C improves the functional groups desorption and  $sp^2$  bond restoration observed from the increment in C/O ratio of 4.9 and 5.1 for S4 and S7. The peak intensity of other carbonyl, and carboxyl groups such as C=O and O=C-O also reduces with the increase in annealing temperature observed from Fig 3.8. So, the non-oxygenated carbon percentage was improved by the formation of new C-C bonds in rGO structures during reduction. This signifies the GO reduction accompanies with the ejection of water molecules followed by the degassing of surface functionalities with the reconstructed carbon lattice.

Further, the FTIR spectra Fig.3.9 are quantified by measuring the peak area under the functional groups and analysed at every reduction temperature to observe the dominance of oxygenated functional groups over the conductivity of rGO as shown in Fig 3.10. The decrement of functional groups intensity during thermal reduction explored from the FTIR peak analysis suggest that deoxygenation reaction was started at low temperature.

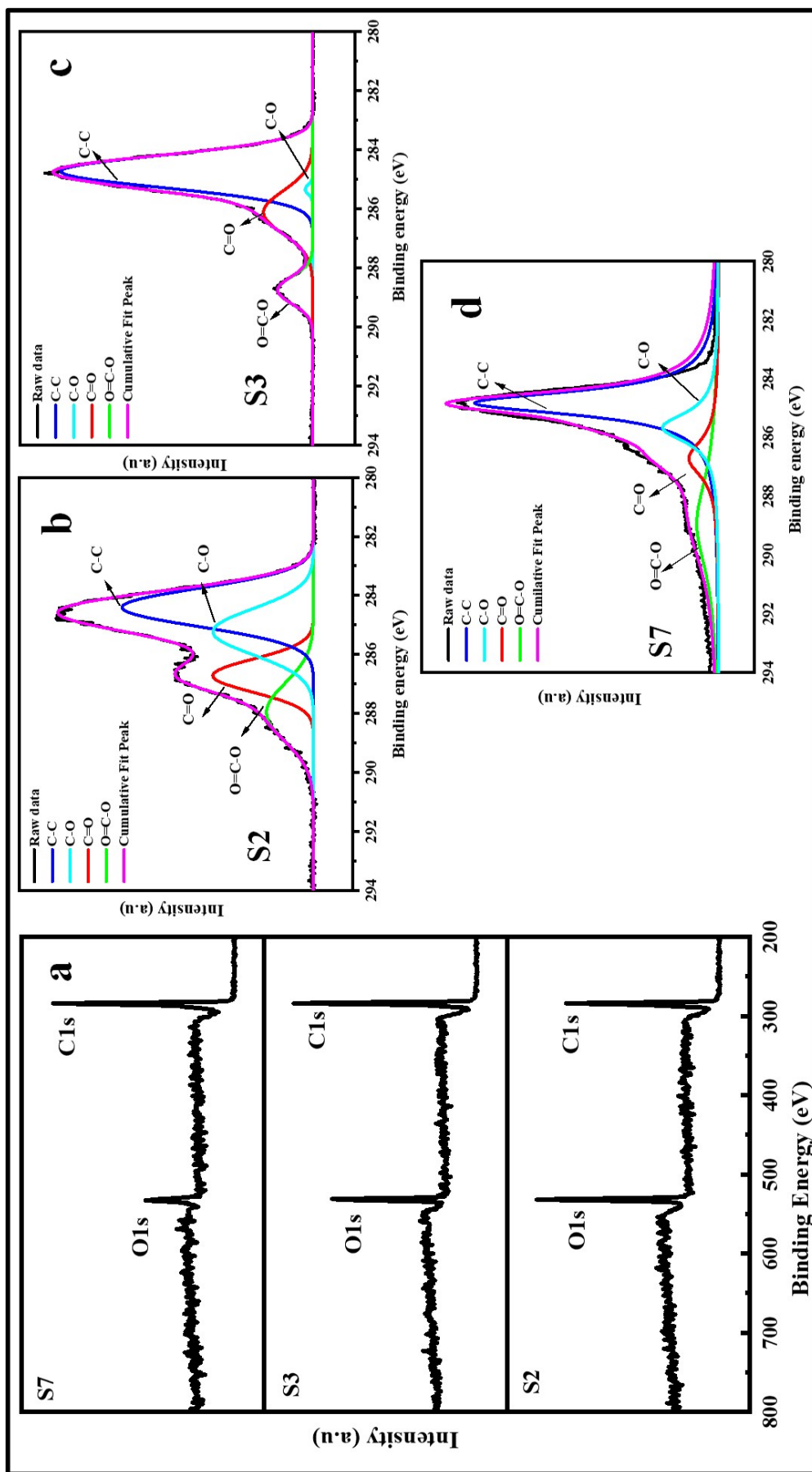


Fig. 3.8: XPS spectra of GO at different annealing temperature: (a) survey spectrum of rGO @ 100 °C (S2), 150 °C (S3), and 350 °C (S7). High resolution deconvoluted C1s peak image of (b) rGO @ 100 °C (S2), 150 °C (S3), and 350 °C (S7)

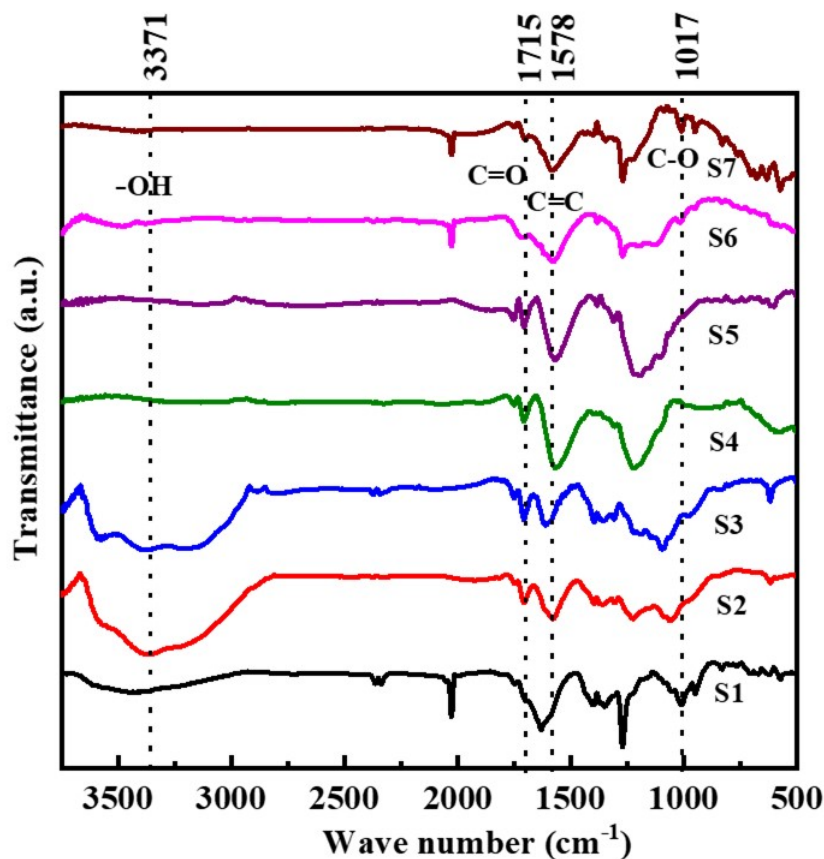


Fig. 3.9: FTIR spectra of as prepared GO (S1) and rGO @ 100 °C (S2), 150 °C (S3), 200 °C (S4), 250 °C (S5), 300 °C(S6) and 350 °C (S7)

The -OH group stretching vibration at  $3371\text{ cm}^{-1}$  is observed for the samples from S1 to S3 with a noticeable variation in peak area as shown in Fig 3.9. The reduction without inert atmosphere and vacuum significantly improves the amount of hydroxyl group due to oxidation at 100 °C. So, the observed -OH bond peak area is more for S2 than the S1 due to the ambient atmosphere. Further increase in temperature from 150 °C substantially improves the evaporation of water molecules and removal of hydroxyl groups from the basal plane, thereby reduces the -OH peak in samples from S3 to S7. The hydroxyl group reduces progressively until 200 °C and then it becomes slower due to ambient annealing condition. Similarly, the band at  $1578\text{ cm}^{-1}$  for the stretching vibration of C=C bond of graphene plane was registered for all the samples from S1 to S7. But the intensity of  $1578\text{ cm}^{-1}$  peak is increased further for the GO samples from S4 to S7 signifies the restoration of carbon bonds during the process of reduction. The stretching vibration of carbonyl (C=O) groups at  $1715\text{ cm}^{-1}$  evolved from the edges of

the GO and rGO layers. The desorption of C=O groups from the edges of rGO layer is observed at elevated annealing temperature from sample S1 to S7.

It is observed from the Fig.3.10 that transition of GO to rGO occurs at the critical reduction temperature of 200 °C because the changes in the active functional groups of GO are very less above 200 °C during the process of reduction.

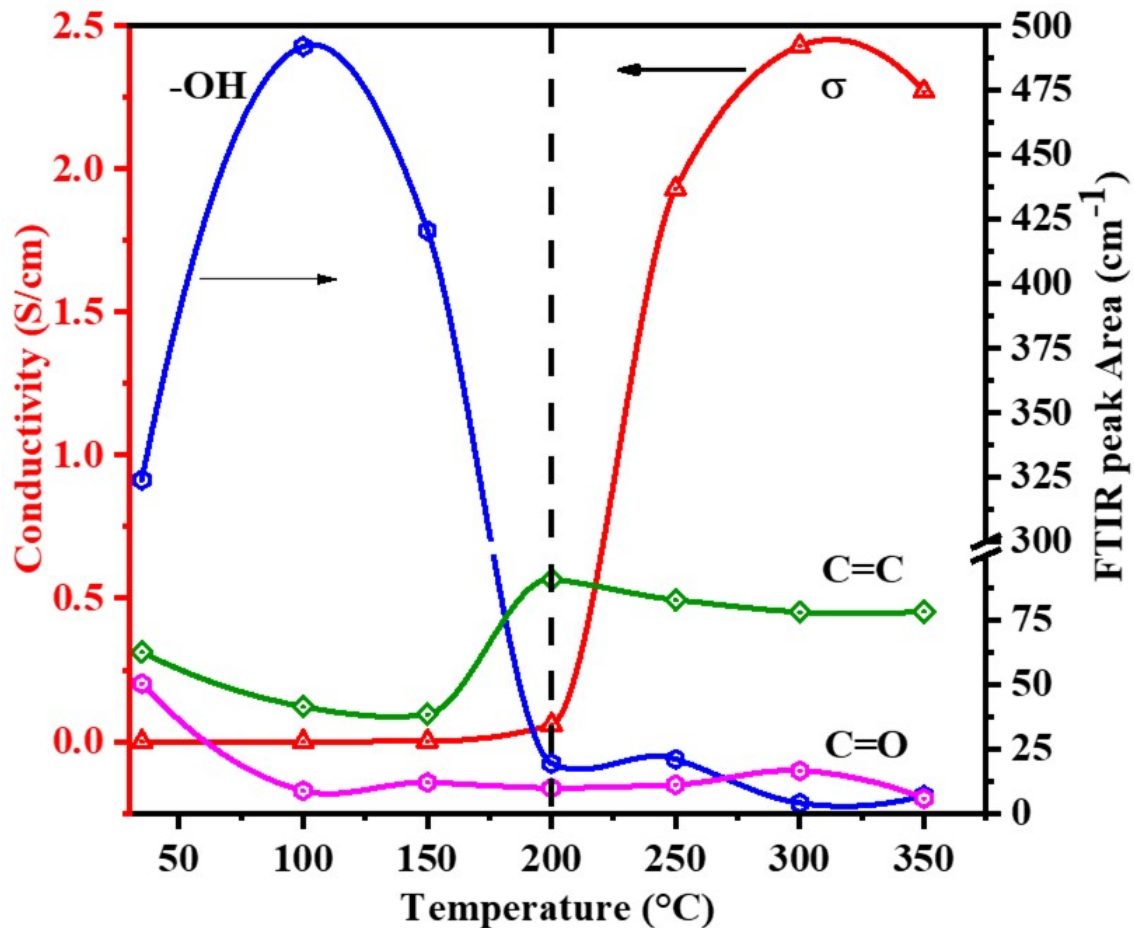


Fig. 3.10: Correlative graph of electrical conductivity of GO/rGO channel and peak area of GO/rGO samples obtained from FTIR spectra with reduction temperature

The structural modification with restored C=C bonds is also observed with the increased peak area for the rGO samples above 200 °C. The electrical conductivity of rGO above 200 °C increases due to the expulsion of oxygenated functional groups together with the thermally modified  $sp^2$ - $sp^3$  hybridized carbon network as shown in Fig. 3.10. So, the observed variation in the electrical conductivity during increase in temperature is a real time indication of structural modification of GO during reduction. This method

improves the reduction process by minimizing the effect of solvent in comparison to other deposition techniques. It also, enables to control the electrical conductivity of the rGO channel by simply managing the degree of reduction.

### **3.4 Conclusion**

In summary, a facile and scalable fabrication approach has been developed to synthesize PGN. Initially, GO was synthesized from graphite powder by modified Hummer's method. A detailed structural (microscopic and diffraction) studies establishes that porous graphene network can be synthesized from graphene oxide obtained by modifying the graphite. Structural and spectroscopic investigations shows that GO starts reducing at the temperature of 200 °C that is explicitly clear from the change in inter-layer spacing, XRD and removal of functional groups, FTIR. The interconnected pore like structure was obtained from the temperature of 300 °C. SEM results clearly show the formation of PGN. Structural reconstruction is evidently observed from the Raman peak shift and intensity ratio of the D and G peaks in GO and rGO samples using the Raman spectroscopy analysis. The correlation between the electrical conductivity and the functional group of rGO was probed using FTIR spectroscopy. The increase in electrical conductivity of rGO films is correlated with improved charge transfer promoted by the elimination of hydroxyl, epoxy functional groups and recovery of native carbon bonds during reduction. It is obtained that the electrical conductance of rGO films can also be tuned by optimizing the reduction temperature. These results show that the obtained rGO open up the exciting opportunities and have the potential to replace the existing TCO layer in photovoltaics and also suitable for a wide range of applications in sensing, energy storage, flexible electronics and optoelectronics.

# CHAPTER 4

## First order Raman scattering to analyse defects in GO and rGO

### 4.1 Introduction

The structural modification in the  $sp^2$ - $sp^3$  hybridized GO derivatives evolves with defects during the growth process, either physically or chemically. The type of defects, 0D (point defects) and 1D (line defects), may change from one sample to another sample that fully relies on the synthesis method. Regardless of the diverse application, graphene derivatives like GO and rGO are always accompanied by defects that generally evolve during the synthesis and reduction steps. The different processes involved during the synthesis of graphene derivatives play a crucial role in developing defects; besides, they cannot be avoided. Structural changes in the material in terms of change in the number of stacking layers, the addition of reactive chemical groups, and varying the degree of oxidation are also considered as a source of defects Tian *et al.* (2017); Pham *et al.* (2017); Aliyev *et al.* (2019); Gong *et al.* (2012).

Lattice deformation also happened during the oxidation and reduction stages Kumar *et al.* (2015). The reduction of GO is done with distinct methods such as chemical, electrochemical, thermal, laser and microwave methods. The process methods led to an evolution of new graphene based structures with the change in grain size and development of defects Ma *et al.* (2019a); Quezada-Renteria *et al.* (2019); Sengupta *et al.* (2018); Bagri *et al.* (2010). The type and quantity of the defects existing in the material after reduction highly impacts the characteristics of carbon based materials such as carrier density and mobility Tu *et al.* (2015); Gómez-Navarro *et al.* (2009); Eda *et al.* (2009); Peres *et al.* (2006).

Single layer graphene is considered as an ideal material for the defect analysis than GO and rGO due to the more accessible inclusion and exclusion of carbon atoms and



other dopant atoms from the two-dimensional graphitic lattice. There are earlier studies on the defect mechanism of graphite and single layer graphene through theoretical and experimental predictions useful in exploring the density, type and functionality of defects Claramunt *et al.* (2015); Eckmann *et al.* (2012); King *et al.* (2016). The evolution and types of defects on graphitic structures are often interpreted with the non-destructive and high-resolution method of Raman spectroscopy.

Raman spectroscopy is an efficient, powerful technique for the structural analysis of graphene based materials. It gives qualitative information of the material, including dopants, the nature of carbon bond, an abundance of  $sp^2$  and  $sp^3$  bonds, crystallite size and defects through peak position, peak intensity and line width. These parameters are used to analyze the defect states, defect intensity and crystallite nature, as well as the electronic property of carbon based materials Ferrari (2007); Sood *et al.* (2001); Ferrari *et al.* (2006); Tang *et al.* (2010); Eigler *et al.* (2013); Ryu *et al.* (2010).

The well known T-K model for graphitic materials predicts the degree of defects by comparing the intensity ratio of D and G peak with the inverse of the crystalline size  $L_a$  Tuinstra and Koenig (1970). This will be suitable for the graphene sheets with very less defect density with inter-defect distance above 2 nm ( $L_a > 2$  nm). However, no further dependency of T-K model for graphene sheets with a very smaller crystallite size ( $L_a < 2$ nm) was reported by Ferrari *et al.* Ferrari (2007). So, carbon structures with smaller crystallites size ( $< 2$ nm) are interpreted by the Ferrari-Robertson relation  $(I_D/I_G) \propto L_a^2$ . Lucchese *et al.* quantified the disorder in Graphene induced by ion implantation with  $(I_D/I_G)$  ratio Lucchese *et al.* (2010). Similarly, L.G.Cancado *et al.* discussed the influence of the Raman cross section of D,  $D'$  and 2D over the in-plane crystalline size ( $L_a$ ) of nanographites and analyzed the dependency of  $L_a$  with  $(I_D/I_G)$  ratio Cançado *et al.* (2007). Eckmann *et al.* predicted the nature of defects like vacancy and  $sp^3$  hybridization by probing the intensity ratio of defect activated peaks such as D and  $D'$  ( $I_D/I_{D'}$ ) Eckmann *et al.* (2012).

Recently, L.G. Cancado *et al.* reported the contributions of 0D and 1D defects such as point and line defects of Graphene related materials by comparing the ratio of the integrated area of D and G peak ( $A_D/A_G$ ) with line width of G peak Cançado *et al.* (2017). For identifying defect type in a sample with intermixed defect density with

distinct  $L_a$  and  $L_D$  (distance between the point defects) value, the analysis of peak intensity scarcely provides the spectral details about the structural disorientation. Instead, the contribution of integrated peak area Raman D and G is more required to depict defect contribution over the structural evolution of graphene oxide derivatives. In this chapter Raman spectroscopy analysis is used to probe the nature of defects evolved in the rGO structure during thermal annealing process. The fortuitous change of crystalline size  $L_a$  of GO and rGO during oxo-reduction stages at ambient condition makes a non-linearity with the relative intensity of D and G peak ( $I_D/I_G$ ). Some of the results reported in the recent defect studies on GO in a controlled environment also interpreted the non-dependency and discontinuity of  $I_D/I_G$  ratio only with  $L_a$  value Claramunt *et al.* (2015); King *et al.* (2016).

Irrespective of the reaction environment, the present study also correlated with the above phenomenon. Also, by considering the predominant role of defects, it is necessary to build an accurate method to analyze the highly disoriented GO and rGO sheets. So, the essence of this work is to propose an approach for the interpretation of defect type and density present on the highly defective GO and rGO sheets. And also to examine the change in microstructure with the evolution of new peaks associated with the defects during different reduction stages at ambient atmospheric conditions using crystallographic analysis techniques such as Raman Spectroscopy and XRD methods. Clear understanding of defects and disorders in Graphene derived materials like GO and rGO is always very important for further refinement of material structure and incorporating this material into device structure.

## **4.2 Experimental method**

### **4.2.1 Synthesis of graphene Oxide**

GO was synthesized from graphite powder by the modified Hummers method. GO (named as S1) was further reduced thermally at different annealing temperatures in ambient atmospheric condition for 10 mins at 200 °C (S2), 300 °C (S3), 400 °C (S4) and 500 °C (S5) to obtain the rGO. Recorded patterns of X-ray Diffraction were obtained by PANalytical XPERT powder diffractometer with a high intensity CuK radiation

( $\lambda=1.540 \text{ \AA}$ ) in the range from  $10\text{-}80^\circ$  at  $2\theta$  angle. Identification of functional groups was investigated by Fourier Transform Infrared (FTIR) Spectroscopy using PERKIN ELMAR; SPECTRUM RXI. Room temperature Raman spectra of GO and rGO sheets were analyzed using LabRAM HR Evolution, Horiba micro-Raman spectrometer with the excitation wavelength of 633 nm. Lorentzian fitting was identified as an excellent fitting function compared with other functions such as Gaussian and Voigt to fit the peaks such as D, G and D' in the range of  $1000\text{-}2000 \text{ cm}^{-1}$  during the analysis. The crystal structure and morphology of GO and rGO were obtained by HRTEM analysis obtained using (JEOL JEM 2100 operated at an acceleration voltage of 200 kV). XPS measurements were taken by physical electronics PHI5000 XPS model, and the sample was excited by Al  $K\alpha$  source.

## 4.3 Results and Discussion

### 4.3.1 Structural analysis

Figure 4.1 shows the X-ray diffraction (XRD) patterns of the GO at room temperature and GO annealed at different reduction temperatures from  $200^\circ$  to  $500^\circ \text{ C}$  with the increment of  $100^\circ \text{ C}$  at the range of  $10^\circ$  to  $80^\circ$ . The difference in the X-ray diffraction (XRD) patterns of GO and rGO samples with the shift in the scattering angle ( $2\theta$ ) clearly exhibits a change in the crystalline nature during the oxidation and reduction process Claramunt *et al.* (2015). For GO, the observed ( $2\theta$ ) at nearly  $12^\circ$  with the increment in the interplanar distance ( $d$ ) of 0.8 nm implies the (001) plane of the oxidized GO structure. In addition to the oxidized GO peak at ( $2\theta$ ) at nearly  $12^\circ$ , a new peak at ( $2\theta$ ) =  $26^\circ$  arises for the sample S2 at  $200^\circ \text{ C}$ . This signifies the change in oxidation level with the effect of reduction temperature. From the reduction temperature of  $300^\circ \text{ C}$  to  $500^\circ \text{ C}$  there observed the absence of (001) peak. As well as reduction process recovered the (002) plane towards  $2\theta = \pm 24^\circ$  for rGO annealed above  $300^\circ \text{ C}$ . The above peak is related to the reconstructed lattice of the reduced GO structure during annealing due to the intense dispersion of inserted oxygenated functional groups on the GO sheets. The changes in peak width (FWHM) of the (002) peak imply the decrease in crystalline stack height with the existence of a few reduced graphene sheets in the

annealed GO sample. The thermally induced reduction with the declined interplanar spacing is the reason behind the shifting of the (002) peak towards a higher diffraction angle. During oxidation and reduction, the peak shift accompanied with the peak broadening directly specifies the variation in the crystalline nature of GO during oxidation and reduction. The hydrophilic GO moves towards disordered structure by losing functional groups and hybridization change between the carbon atoms during ambient annealing atmosphere Hu *et al.* (2012).

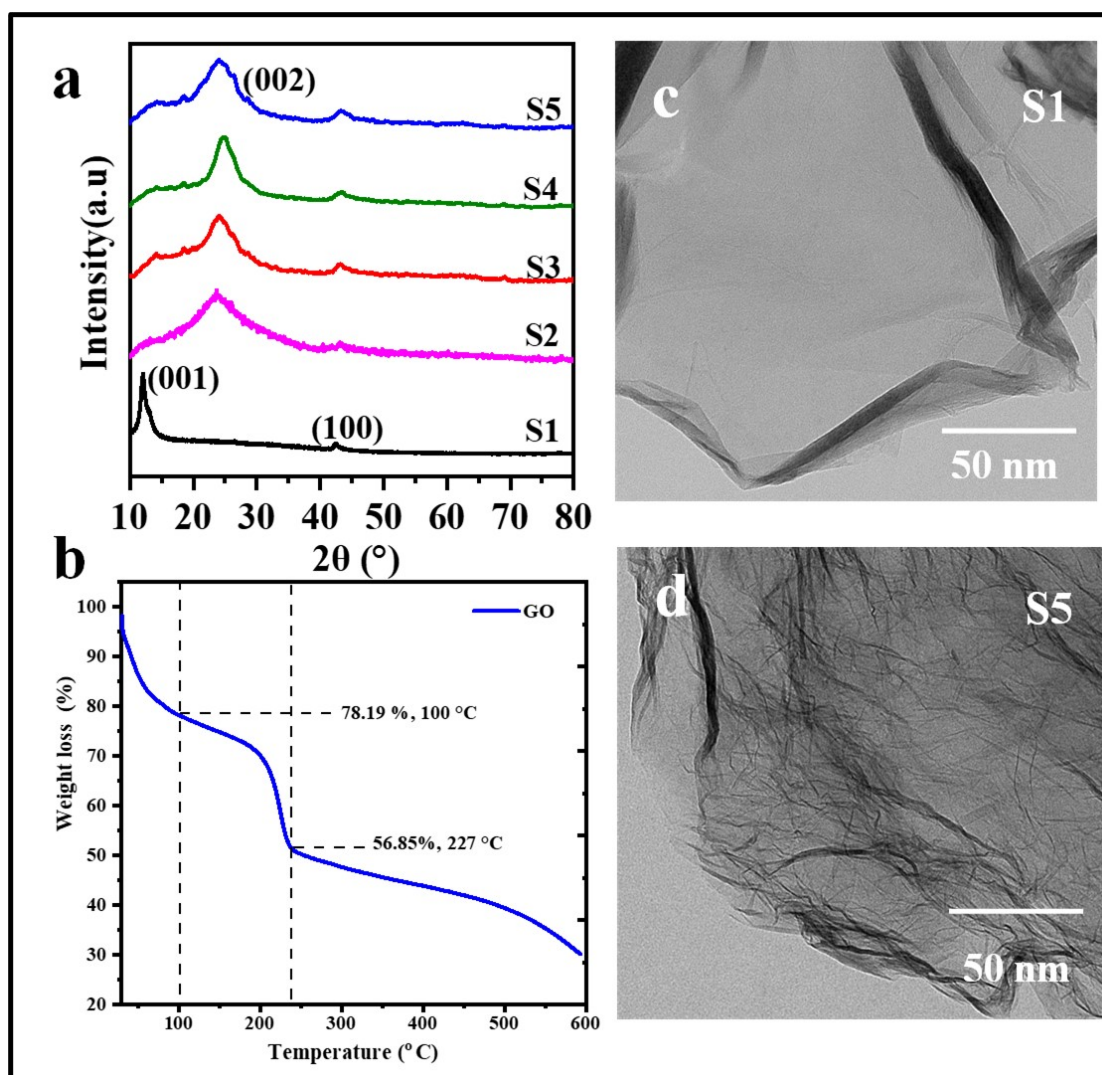


Fig. 4.1: (a) The XRD pattern of GO (S1) and rGO samples at 200 °C (S2), 300 °C (S3), 400 °C (S4) and 500 °C (S5). (b) TGA curve of GO weight loss during the reduction process of GO in the temperature range of 30-600 °C in ambient conditions. (c) and (d) TEM images of GO (S1) and rGO at 500 °C (S5).

The weight loss measurement during annealing of GO with the rate of 5 °/min was done using thermogravimetric (TGA) characterization at air atmosphere. Significant changes in the TGA curve of GO were noticed in between the temperature range of 30-600 °C. The thermogravimetric curve presented in Fig 4.1 b, is observed with two major weight loss curves. The first weight loss was observed around 100 °C. The GO reduces by 21.81% of its weight at 100 °C. It is mainly contributed by the removal of adsorbed molecular water from the GO lattice. The second stage of weight loss happens at the reduction temperature around 200 °C. There observed a firm increase in the weight loss percentage from 29.90 % to 48.83 % from the reduction temperature of 200 °C to 240 °C. The maximum rate of evolution of oxygen species occurred between 200-240 °C. The pressure evolved from the gases in the temperature range above 200 °C helps in the graphitic layer exfoliation and removes oxygen functionalities from the GO surface Kaniyoor *et al.* (2011).

Above 200 °C of annealing temperature, the increase in the weight loss confirmed a thermal exfoliation of the GO sheet effect from the rapid deoxygenation of functional groups from GO surface. Up to 300 °C, the GO loses 52.34 % of weight and increases to 60.58 % at 500 °C. The weight loss under 200 °C is mainly determined by the evaporation of water molecules and then by oxygen species desorption (such as hydroxyl and epoxy) from the graphitic structure. The weight loss between 200 - 500 °C was contributed by the deoxygenation of other oxygen functionalities bonded with carbon lattice along with the C-C bond restoration Larciprete *et al.* (2011). The weight loss in the range above 500 °C is mainly associated with the sublimation of carbon skeletal structure at ambient atmospheric conditions. This weight transition can be ascribed to the dissociation of oxygenated species on the GO lattice structure.

Figure 4.1 c and d shows the TEM micrograph image of GO and rGO annealed at 500 °C. The structural morphology of GO and rGO were modified due to oxidation and reduction influenced by the thermal instability of the GO sheet, followed by the lattice distortion with the ejection of oxygen functionalities and native carbon atoms from the GO lattice. TEM micrograph shows the wrinkled morphology of the GO and rGO structures. The exfoliation of GO during oxidation and the reduction with ejection of surface functionalities induce wrinkles and edge folding on the GO morphology.

The lattice strain generated during the co-operative realignment of functional groups particularly epoxy groups initiates the wrinkles and cracks on the GO lattices. The wrinkled GO and rGO sheets can be termed as gasothermal graphene derivatives as reported by Adarsh et.al Kaniyoor *et al.* (2011).

### 4.3.2 X-ray photoelectron spectroscopy

The X-ray photoelectron spectroscopy (XPS) analysis was done to better understand the functional groups that evolve on GO during oxidation and reduction stages. It allows surface sensitive and in-depth quantification of oxidative functional groups that exist on the surface of GO and rGO.

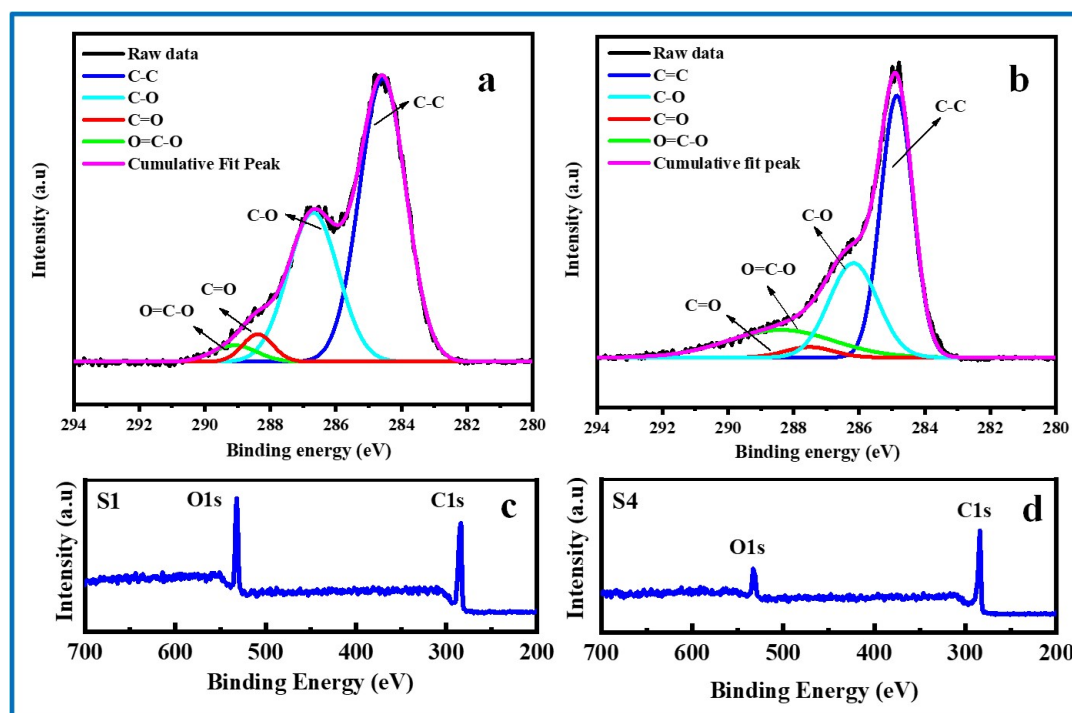


Fig. 4.2: Deconvoluted C1s XPS spectra of (a) GO (S1) and (b) rGO reduced at 400 °C (S4), (c and d) XPS survey spectrum of GO (S1) and rGO reduced at 400 °C (S4).

Figure 4.2 a and b shows the deconvoluted C1s peak of XPS spectra obtained from GO and rGO reduced at 400 °C. From the XPS survey spectra of GO and rGO reduced at 400 °C at Fig 4.2 c and d, a significant reduction in the amount of oxygen functionalities was noticed with an increment of annealing temperature. The atomic percentage and carbon and oxygen species of GO was initially less and increased after the reduction.

The variation in the peak intensity of GO and rGO signifies the elimination of carbon and oxygen related species from the rGO surface during reduction. The C1s spectra deconvoluted into four components corresponding to C-C bond ( $sp^2$ -C or  $sp^3$ -C) at a binding energy of (284-248.8 eV), C-O bond near 286 eV (hydroxyl and epoxy), C=O bond (carbonyl) at 288 eV and O=C-O (carboxyl) at 289 eV. The XPS peak of C-O, C=O and O=C-O was noticeably reduced by the increment in the annealing temperature. This signifies the elimination of oxygenated functional groups from the surface of the GO structure. The carbon-oxygen ratio (C/O) ratio was calculated from the integrated peak area calculation of the C-C peak from XPS spectra. GO structure possesses the lowest C/O ratio of 2.47 with the minimum of 71.2 % of C-C bond and 28.8 % of oxygen species ratio compared with rGO sample. The O1s peak intensity of S4 sample decreased drastically as observed from the XPS survey spectrum Fig 4.2d. The C/O ratio increased more than double the value of nearly 5.28 during the reduction than the GO. The thermal reduction improves the deoxygenation of surface functionalities with the reconstruction of the C-C bond on the rGO structure.

### 4.3.3 Raman scattering

Raman spectroscopy is a prominent and well-known technique to explore the structural transition that happened during oxidation and reduction of graphene with the inception of defects, the addition of dopants and change of hybridization. This versatile method is also used to probe the defect level and types of defects Tuinstra and Koenig (1970) Raman spectra can clearly exhibit the effect of defect type and density during the oxidation stages. However, identification of 0D and 1D defects such as point and line defects in the two-dimensional (2D) graphene oxide structure has not yet been analysed thoroughly as much as it should be. The differentiation between 0D and 1D defects of GO and GO derivatives evolved during oxidation and reduction techniques has to be disclosed to further move towards applications. The well known Raman G and D peak is observed for all the GO and rGO during oxidation and reduction stages. A change in peak position and intensity from GO to rGO transition signifies the thermally induced structural changes in the GO structure. The G band, characteristic peak of graphene-based materials corresponds to the first-order Raman  $E_{2g}$  phonon mode arising from

the in-plane vibration of the rigid graphitic layers Ferrari (2007). The defect induced D band relates to the  $A_{1g}$  breathing mode activated by the intervalley one phonon double resonance (DR) process observed from the edges of graphene based materials Casiraghi *et al.* (2009); Beams *et al.* (2011); Cançado *et al.* (2004). Besides, a distinct D' band observed as a shoulder peak near G band results from the intravalley one phonon DR scattering process between K and K' points Carozo *et al.* (2011); Ferrari and Robertson (2001). These detected D band with weak intensity and minimal dispersion arises from the crystal defects activated by the phonon scattering with smaller wave vector  $q$  Ferrari (2007).

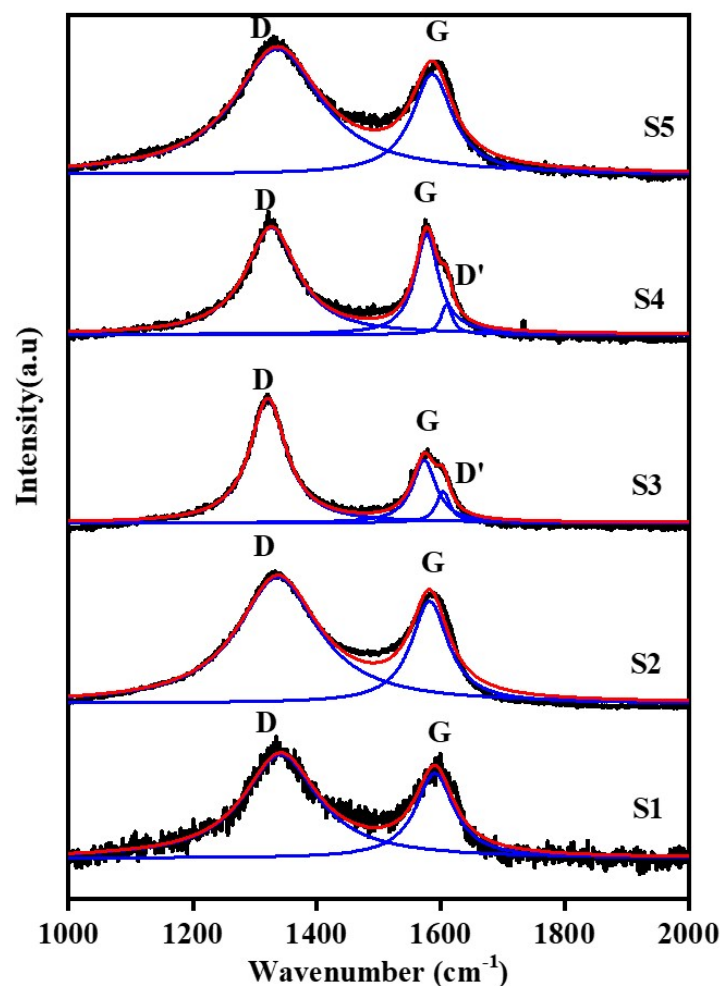


Fig. 4.3: First-order Raman spectra and fitted Raman peak of GO (S1) and rGO samples annealed at 200 °C (S2), 300 °C (S3), 400 °C (S4) and 500 °C (S5)



The recorded Raman spectra of GO and rGO at different annealing temperature is shown in Fig 4.3. For sample S1, the D and G peaks were located at  $1336\text{ cm}^{-1}$ , and  $1598\text{ cm}^{-1}$ , respectively and the band splitting was not observed in the G peak. The peak intensity ratio of D and G mode was initially low for S1 and started increasing from S2. The influence of annealing temperature on the structural changes of GO during reduction can evidently see through the fluctuations in the peak intensity of Raman spectra of all these samples. Increasing the reduction temperature reduces the G peak intensity by the formation of disordered carbon lattice. The position of G mode moved gradually towards the lower wavenumber region from the reduction temperature of  $200\text{ }^{\circ}\text{C}$ . The red shifting of the G peak position started from S1 and continued till S4. In addition to that, a significant feature is the broadening of the G peak with the formation of a new shoulder peak at the temperature of  $300\text{ }^{\circ}\text{C}$  and  $400\text{ }^{\circ}\text{C}$ . The peak splitting of the G band was observed with the formation of  $D'$  peak near  $1603\text{ cm}^{-1}$  and  $1608\text{ cm}^{-1}$  for S3 and S4. The G peak dispersion is susceptible to external perturbations such as defects, strain and doping and temperature. Thermal dilation of carbon skeletal structure stimulates the increase in phonon dispersion with the change of phonon energy dispersion centre during reduction. This might be the cause of band splitting and peak shift of G peak in Raman spectra Ferrari (2007).

Generally, the  $D'$  peak presence in Raman spectra is not much considered due to its very smaller intensity compared to the intensity of D peak Claramunt *et al.* (2015); Eckmann *et al.* (2012). However, in carbon samples with moderate defect concentration, the  $D'$  peak could visibly be seen as a tiny shoulder, and they are easily distinguished from the G peak. Besides,  $D'$  peak is not common in all the GO samples and is observed only for rGO at  $300\text{ }^{\circ}\text{C}$  and  $400\text{ }^{\circ}\text{C}$ . The formation of the  $D'$  shoulder peak made the G band of S3 and S4 to split and broad. So, the study of peak shifting and broadening of Raman G peak is always useful to analyse the impact of external perturbations on graphene based materials. It denotes the variation in defect type and concentration via structural transformation of GO during reduction at different annealing temperatures. Further, at a higher reduction temperature of  $500\text{ }^{\circ}\text{C}$ , the G peak returns to the peak position near  $1590\text{ cm}^{-1}$  which is closer to the G mode of S1. Also, at S5, the  $D'$  peak disappears and merges with the G peak with the increase of annealing temperature. It

might be attributed to the formation of highly disordered non-organized carbon atoms on the rGO lattice due to the increase in annealing temperature Sadezky *et al.* (2005); Vollebregt *et al.* (2012); Calizo *et al.* (2007).

The structural changes evolved in GO and rGO during oxo-reduction stages are visibly recognized from the changes in the Raman G and D peaks. The transition of GO to rGO encourages the structural disorder by the eviction of functional groups and native carbon atoms with the formation of vacancies and new crystalline boundaries. The above occurrence generates more zero dimensional defects or point like defects such as vacancies and one dimensional defects or line like defects such as crystalline borders or dislocations on the graphitic lattice. The comprehensive analysis of defect type and density in a highly disoriented graphitic structure such as GO and rGO is highly needed to take these materials towards applications.

To date, the contribution and the effects of point and line defects generated on the  $sp^2$  carbon lattice based graphene structures are widely studied from the thorough analysis of Raman spectroscopy Eigler *et al.* (2012); Claramunt *et al.* (2015); Eckmann *et al.* (2012); King *et al.* (2016); Lucchese *et al.* (2010). Identification of defect types like 0D or 1D in a single or few-layer graphene structure has been already investigated separately with a distinct protocol using Raman spectroscopy Lucchese *et al.* (2010); Ribeiro-Soares *et al.* (2015). Graphene based materials such as GO and rGO synthesized either physically or chemically are always accompanied by both types of defects such as 0D and 1D. Methods to identify and differentiate both type of defects in a highly defective graphitic sample has not been developed yet. So, for the qualitative analysis of 0D and 1D defects such as point like and line like defects, for the interpretation of defect type present on the highly defective GO & rGO sheets, the method have been adopted based on the technique proposed by Cançado *et al.* (2017).

The frequently used approach for the defect analysis in graphene based materials rely on the ratio of the relative intensity of Raman of D and G peaks ( $I_D/I_G$ ). Compared to graphene, GO and rGO have higher defect densities mainly evolved during the synthesis process. Considering the inconsistency of the intensity ratio relationship for defective materials such as GO and rGO, the area under the Raman peaks has been taken as an input for the defect analysis Cançado *et al.* (2017); Lucchese *et al.* (2010).

The peak area (integrated intensity) under an individual Raman peak is preferred because it reflects the probability of the phonon scattering process than the intensity ratio. GO derivatives with only line defects ( $L_a$ ) are analyzed with the equation 4.1 by assuming the sample comprises only line defects Tuinstra and Koenig (1970); Cançado *et al.* (2006). Furthermore, GO derivatives with only point defects ( $L_D$ ) is analyzed with the equation 4.2 by assuming the sample comprises only point defect Casiraghi *et al.* (2009); Lucchese *et al.* (2010).

$$\frac{A_D}{A_G} = \frac{560}{(E_L)^4} X \frac{1}{L_a} \quad (4.1)$$

$$\frac{A_D}{A_G} = \frac{4300}{(E_L)^4} X \frac{1}{(L_D)^2} \quad (4.2)$$

So, the defect analysis such as crystalline size ( $L_a$ ) and point defect density ( $1/L_D^2$ ) analysis with reference to the peak area is calculated separately by using either  $L_a$  or  $L_D$  values ervenka and Flipse (2009); Ribeiro-Soares *et al.* (2015). However, sample like GO and derivatives will have both kind of point and line defects. So, the defect analysis using Eqn. 4.1 and 4.2 is not sufficient to extract the information about the combined contribution of 0D and 1D defects in a material structure like GO and rGO with intermixed defect density. Therefore, the ( $A_D/A_G$ ) is assumed to be the contribution of three regions from the structurally damaged region (S) around the point defect ( $L_D$ ), structurally damaged region (S) around the crystalline borders or grain boundaries ( $L_a$ ) and around the defect activated region with both point and line defects. Thus, the integrated peak intensity ( $A_D/A_G$ ) incorporating both kind of defects i.e. point and line defects is given by (eqn 4.3) Cançado *et al.* (2017).

$$\left(\frac{A_D}{A_G}\right) E_L^4 = \left(\frac{A_D}{A_G}\right)_{0D}^{(s)} + \left(\frac{A_D}{A_G}\right)_{1D}^{(s)} + \left(\frac{A_D}{A_G}\right)_{0D,1D}^{(A)} \quad (4.3)$$

$$\left(\frac{A_D}{A_G}\right) E_L^4(\bar{L}_a) = \frac{1}{(\bar{L}_a)^2} \left[ 4K_s^{(1D)} l_s (\bar{L}_a - l_s) + 2K_A^{(1D)} l_e (\bar{L}_a - 2l_s) \right] \times \left( 1 - e^{-\frac{\bar{L}_a - 2l_s}{l_e}} \right) \quad (4.4)$$

$$\left(\frac{A_D}{A_G}\right) E_L^4(\bar{L}_D) = K_s^{(0D)} \left(1 - e^{-\frac{\pi r_s^2}{\bar{L}_D^2}}\right) + \frac{2\pi}{\bar{L}_D^2} K_A^{(0D)} l_e (l_e + r_s) e^{-\frac{\pi r_s^2}{\bar{L}_D^2}} \quad (4.5)$$

The equations 4.4 and 4.5 is appropriate for the samples with only line defects and samples with only points defects as exactly same as the infinite single layer graphene sheet by assuming  $L_a, L_D = \infty$  respectively Cançado *et al.* (2017). Here, the value of excitation laser energy  $E_L$  is 1.96 eV and may vary with different laser energy reported by Pimenta *et.al* Pimenta *et al.* (2007). The parameter  $r_s$  is the radius of point defect at the structurally deformed S region useful for the  $L_D$  determination. And  $l_s$  is the width of the structurally deformed line defect near the crystallite border useful for the  $L_a$  determination. The dynamical parameters  $l_{ph}$  and  $l_e$  are the phonon, and electron coherence length mainly contributes to the broadening of Raman line width in graphene. The coefficients  $K_s^{0D}, K_s^{1D}, K_A^{0D}, K_A^{1D}$  describe the Raman cross section ratios between G and D from the structurally deformed region S, around the point like region and the structurally deformed region A, near the point and line defects. The values of the structural parameters are taken as  $l_{ph} = 16$  nm,  $C_\Gamma = 87$   $cm^{-1}$  and  $\Gamma_G(\infty) = 15$   $cm^{-1}$ ,  $r_s = 2.2$  nm,  $l_e = 4.1$  nm.  $K_s^{0D} = 54$   $eV^{-4}$ ,  $K_s^{1D} = 30.4$   $eV^{-4}$ ,  $K_A^{0D} = 26.5$   $eV^{-4}$ ,  $K_A^{1D} = 30.3$   $eV^{-4}$  respectively ervenka and Flipse (2009); Beams *et al.* (2011); Cançado *et al.* (2017).

However, for the disordered samples with a combined contribution of point and line defects, the above equation 4.4 and 4.5 alone does not exclusively provide the spectral features of the disordered carbon lattice structure. The other spectral detail, such as the line width of Raman G peak ( $\Gamma_G$ ) has to be incorporated as a supporting parameter for exploring defect type and density. Accordingly, the integrated peak area  $A_D/A_G$  and the  $\Gamma_G$  are considered as important Raman spectral feature for the defect analysis of disordered graphitic structures quantitatively. The phonon localization length ( $\xi$ ) is directly related to the G peak linewidth  $\Gamma_G$  Ribeiro-Soares *et al.* (2015).

$$\Gamma_G(L_a, L_D) = \Gamma(\infty) + K_\Gamma e^{\frac{-\xi}{l_{ph}}} \quad (4.6)$$

The value of  $\Gamma_G$  increases with the decrease in  $\xi$  with respect to the phonon coherence length ( $l_{ph}$ ). For sample formed with only 1D or line defects,  $\xi$  is considered as  $\xi = L_a$ .

For sample formed with only 0D or point defects  $\xi$  is considered as  $\xi = 10 L_D$  because 0D defects are less active in phonon localization than 1D defects. And for the sample formed with the intermixed defect density such as 0D and 1D,  $\xi$  is considered as the minimum value between  $L_a$  and  $10L_D$ . The combined contribution of point and line defects is given by following equation Cançado *et al.* (2017).

Where all the parameters are same as described previously. Initially, numerical calculations were carried out with the set of data points representing the samples with only point defects and samples with only line defects, as shown in Fig 4.4 (a and b).

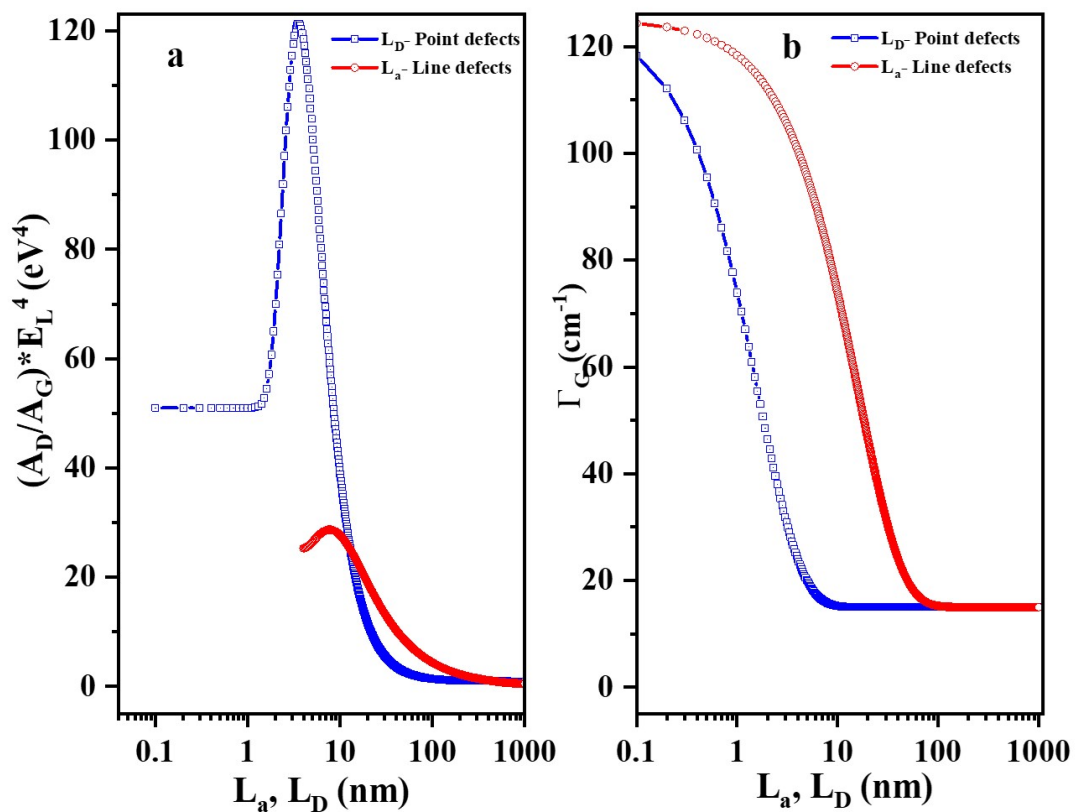


Fig. 4.4: Raman spectral behaviour of structural changes happened in graphene-based materials.  $(A_D/A_G) * E_L^4$  as a function of  $L_a$  and  $L_D$ . The blue and red lines are the plots of equations 4.4 and 4.5 as a function of  $L_a$  and  $L_D$ , respectively. (b)  $\Gamma_G$  as a function  $L_a$  and  $L_D$  using equation 4.6

The obtained  $(A_D/A_G) * E_L^4$  and G band linewidth  $\Gamma_G$  from the above simulation using equations 4.4, 4.5 and 4.6 were further applied to analyze the defective behaviour of samples with both types of defects. In all the graphs, the blue and red lines correspondingly represent the point and line defects.

$$\begin{aligned}
\left(\frac{A_D}{A_G}\right) E_L^4(L_a, L_D) = & K_s^{(0D)} \left(1 - e^{-\frac{\pi r_s^2}{L_D^2}}\right) + 4K_s^{1D} l_s \frac{L_a - l_s}{L_a^2} e^{-\frac{\pi r_s^2}{L_D^2}} \\
& + 2\pi K_A^{0D} l_e \left(\frac{l_e + r_s}{L_D^2}\right) \left(1 - 4l_s \frac{(L_a - l_s)}{L_a^2}\right) e^{-\frac{\pi r_s^2}{L_D^2}} \\
& + 2K_A^{1D} l_e \frac{L_a - 2l_s}{L_a^2} \left(1 - e^{-\frac{L_a - 2l_s}{l_e}}\right) e^{-\frac{\pi r_s^2}{L_D^2}} \quad (4.7)
\end{aligned}$$

In Fig 4.4a,  $(A_D/A_G)*E_L^4$  as a function of structural parameters  $L_a$  and  $L_D$  are plotted with the aid of equations 4.4 and 4.5. The blue line with the set of square symbols ( $L_a$  - line like defects) and red line with the set of circular symbols ( $L_a$  point like defects) are obtained by setting  $\xi = L_a$  (Where  $L_a$  value ranges from 4 to 1000 nm with 0.01 nm steps) and  $\xi = 10L_D$  (Where  $L_D$  value range from 0.01 nm to 1000 nm with 0.01 nm steps). Figure 4.4b shows the G band linewidth  $\Gamma_G$  as a function of  $L_a$  and  $L_D$  independently. It is obtained from numerical calculation of equation 4.6 with  $\xi = L_a$  and  $10\xi = L_D$ . The fitting parameter values are taken as  $l_{ph} = 16$  nm,  $C_\Gamma = 87$   $cm^{-1}$  and  $\Gamma_G(\infty) = 15$   $cm^{-1}$ , and they are the same for the line and point defects. All the blue and red lines have the same interpretation, respectively.

From Fig 4.4 a and b, it is observed that the spectral response of  $(A_D/A_G)*E_L^4$  and  $\Gamma_G$  individually varies with respect to the crystalline parameter ( $L_a$  and  $L_D$ ), which signifies the degree of disorder in a defective sample. The spectral response of integrated intensity of peak area  $(A_D/A_G)$  and G band line width  $\Gamma_G$  varied with the distinct values of  $L_a$  and  $L_D$  and touched only at the two extreme limit value of 0 and  $\infty$ . So, correlating the above  $L_a$  and  $L_D$  and  $\Gamma_G$  data points will be the most appropriate way to study and predict the defect density precisely than  $(I_D/I_G)$  analysis for a highly defective sample like GO and rGO.

Figure 4.5a shows the spectral behaviour of the graphene based nanomaterials by the change of  $(A_D/A_G)*E_L^4$  as a function of  $\Gamma_G$  obtained from equations 4.4, 4.5 and 4.6. Figure 4.5b shows the schematic illustration of point defects and line defects in rGO sheets. The scattered open symbols are the data points obtained from the experimental Raman spectra of GO and rGO samples as shown in Fig 4.5c. The experimental

values from the Raman spectra of the GO sample occupy a different position with the increase of reduction temperature. The influence of reduction temperature on the structural reconstruction of GO is apparently seen from the change of integrated peak area ratio and G band line width value at each annealing temperature. The above studies provide a deep insight into the contribution of two types of induced defects such as points and line defects in a graphitic sample with the mixed defect population through the Raman spectra analysis.

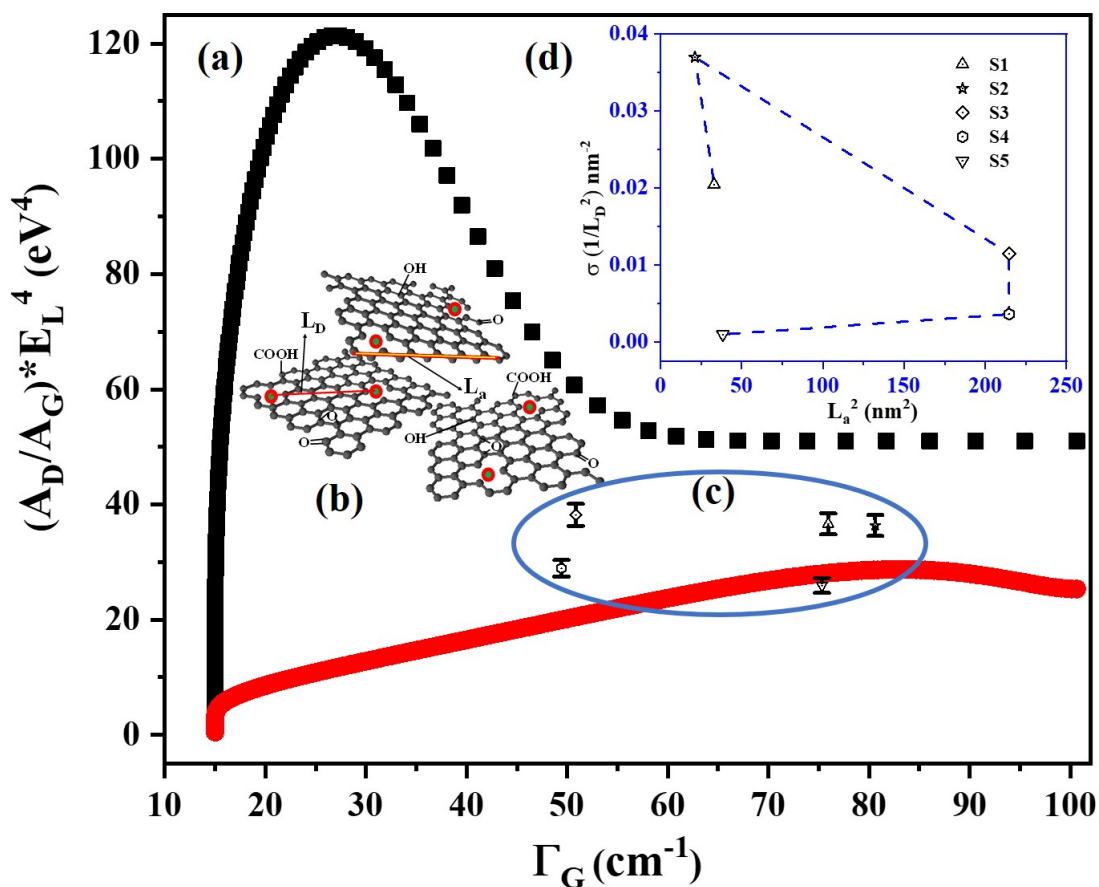


Fig. 4.5: (a) Integrated peak area  $A_D/A_G \cdot E_L^4$  as a function of G band spectral line width  $\Gamma_G$ . (b) Schematic illustration of point defects and line defects in rGO sheets. (c) The scattered open symbols are data points obtained from experimental Raman spectra of GO (S1) and rGO samples at 200 °C (S2), 300 °C (S3), 400 °C (S4) and 500 °C (S5). (d) The inset graph shows the crystallite area ( $L_a^2$ ) Vs Defect density ( $\sigma$ ) in terms of  $1/L_D^2$  of GO (S1) and rGO samples at 200 °C (S2), 300 °C (S3), 400 °C (S4) and 500 °C (S5).

As shown in Fig 4.5c, sample S1 falls in the region between the line and point defect density zone. It might be due to the formation of new crystallite boundaries during

chemical and ultrasonic exfoliation during the early stage of oxidation. Chemical and ultrasonic exfoliation of GO sheet changes the crystalline size without forming many wrinkles on the basal plane. It promotes the formation of line like defects and more edge effects with the aid of crystalline dislocations and new crystalline borders on the S1 sample. This was also observed earlier by the increased peak width (FWHM) of (001) peak of S1 with the help of XRD analysis. However, the existence of surface functionalities (oxygenated groups) in GO as a form of point defects dominated as the newly formed 0D defects during oxidation.

During the initial stage of reduction, the migration of oxygen species such as hydroxyl and epoxy on the GO basal plane induces functional group pairing and leaves the surface without much damage to the GO lattice. For S2, the thermal reduction is accompanied by the expulsion residual water molecules and a very less removal of other functionalities such as hydroxyl, epoxy groups Sinclair and Coveney (2019); Mao *et al.* (2012) due to partial reduction. So, the S2 sample at a lower reduction temperature of 200 °C occupies with the dominance of line and points defects. By the increment of annealing temperature, consumption of carbon lattice occurs through the gasification of GO as  $CO$  and  $CO_2$  while native carbon atoms react with the oxygen species. It causes the ejection of the carbon atom from the graphene lattice and creates vacancy. This is one of the causes of point defect formation in the graphene lattice.

The S3 and S4 samples lies on the regime between the density of point and the line defect zone. With respect to the G peak line width ( $\Gamma_G$ ), the S3 and S4 samples at 300 °C and 400 °C possesses smaller G band linewidth ( $\Gamma_G$ ) value and higher ( $A_D/A_G$ ) in comparison with other oxidized (S1) and reduced samples (S2 and S5). Also, the G peak position in S3 and S4 redshifts near  $1580\text{ cm}^{-1}$ . This signifies that the GO is trying to reconstruct the carbon lattice through the recovery of non-oxygenated  $sp^2$  carbon bonds. Since the reduction has been performed in ambient atmospheric conditions, the structural modification happened with the evolution of intermixed defects formed during the expulsion of carbon atoms creates point like defects and the conjugation of C-C bonds with the formation of new  $sp^2$  crystallites leads to line like defects simultaneously. The above behaviour is also noticed from the TGA analysis with maximum mass loss and XPS analysis with the highest C/O ratio above 200 °C.



In this analysis, the maximum change in  $(A_D/A_G)$  and  $(\Gamma_G)$  is observed for the sample S5. At S5, with the higher reduction temperature, the defect density increases with the decrease of phonon coherence length ( $l_{ph}$ ) due to that the precise geometrical information about the single defect might be doubtful. Since the G band line width is sensitive towards the phonon localization length ( $\Gamma$ ) with respect to the phonon coherence length ( $l_{ph}$ ) as shown in equation 4.6,  $\Gamma_G$  increases with the increase of defect density. So, sample S5 shows more deviation in  $\Gamma_G$  and  $(A_D/A_G)*E_L^4$  values than other GO samples. Also, sample S5 is lying in the regime where the line defects are maximum. It was also observed from the experimental Raman spectra in Fig 4.3 with the merging of G and  $D'$  peaks and broadening of G peak by the increment of defect concentration.

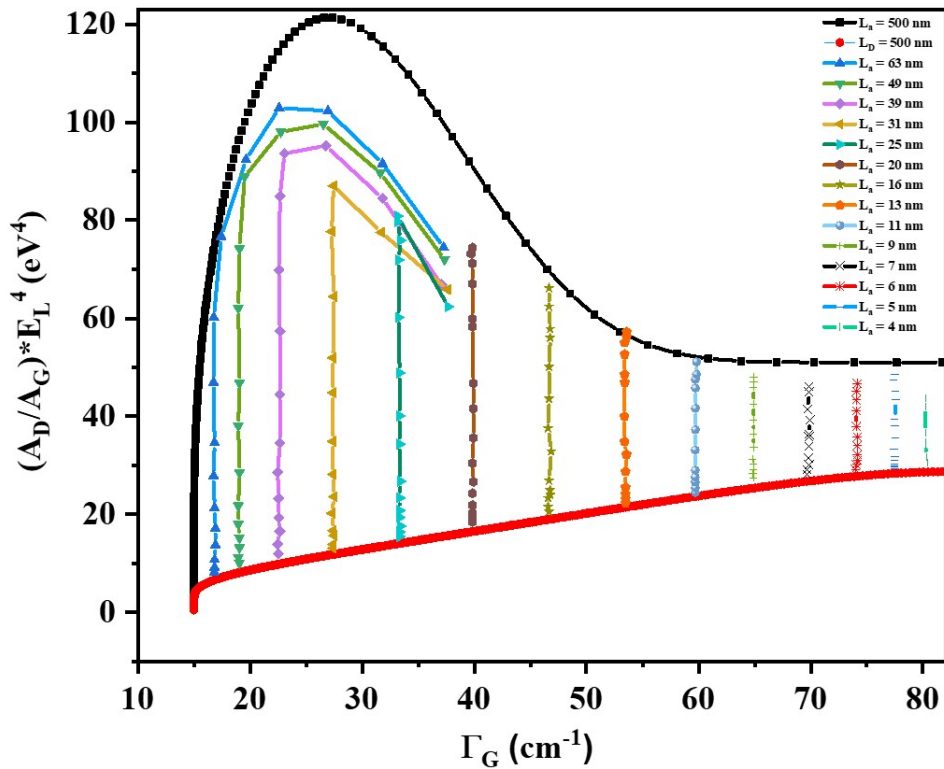


Fig. 4.6: Theoretical integrated Raman peak intensity  $(A_D/A_G)*E_L^4$  as a function of G peak line width  $\Gamma_G$  for different values of  $L_a$ . The line connected by the symbols with different colour and shapes are obtained by numerical calculations by changing the  $L_a$  value shown in the legend using the equation 4.7.

These results are widely supportive of the qualitative analysis of deformed graphitic structures with intermixed types of defects. Figure 4.5d shows the structural evolution

of GO with the change of defect density in terms of crystallite area ( $L_a^2$ ) and defect density  $1/L_D^2$  ( $= 1/L_D^2$ ). The Theoretical Raman integrated peak intensity  $(A_D/A_G)*E_L^4$  as a function of  $\Gamma_G$  for different values of  $L_a$  and  $L_D$  is shown in Fig 4.6 and 4.7, drawn using eqn 4.7. The  $L_a$  and  $L_D$  of samples S1 to S5 are extracted with the aid of Fig. 4.6 and 4.7 respectively.

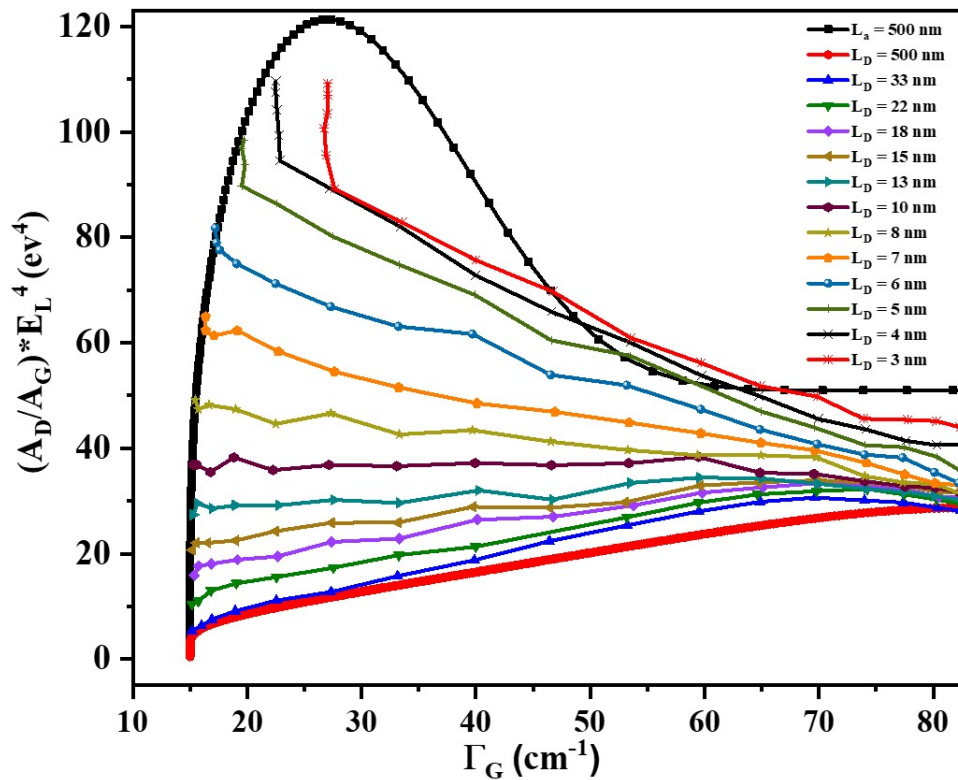


Fig. 4.7: Theoretical integrated Raman peak intensity  $(A_D/A_G)*E_L^4$  as a function of G peak line width ( $\Gamma_G$ ) for different values of  $L_D$ . The line connected by the symbols with different colour and shapes are obtained by numerical calculations by changing the  $L_D$  value shown in the legend using equation 4.7

The change in defect density during the oxidation and reduction of GO is better analysed by deconvoluting the specifications of Fig. 4.6 and Fig.4.7 obtained using equation 4.7 Cançado *et al.* (2017).

Also, the  $L_a$  and  $L_D$  of samples S1 to S5 are extracted with the aid of Figs 4.6 and 4.7. are tabulated in table 4.1. **The error in the calculated values of defect densities is less than 2%.** Among all, S2 sample shows maximum point defect density with smaller crystallite size area exhibits the dominance of 0D and 1D defect density in the sample with disordered carbon lattice. The crystallite area ( $L_a^2$ ) is more for S1 than S2 with

Table 4.1:  $L_a$  and  $L_D$  values calculated using eqn 4.7 as extracted with the aid of Figs. 4.6 and 4.7 for in samples S1 to S5

Samples	$L_a$ (nm) Calculated using Eqn. (7)	$L_D$ (nm) Calculated using Eqn. (7)
S1	5.8	7
S2	4.6	5.2
S3	14.7	9.4
S4	14.7	16.8
S5	6.2	32.5

the lesser point defect density ( $\sigma$ ). With reference to the crystallite size area and point defect density, the S3 and S4 samples shows a moderate level of 0D and 1D defect with larger crystallite size area ( $L_a^2$ ) and lesser point density ( $\sigma$ ) compared to S1, S2 and S5. The reduction in point defect density might be attributed to the eviction of oxygenated functional groups followed by the reconstructed  $sp^2$  carbon lattice with an increment of reduction temperature. At the higher annealing temperature of 500 °C, the sample is moved towards the highly disordered region with a smaller crystallite area and lesser point defect density.

## 4.4 Conclusions

In summary, the GO was synthesized by the modified Hummers method and subsequently it was thermally reduced at different temperatures to get rGO. The Structural and morphological characterizations by TEM, XRD and X-ray photoelectron spectroscopy confirms the synthesis of GO and rGO. Reduction temperature plays the most crucial role as it controls the quality of rGO in terms of weight percentage of carbon and lattice defect. The structural modification happened with the evolution of intermixed defects formed during the expulsion of carbon atoms creates point like defects and the conjugation of C-C bonds with the formation of new  $sp^2$  crystallites leads to line like defects simultaneously. The contribution of point and line defects on the structural reorientation of GO during oxidation and reduction was well understood by com-

binning the theoretical and experimental analysis of first order Raman scattering. The integrated Raman peak area ( $A_D/A_G$ ) and G band spectral line width ( $\Gamma_G$ ) calculated experimentally was mapped in numerically calculated defect diagram to calculate the defect density. It is found that rGO sample reduced at 400 °C has larger crystallite area ( $L_a^2$ ) of about 216 nm<sup>2</sup> and point defect density of  $\sigma = 0.00356 /nm^2$ . This shows that reduction temperature at 400 °C is optimum temperature under given conditions to synthesize good quality rGO sheets. Furthermore, the as-obtained GO and rGO will be widely useful for various applications such as an electrode, transistors, storage devices and sensor due to the availability of larger binding sites.

# CHAPTER 5

## **rGO-NiO nanocomposite: synthesis and electrochemical properties**

### **5.1 Introduction**

The graphene derivatives are expected to be an advantageous material in the research zone of energy storage, sustainable and renewable energy to meet the future energy requirements due to their exceptional material characteristics. Efficient, easy to fabricate, ecofriendly and lowcost devices like battery and supercapacitors are much needed resources for the storage of energy. The evitable demand on energy storage systems such as supercapacitor with higher power density and longer cycle stability than the battery increases due to the requirement of advanced technologies such as portable electronic devices, back up power sources, hybrid electric vehicles, flash cameras and so on. Nanostructured materials of higher surface area, better porosity revamps the supercapacitor performance by improving the conductivity and charge storage capacity. The type of nanostructured electrode material plays a significant role in the determination of supercapacitor performance. Many carbon based nanostructures, transition metal oxides and polymers are extensively used as an electrode material for energy storage application due to their unique physicochemical and electrocatalytic characteristics.

The charge storage mechanism of supercapacitor based on the faradic and non-faradic energy storage are named as electrical double layer (EDLC) capacitor and pseudo capacitor behaviour Li *et al.* (2016). Supercapacitor electrodes made of graphitic structures usually shows electrical double layer capacitance (EDLC) behaviour widely relying on the porosity, dielectric nature, charge transport behaviour and type of electrolyte. The charge discharge process of EDLC capacitors generated at the interfaces of electrode-electrolyte without any faradic process and the specific capacitance developed by the adsorption of ion from the electrolyte through electrostatic forces. In pseudo

capacitor the capacitance is developed by faradic redox reaction by oxidation and reduction at the electrode and electrolyte surfaces or near surfaces Yi *et al.* (2020). The ideal choice of material for EDLC super capacitors are carbon based structures and pseudo capacitors are transition metal oxides and polymers. High performance supercapacitors are possible with metal oxide electrodes than conducting polymer due to their higher theoretical capacitance value and broader choice of metal oxides structures. In general, polymer electrode based pseudo capacitor are used to suffer by lower cyclability due to their significant volume change after certain cycles. The electrodes made of transition metal oxides such as  $MnO_2$ ,  $RuO_2$ ,  $Co_3O_4$ ,  $Fe_3O_4$  and  $SnO_2$  are highly preferred in pseudo capacitors due to their easy synthesis, low cost, high energy density, longer cyclability and multivalent oxidation states with wider potential window Govindarajan *et al.* (2019) Asen *et al.* (2019). In addition to the good electrochemical characteristics like high specific capacitance ( $C_s$ ) of  $2000\text{ Fg}^{-1}$  for  $RuO_2$  and  $3560\text{ Fg}^{-1}$  for  $Co_3O_4$  the inherited property like higher toxicity makes these material less suitable as electrode materials for supercapacitors Dao *et al.* (2019). The SC electrodes made of  $Fe_3O_4$  and  $MnO_2$  are eco friendly and less cost but possesses less  $C_s$  of  $2299\text{ Fg}^{-1}$  and  $1370\text{ Fg}^{-1}$ .

Recently, the nickel oxide (NiO) nanostructures of different dimension like 1D, 2D and 3D has attracted more attention than  $MnO_2$ ,  $RuO_2$ ,  $Co_3O_4$ ,  $Fe_3O_4$  and  $SnO_2$  as electrode material due to their high theoretical capacitance value ( $2584\text{ Fg}^{-1}$ ) non-toxicity, low cost and abundance in nature Ramu *et al.* (2021). The pseudo capacitor behaviour with the faradic redox process at the surface of metal oxide electrodes mainly relies on surface area, micro structure and conductivity Daneshvar *et al.* (2018). Despite having good electrochemical characteristics and non-toxicity, the electrochemical performance of NiO usually ruins due to low conductivity, finite surface area and less active sites. The lesser conductivity NiO like metal oxides can be overcome by hybridization with conductive carbon structures Zhang *et al.* (2016c) Li *et al.* (2017a).

Carbon based structures such as activated carbon, carbon nanotubes and graphene derivatives as SC electrode materials are known for the improved electrocatalytic performance in different types of electrolytes. Among those graphene derivatives, GO and rGO are of great interest as an electrode material due to the improved porosity,

higher surface area and enhanced charge transport, and higher electrochemical stability. Rakesh Kumar *et al.* (2021) reported a microwave assisted synthesis of rGO/NiO nanocomposite with the  $C_s$  of  $270 \text{ Fg}^{-1}$  at a scan rate of  $1 \text{ Ag}^{-1}$ . Sethi *et al.* (2021) et.al reported a simple solvothermal synthesis of PGNO/NiO nanocomposite with the  $C_s$  of  $511 \text{ Fg}^{-1}$  at a scan rate of  $5 \text{ mV}^{-1}$ . Li *et al.* (2021) reported the hydrothermal synthesis of Ni-metal oxide framework (MOF) decorated NiO nanostructure at different calcination temperature. The modified electrode showed a enhanced electrochemical performance of  $435.25 \text{ Fg}^{-1}$  at  $1 \text{ Ag}^{-1}$  even at a lowest level of process temperature. Gui *et al.* (2017) reported the NiO nanocrystals anchored rGO sheets with the two step thermal annealing process with the  $C_s$  of  $422 \text{ Fg}^{-1}$  at  $1 \text{ Ag}^{-1}$ . Zhou *et al.* (2020) reported the coordinating etching and template assisted synthesis of three dimensional porous graphene/nickel cobaltoxide with the enhanced  $C_s$  of  $708 \text{ Fg}^{-1}$  at  $1 \text{ Ag}^{-1}$ . Owing to their higher surface area and interconnected porous network, the incorporation GO derivatives with metal oxide nanostructures favourable in the enhancement of electrical conductivity and pseudo capacitive charge storage behaviour of supercapacitor electrodes.

In that regard, nanocomposite of three dimensionally interconnected porous and conductive rGO/NiO based electrode material is synthesized to enhance the specific surface area and conductivity. The enhanced electrochemical performance with higher specific capacitance is mainly attributed to the improved porous structure and increased surface area of the rGO/NiO composite. The assembly of three dimensional porous rGO network and flakes like NiO nanostructure promotes the accessibility of electrolyte ions and improves the charge transport (both electrons and ions) inside the electrode. The as prepared rGO/NiO composite nanostructure improves the performance of the electrode with enhanced specific capacitance.

## 5.2 Synthesis of rGO/NiO nanocomposite

In this experiment, the rGO/NiO nanocomposites of three different ratio of rGO was synthesized by one step and simple wet impregnation process. Briefly, for the synthesis of NiO nanoflake structure, 30 ml of 35 mM nickel acetate tetrahydrate was dissolved

in deionized(DI) water and kept under vigorous stirring for 15 mins. 10 ml of 600mM urea and 20 ml 100 mM of hexamethyl tetraamine (HMT) are added to the above solution consequently and stirred for 30 mins . Then the above solution mixture was poured in a 100ml tightly closed scott duran glass bottle and kept in hot air oven at 100 °C for 24 h. The obtained solution was centrifuged at 6000 rpm and washed several time with ethanol and water. The precipitate was dried at 100 °C. Finally, the synthesized sample was calcined at 400 °C in a muffle furnace for 2 h. GO was synthesized by the modified Hummer's method. The obtained GO powder was annealed at 400 °C to obtain the rGO. For the synthesis of rGO/NiO nanocomposite, rGO of different weight percentage with 5, 10 and 20% was taken and added to the as prepared NiO nanoflakes structure. The above proportion of rGO was mixed with 25 ml of DI water and ultrasonicated for 30 min separately. The prepared NiO nanoflakes were added to the rGO mixture and stirred for 3 hours. The final product was centrifuged and dried at 80 °C in hot air oven. Hereafter, the rGO/NiO nanocomposites of 5, 10 and 20% of rGO on NiO are named as GN1, GN2 and GN3. The simple wet impregnate method of rGO/NiO nanocomposite is a viable technique for the one pot synthesis of nanocomposite without using elaborate techniques. The as synthesized interconnect network structure of rGO/NiO nanocomposite were used as the modified electrode material for electrochemical analysis.

### **5.3 Preparation of rGO/NiO modified electrode**

The rGO/NiO working electrode was fabricated as follows: To coat the active material on the Ni foam the following steps are used. The required materials for the electrode preparation are active material, activated carbon, polyvinylidene difluoride (PVDF), and N-Methyl-2-pyrrolidone (NMP). The emulsion paste with weight percentage of 80% rGO/NiO nanocomposite active material, 15% acetylene black and 5% PVDF was made deposited on the Ni foam electrode which acts as current collector. The rGO/NiO nanocomposite modified electrode of 1cm<sup>2</sup> will serve as the working electrode. The mass loading of each rGO/NiO working electrode with different percentage of 5, 10 and 20 % rGO is about 3mg.



## 5.4 Result and Discussion

### 5.4.1 X-ray diffraction analysis

The XRD patterns of NiO and rGO/NiO nanoflake structure are shown in Fig 5.1. The characteristic diffraction peak of NiO at (111), (200), (220), (222) and (311) planes is well observed for all the NiO and rGO/NiO nanocomposite structure. The sharp diffracted peaks of NiO nanoflake structure signifies the well ordered formation of NiO crystalline structure. In addition to the NiO peaks, the peak at  $2\theta = 25^\circ$  from (002) plane for the graphitic structure is observed for all the GN1, GN2 and GN3 nanocomposite. There observed a negligible changes in the NiO peaks of rGO/NiO nanocomposites after the incorporation of rGO. This confirms that the rGO/NiO nanocomposites are formed without altering the crystal structure of NiO.

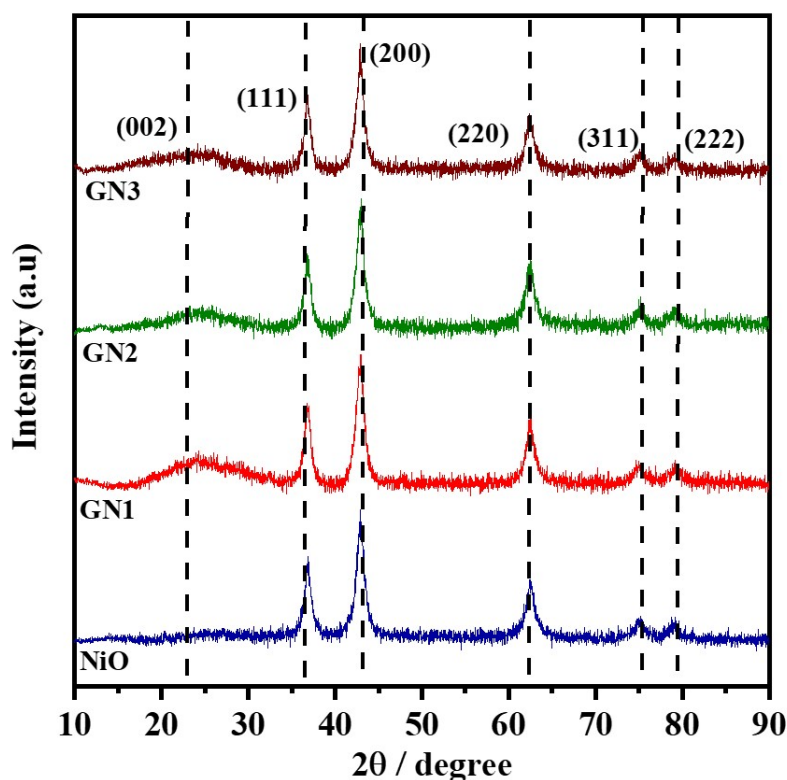


Fig. 5.1: The XRD patterns of NiO nanoflakes and rGO/NiO nanocomposites GN1,GN2 and GN3 at different proportion of rGO samples

## 5.4.2 Scanning electron microscopy

The SEM images shown in Fig 5.2 showed the the changes in the morphology of the bare NiO and rGO/NiO nanocomposite. It is visible that the surface of the NiO structure was modified by the incorporation rGO structure. The flaky NiO nanostructure is topped by the rGO sheets there by supports the conductivity and electrochemical activity of the electrode. The NiO nanoflakes are densely wrapped by many rGO sheets.

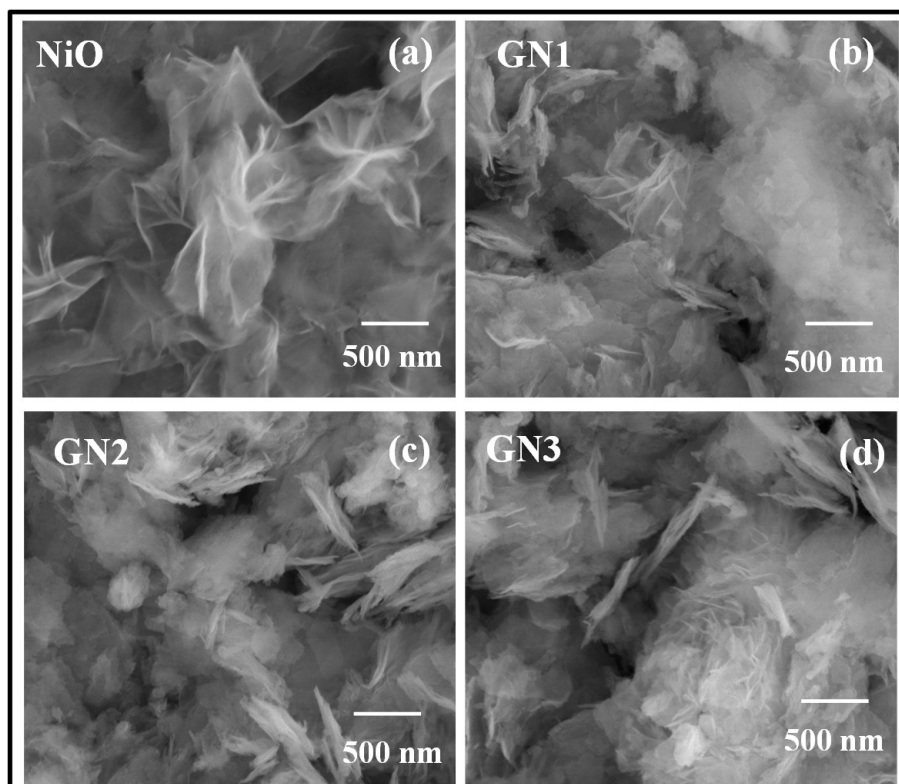


Fig. 5.2: (a) The SEM image of NiO nanoflakes structure (b,c and d) rGO/NiO nanocomposites GN1,GN2 and GN3 at different proposition of rGO samples.

The thin nanoflakes of NiO are interconnected with the nearby flakes as well with the rGO sheets to form three dimensionally interconnected network of rGO/NiO with porous structure. The elemental mapping images on Fig 5.3 shows the even distribution of nickel, carbon, and oxygen on the rGO/NiO nanocomposites with three different composition.

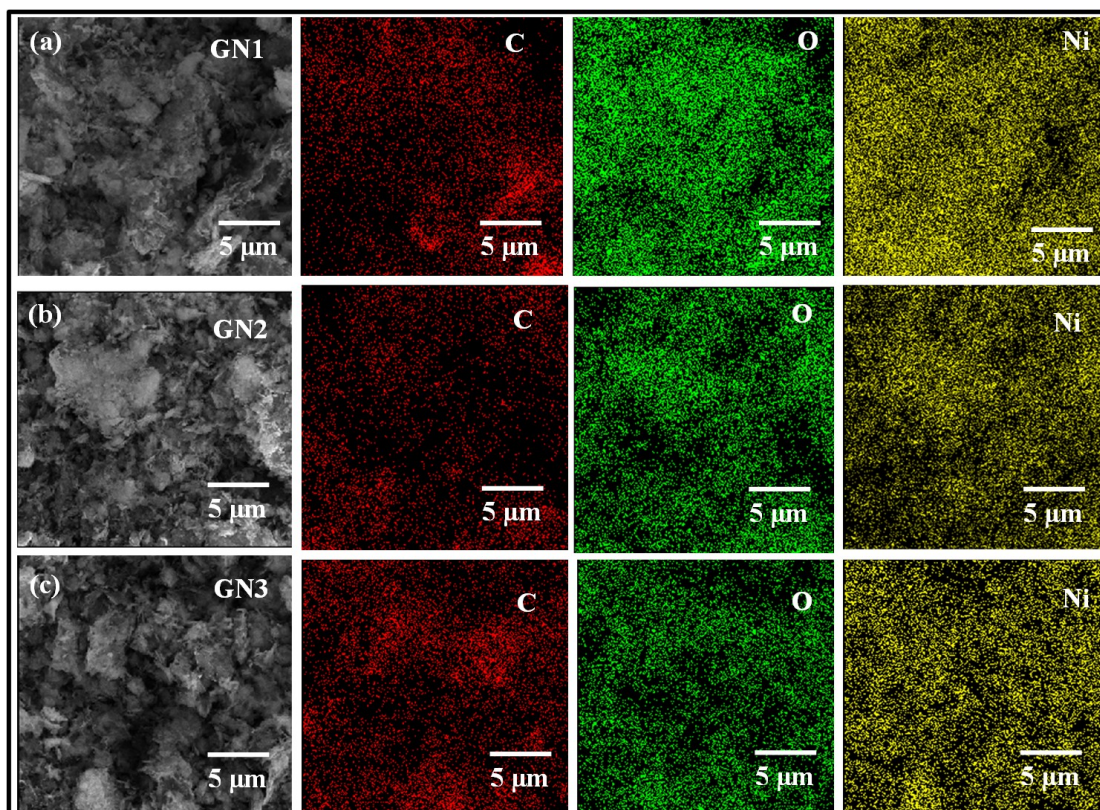


Fig. 5.3: (a,b and c) EDS elemental mapping of GN1,GN2 and GN3 at different proportion of rGO samples.C-carbon element, O-Oxygen element and Ni-Nickel element

### 5.4.3 Brunauer-Emmett-Teller analysis

To understand the change in surface area with the incorporation of rGO on NiO structure Brunauer-Emmett-Teller (BET) analysis was carried out. The nitrogen ( $N_2$ ) adsorption/desorption isotherms shows the type IV curve Xu *et al.* (2016, 2020). The steep variation of ( $N_2$ ) adsorption isotherm at lower relative pressure region signifies the development of near microporous nature on the rGO/NiO composites Sylla *et al.* (2019). The surface area of rGO/NiO nanocomposite structure increases when compared with the bare NiO sample. The pore volume and pore size distribution are obtained using Barrett-Joyner-Halenda (BJH) analysis. The specific surface area of bare NiO nanoflakes are calculated as  $85.299 \text{ m}^2/\text{g}$ . For the rGO, the calculated specific surface area was  $423.970 \text{ m}^2/\text{g}$ .

The incorporation of rGO with the NiO significantly increases the surface upto three orders. The observed specific surface area for GN1,GN2 and GN3 are 649.016, 836.653 and 1158.206  $m^2/g$ . The pore volume of rGO with 13.198  $cm^3/g$  drastically reduced due to the incorporation of NiO structure. The enhance porosity of rGO is attributed to the multiple decomposition of surface functionalities through the degassing of CO and  $CO_2$ . The observed pore volume for GN1,GN2 and GN3 nanocomposite are 1.123, 1.266 and 1.711  $cm^3$  which are absolutely higher than the pore volume of bare NiO with 0.429  $cm^3/g$ . Micropores are observed on the NiO nanoflake and rGO/NiO nanocomposite structure. For the bare rGO and NiO it is observed as 1.9 nm and 1.7 nm. The pore size is increased to 2.8, 2 and 2.4 nm with formation of nanocomposites.

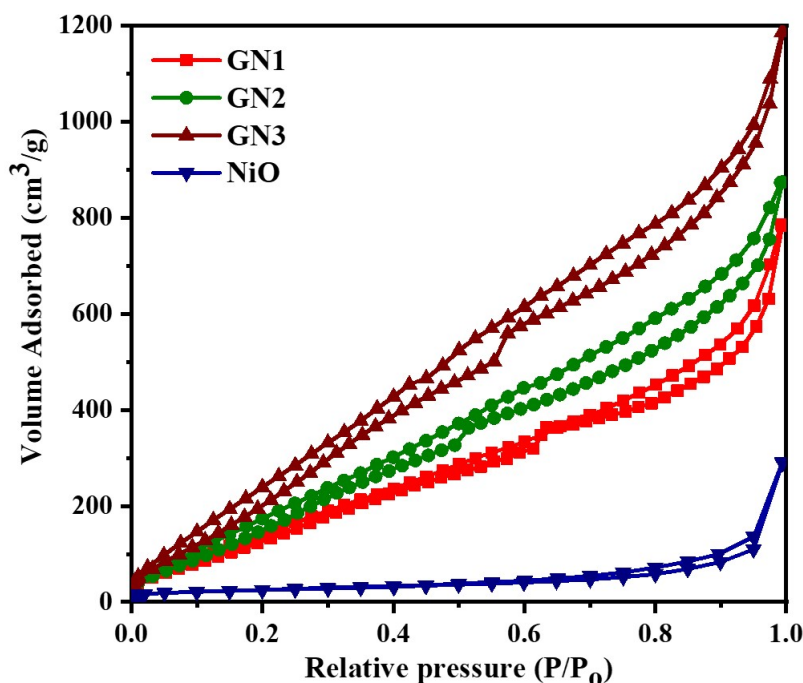


Fig. 5.4:  $N_2$  adsorption-desorption isotherms of NiO nanoflakes structure and rGO/NiO nanocomposites GN1,GN2 and GN3 with different proposition of rGO samples.

The increase in surface area, change in pore volume and size with the increment in rGO loading percentage on NiO mainly arises due to the stacking of rGO over NiO structure with adequate gap. The large specific surface area facilitates the capacitive behaviour of the electrode by improving the ion diffusion into the active sites of electrode. The above occurrence is observed with the increase of current value from the C-V curve

of rGO/NiO nanostructures. So, the hike in the surface area alone does not enhances the capacitive behaviour of the electrode in either way it aids the afore mentioned property.

#### 5.4.4 Electrochemical analysis

The electrochemical performance of as synthesized rGO/NiO electrode was analyzed using cyclic voltammetry (C-V) workstation. The C-V measurements are taken with three electrode measurement setup at the potential window of 0 to 0.5 V. The electrochemical experiment was carried out with 1M of KOH aqueous electrolyte solution.

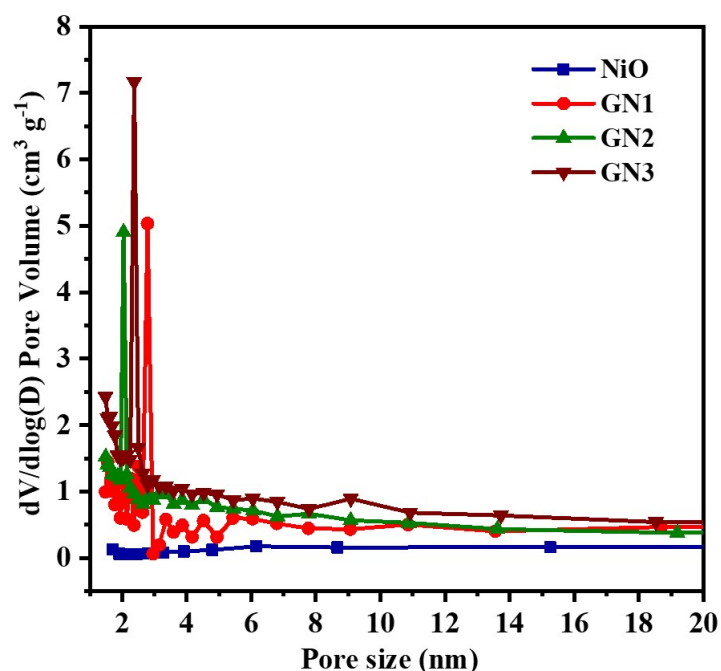


Fig. 5.5: Pore size distributions analysis using BJH data of NiO nanoflakes structure and rGO/NiO nanocomposites GN1,GN2 and GN3 with different proposition of rGO samples.

The Ag/AgCl and platinum wire electrodes are used as reference and counter electrode through out the experiment respectively. The active material loaded on the Ni foam is used as the working electrode. The CV analysis of NiO and rGO/NiO nanocomposite modified working electrode was done at diffent scan rates from 10 mV/s to 100 mV/s. The electrode with bare NiO nanoflake structure showed a CV curve with the pseudo capacitance behaviour. The CV curve of NiO electrode with the pseudo capacitance behavior is ascribed to the redox process from the  $\text{Ni}^{2+}$  and  $\text{Ni}^{3+}$  oxidation states

of NiO nanoflake structure. In general, the anode peak of NiO arises due to the oxidation of NiO to NiOOH. The cathodic peak are arises due to the conversion of NiOOH to NiO. The overall redox peak of NiO electrode is dominated only by the contribution of NiO nanostructure. The faradic reaction of NiO nanoflake electrode is given eqn 5.1.

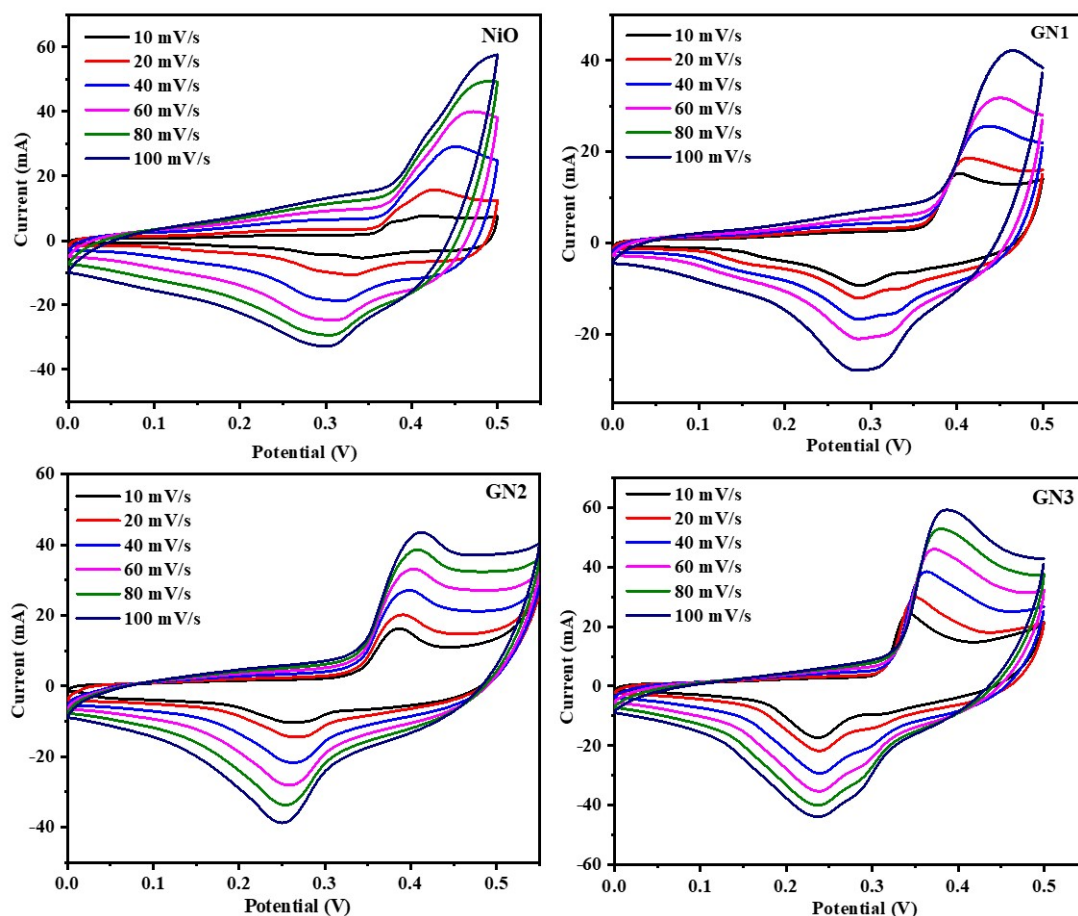
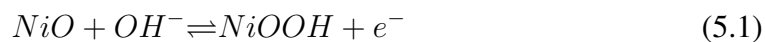


Fig. 5.6: (a) The C-V curve of NiO nanoflakes and rGO/NiO nanocomposites GN1,GN2 and GN3 at different proposition of rGO samples at different scan rates from 10 to 100 mV/s with the increment of 20 mV/s.

The CV curve of rGO/NiO nanocomposites of different proportion of rGO showed proper redox peak with existence of anodic and cathodic peaks than the bare NiO electrode in a specific operating potential range from 0 to 0.5V. The intrinsic electrical conductivity and surface active sites of NiO are tailored by the aid of rGO conducting network and improving the electrode activity. In the rGO/NiO nanocomposite, the exis-

tence of porous network of rGO might stabilizes the nickel ion oxidation states. As a result, enhanced redox activity of rGO / NiO is induced by the addition of rGO by anodic peak evolution. This shows the good electrochemical performance of rGO/NiO composite. In comparison with the current value of bare NiO nanoflakes, the current value of rGO incorporated NiO nanocomposite structure considerably increases at the lower scan rate of  $10 \text{ mVs}^{-1}$ . The increase in the CV current is observed in a sequence of NiO < 5% rGO/NiO (GN1) < 10% rGO/NiO (GN2) < 20 % rGO/NiO (GN2). Along with the increased surface area, the porous network of the rGO stimulates the charge collection and provides better charge conductivity in rGO/NiO electrodes. This suggests that, the rGO with porous interconnected network morphology favorable in enhancing the electrochemical performance of NiO nanoflakes which is important to achieve high power SC electrodes Vlad *et al.* (2016).

As shown Fig 5.6 the CV curve of lesser area for all the rGO/NiO and bare NiO at lower scan rate of  $10 \text{ mVs}^{-1}$  increases with the increase in scan rate due to ion exchange mechanism. The CV peak of bare NiO structure without rGO does not show the symmetric redox peaks with the increase of potential range. The same kind of NiO electrode behavior was reported by Nagamuthu et.al Nagamuthu and Ryu (2019). From the integrated peak area of the C-V curve, the specific capacitance of NiO and rGO/NiO nanocomposites with various scan rates are calculated using eqn 5.2 Miniach and Gryglewicz (2018) Ghosh and Srivastava (2020).

$$C_s (F/g) = \frac{\int Idv}{vm\Delta V} \quad (5.2)$$

Where,  $\int Idv$  signifies the area of the CV curve of each rGO/NiO nanocomposites and bare NiO structure. The scan rate of the CV analysis is denoted by 'v'. The mass of the active material deposited on the electrode is 'm'.  $\Delta V$  signifies the scan rate of the CV measurement. The specific capacitance of bare NiO nanoflakes, calculated at a lower scan rate of  $10 \text{ mV/s}$ , is  $170.01 \text{ F/g}$ . The value of  $C_s$  is increased by the rGO addition on NiO. For the GN1, GN2 and GN3 samples, the obtained  $C_s$  values are 262.92, 350.28 and  $417.52 \text{ F/g}$  at a minimum scan rate of  $10 \text{ mV/s}$ . The rGO/NiO nanocomposite modified electrode showed a four fold increase in capacitance value when compared

with the bare NiO structure. The change in the specific capacitance value of rGO/NiO composites and bare NiO structure at different scan rates are shown in Fig 5.8.

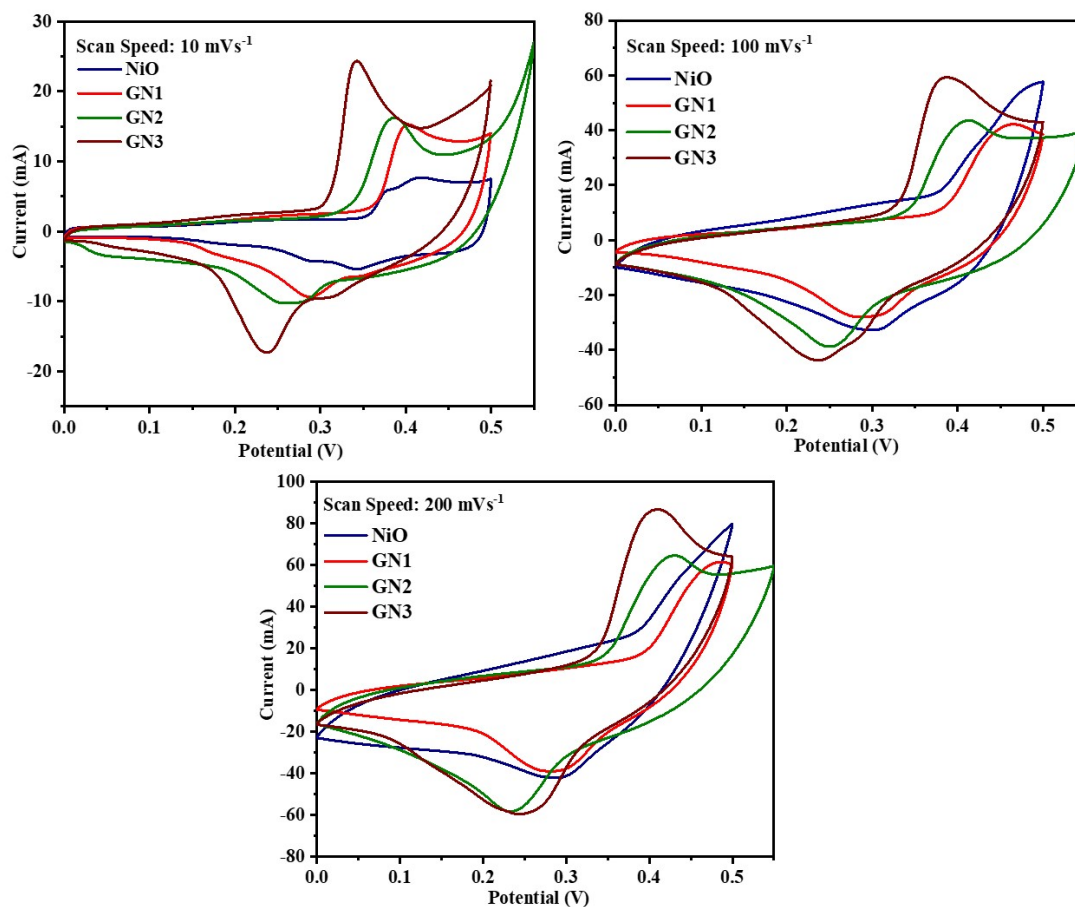


Fig. 5.7: (a) The C-V curve of NiO nanoflakes and rGO/NiO nanocomposites GN1,GN2 and GN3 at different proposition of rGO samples at the lower, higher, and highest scan rate of 10, 100 and 200 mV/s.

The effective electrochemical performance of rGO/NiO nanocomposite is apparently good at a lower scan rate of 10 mV/s than the higher and highest scan rates of 100 and 200 mV/s as shown Fig 5.7. The faradic process of rGO/NiO is very much prominent at a lower scan rate of 10 mV/s is mainly attributed by the charge diffusion process. At lower potential scan rates, the ions in the electrolyte solution have enough time duration to diffuse better in to the rGO/NiO electrode than the higher scan rates. This increases the energy storage behaviour with higher capacitance value. The C-V analysis at higher scan rates urges the ionic transport to finish faster which reduces the electrochemical performance with the reduction in capacitance value. So, the electrochemical performance decreased with the increase in scan rate for all the bare NiO and



rGO/NiO composites. This is accomplished with ion diffusion limitations and increase in ohmic loss of the electrode. The specific capacitance values of distinct rGO and rGO/Metal oxides based electrodes as an efficient electrode material in supercapacitor are shown in table 5.1.

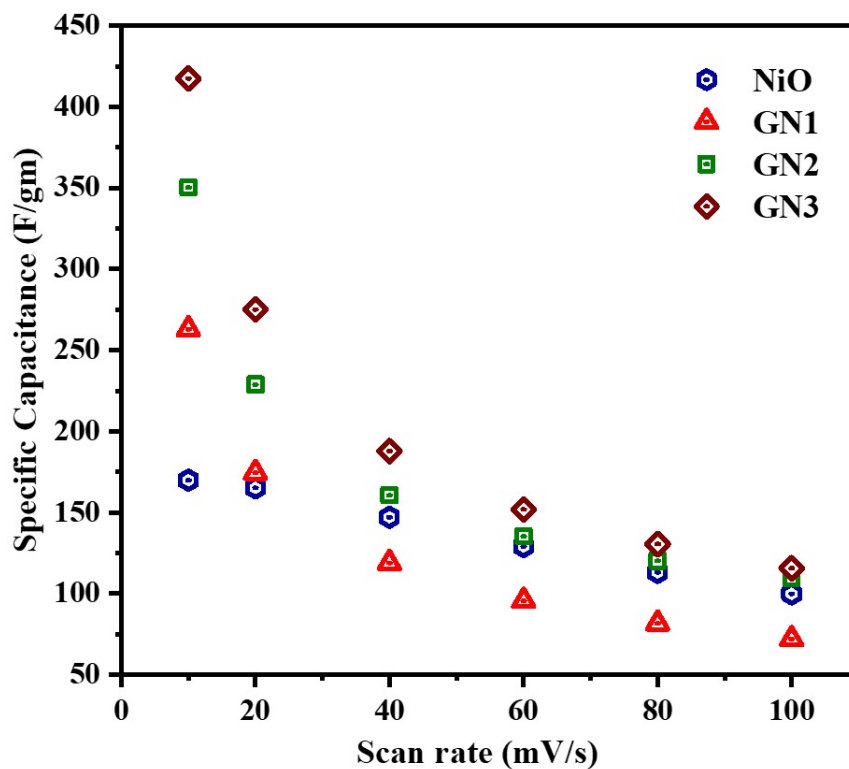


Fig. 5.8: The variation in specific capacitance value at the different scan rates of 10, 20, 40, 60, 80 and 100 mV/sec for NiO and rGO/NiO nanocomposites (GN1, GN2 and GN3).

The electrochemical mechanism of rGO/NiO nanocomposite electrode is proposed and analyzed. Pseudocapacitive metal oxide nanostructures such as NiO have lower conductivity and higher theoretical specific capacitance. Graphene derivatives possess limited EDLC behaviour and higher conductive networks. The pseudocapacitive based charge storage behaviour in metal oxide nanostructures are mainly contributing to the electrochemical faradic process. The redox process is a unique surface dependent process or near a surface process. It mainly occurs on the top surface or a few layer inside from the outer surface of the active electrode.

Table 5.1: Comparison of specific capacitance values of rGO/Metal oxides based electrodes for efficient energy storage in supercapacitor

Supercapacitor electrode materials	Synthesis method	Type of Electrolyte	Specific capacitance	References
Porous graphene/NiO nanocomposite	Solvothermal synthesis	2M KOH	511.0 $Fg^{-1}$ at $5 mV.s^{-1}$	Sethi <i>et al.</i> (2021)
NiO/rGO composites	Hydrothermal	6M KOH	171.3 $Fg^{-1}$ at $0.5 Ag^{-1}$	Xu <i>et al.</i> (2020)
NiO/rGO Nanocomposite	Microwave irradiation method	6M KOH	395 $Fg^{-1}$ at $1 Ag^{-1}$	Rakesh Kumar <i>et al.</i> (2021)
Ag nanoparticles anchored NiO/GO	Hydrothermal	2M KOH	229 $Fg^{-1}$ at $1 Ag^{-1}$	Zhou <i>et al.</i> (2016)
Ni-MOF derived NiO/rGO composites	Hydrothermal	6M KOH	435.25 $Fg^{-1}$ at $1 Ag^{-1}$	Li <i>et al.</i> (2021)
3D-porous graphene/ $NiCo_2O_4$	Coordinating etching and /Template assisted method	1M KOH	708.36 $Fg^{-1}$ at $1 Ag^{-1}$	Zhou <i>et al.</i> (2020)
3D Z-CoO/RGO	Hydrothermal	2M KOH	275 $Fg^{-1}$ at $1 Ag^{-1}$	Zha <i>et al.</i> (2021)
Ag-rGO/ $MnO_2$ nanorods	Hydrothermal and thermal annealing	2M KOH	675 $Fg^{-1}$ at $0.5 Ag^{-1}$	Ansari <i>et al.</i> (2022)
rGO/ $MnO_2$ nanorods	Thermal annealing	2M KOH	306.25 $Fg^{-1}$ at $0.5 Ag^{-1}$	Ansari <i>et al.</i> (2022)
NiO nanocrystals /rGO Nanocomposite	liquid phase precipitation and subsequent calcination process.	2M KOH	422 $Fg^{-1}$ at $1 Ag^{-1}$	Gui <i>et al.</i> (2017)

Continuation of Table 5.1				
$C_{o_3}O_4@MnO_2/N$ -doped Graphene oxide (NGO) hybrid composite	Thermal reduction process	6M KOH	$347 Fg^{-1}$ at $0.5 Ag^{-1}$	Ramesh <i>et al.</i> (2018)
$SnO_2@NGO$ composite	Thermal reduction process	6M KOH	$378 Fg^{-1}$ at $4 Ag^{-1}$	Ramesh <i>et al.</i> (2019)
rGO/Cu-MOF@PANI composite	Hydrothermal co-assembly method	1M $H_2SO_4$	$276 Fg^{-1}$ at $0.5 Ag^{-1}$	Le <i>et al.</i> (2022)
rGO anchored CuS nanospheres	Wet reduction process	6M KOH	$235 Fg^{-1}$ at $1 Ag^{-1}$	El-Hout <i>et al.</i> (2021)
$MoS_2/CoS_2/rGO$ hybrid nanocomposite	Hydrothermal method	2M KOH	$190 mF cm^2$ at $0.5 mA cm^2$	Askari <i>et al.</i> (2020)
Ruthinium/rGO nanocomposite	Liquid plasma-assisted method	2M $H_2SO_4$	$136.7 Fg^{-1}$ at $20 mV.s^{-1}$	Dao <i>et al.</i> (2019)
rGO/NiO nanocomposite (GN1)	Thermal annealing and wet impregnation	1M KOH	$262.93 Fg^{-1}$ at $10 mV.s^{-1}$	In this work
rGO/NiO nanocomposite (GN2)	Thermal annealing and wet impregnation	1M KOH	$350.29 Fg^{-1}$ at $10 mV.s^{-1}$	In this work
rGO/NiO nanocomposite (GN3)	Thermal annealing and wet impregnation	1M KOH	$417.52 Fg^{-1}$ at $10 mV.s^{-1}$	In this work

The formation of NiO nanoflake structure at higher calcination temperature brings well ordered crystalline structure to the NiO. The increased surface area and the defective surface are the key parameters for the enhanced chemical activity of electrode materials Chen *et al.* (2016a). The as formed NiO with negligible surface defects minimizes the electrochemical performance with the smaller oxidation peak as shown in Fig

5.6. The higher crystallinity of NiO hinders the ion transport such as  $OH^-$  inside the surface layer during the redox cycle. This minimizes the electrode performance Marrani *et al.* (2014) Gui *et al.* (2017). The hybridization of graphene based materials and metal oxides will compliment each other and offer a new modified active electrodes with an improved electrochemical performance Marina *et al.* (2019) Ke and Wang (2016).

The rGO provides conductive network pathway to the NiO structure and increase the charge transport. The change in rGO percentage in the rGO/NiO nanocomposite accelerates the capacitive behaviour of the working electrode through the improved conductive network and increased surface area. So, the specific capacitance of rGO/NiO composites increased with increase in rGO percentage.

#### **5.4.5 Electrochemical impedance spectroscopy analysis**

Electrochemical impedance spectroscopy (EIS) is the analysis technique to understand the mechanism of charge transfer on the electrode-electrolyte interfaces. Nyquist plots of rGO/NiO modified electrode is shown in Fig 5.9. The frequency range was 0.1 to 100 kHz. The two main parts of Nyquist plot are the high frequency region and low frequency region. The intercept of the curve at the real axis ( $Z'$ ) shows the solution resistance ( $R_s$ ) value. The diameter of the semicircle at the middle range of the frequency shows the charge transfer resistance ( $R_{ct}$ ). The linear line at the low frequency region implies the ion diffusion (Warburg resistance) inside the electrode material.

In the Fig 5.9, very small difference is observed in the high frequency region for bare NiO and rGO/NiO electrodes. The sheet resistance ( $R_s$ ) is the combined value of intrinsic resistance of material used in the electrode, electrolytes ionic resistance and contact resistance between the counter and working electrode. The radius of the semicircle signifies the charge transfer resistance ( $R_{ct}$ ) of the electrode materials which can be controlled by the electrochemical process. The value of  $R_{ct}$  depends upon the type of electrochemical process, reaction temperature, electrolyte concentration. The Warburg resistance 'W' is known as the ion diffusion resistance. The Nyquist plot is fitted by the equivalent circuit.

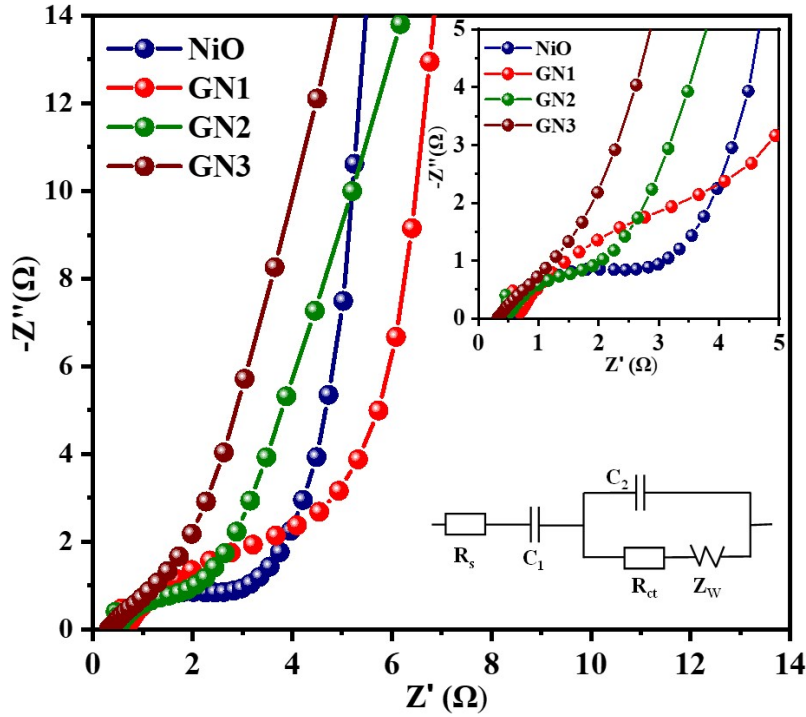


Fig. 5.9: Nyquist plot of NiO and rGO/NiO (GN1,GN2 and GN3) electrodes. (inset shows the lower frequency region of the plot)

The  $R_s$  value obtained for the bare NiO electrode is  $0.6106 \Omega$ . It reduces to  $0.7$ ,  $0.513$  and  $0.398 \Omega$  for GN1, GN2 and GN3. The obtained  $R_{ct}$  of bare NiO is more than the other modified electrodes with visible semicircle region at the middle of the frequency region. For the GN2 and GN3 electrodes, the semicircle almost disappeared. This implies the conductive nature of the electrode. The NiO electrode shows  $R_{ct}$  value of  $1.735 \Omega$  and it reduces to  $2.1$ ,  $0.9$ ,  $1.096 \Omega$  for GN1, GN2 and GN3. The slope of the straight line at lower frequency region of GN1 modified electrode with the lowest 5% concentration of rGO is lesser than the bare NiO electrode. At the mean time, the slope of the straight line at the lower frequency region is increased for GN2 and GN3 samples with increasing the rGO percentage on NiO. The Warburg (W) resistance for the bare NiO electrode was  $0.23$  (mho/sqrt(Hz)) and it reduces to  $0.12$ ,  $0.09$ ,  $0.12$  (mho/sqrt(Hz)) for GN1, GN2 and GN3. This signifies the enhanced diffusion rate of ions in the electrolyte with the smaller diffusion resistance. Also, this can be attributed by the improved porous nature of modified rGO/NiO electrode with higher surface area. So, the incorporation of GO shows a better effect on the rGO/NiO electrode in terms of enhanced electrochemical performance.

## 5.5 Conclusion

In summary, a simple thermal annealing and wet impregnation based synthesis of rGO/NiO nanocomposite with different proportion of rGO is demonstrated. The incorporation of rGO did not significantly alter the crystal structure of NiO thus facilitates the formation of rGO/NiO nanocomposite observed from the XRD peaks. The carbon, oxygen and nickel atoms are uniformly distributed in the rGO/NiO nanocomposites observed from the EDX elemental mapping. The introduction of rGO on NiO remarkably improves the redox nature of NiO nanoflakes. The improved surface area and pore volume with the increase in rGO percentage facilitates the electrochemical performance. With minimal synthesis complexity and a lesser electrolyte concentration the rGO/NiO nanocomposites shows better electrochemical performance than the bare NiO structures. The rGO/NiO modified electrodes with maximum rGO ratio of 20% (GN3) exhibits four fold increase in specific capacitance value of  $417.52 \text{ F g}^{-1}$  at  $10 \text{ mV s}^{-1}$  compared to the bare NiO electrode. This confirms the importance of rGO addition as a inexpensive and ecofriendly material for the reinforcement of NiO with better electrochemical behaviour.

# CHAPTER 6

## Synthesis of GQDs from GO and sensing application

### 6.1 Introduction

Water contamination by toxic heavy metal ions severely impacts the health of human beings and environment. In recent years, heavy metal exposure to humans and other ecosystems exponentially increases with increase in industries and domestic effluences. Heavy metals like Mercury (Hg), Lead (Pb) and Cadmium (Cd) should be controlled from food, soil, drinking water, air and ecosystem due to their excessive bioaccumulation ability and high toxicity even at lower concentration Joseph *et al.* (2019); Nolan and Lippard (2008); Zhang and Chen (2014). As per WHO guidelines value the permissible limit of mercury is 6  $\mu\text{g/L}$  (0.006 mg/L), cadmium is 3  $\mu\text{g/L}$  (0.003 mg/L) and for lead is 10  $\mu\text{g/L}$  (0.01 mg/L).

Previously prodigious numbers of analysis method were proposed by researchers for sensing heavy metals in water using complex instruments based detection method, electrochemical method, optical sensing method and electronic sensing method with filter, membranes, electrodes, Schottky diodes and field effect transistors Batista *et al.* (2007); Souza *et al.* (2015). Most of the sensing techniques were sensitive and selective towards a particular analyte. The bulky sensing mechanism such as inductively coupled plasma mass spectrometry (ICP-MS), gas chromatography and atomic absorption spectroscopy (AAS) have limitations such as complex procedure, precise sample preparation, expensive equipment and professional expertise Bings *et al.* (2006); Butler *et al.* (2006); Li *et al.* (2013). It restricts wider usage of sensor equipment for various applications. So, developing simple, low-cost and environment friendly sensing method for heavy metal ion detection is needed in the current scenario.

Fluorophore dependent PL sensing mechanism is preferred due to its simplicity and high sensitivity. It is a low cost technique with fast acquisition time Qian *et al.* (2015). Strategies based on selective fluorescence emission and fluorescence quenching is an

extraordinary tool for opto-sensing due to its sensitivity and simplicity. Functionalized or capped semiconductor quantum dots (QDs) like CdSe, CdTe, ZnS, CdS and core/shell QDs such as CdSe/ZnSe etc have been considered as an effective fluorescence probe Chen and Rosenzweig (2002); Costa-Fernández *et al.* (2006); Mahmoud (2012); Wu *et al.* (2008). These semiconducting quantum dots are inorganic nano-crystals usually from II-VI, III-V or IV-VI elements functionalized with surfactants and has a modifiable bandgap Frasco and Chaniotakis (2009). Interaction of surface functional groups with the surrounding analyte molecule is responsible for the luminescence behavior of quantum dots which makes them an efficient sensing material Lou *et al.* (2014).

Duan *et al.* have explained the PL quenching of N-acetyl-L-cysteine (NAC)-capped ZnS QDs in water for sensing  $Hg^{2+}$  ions. The mechanism is effective energy transfer between QDs and metal ions followed by nonradiative recombination Duan *et al.* (2011). Pooja *et al.* explored the selective and sensitive fluorescent nanosensing of COOH functionalized CdTe quantum dots for different metal ions using turn off fluorescence response in aqueous environment Chowdhury *et al.* (2021). They are far better than the conventional organic dyes which possess a low light scattering and reduced optical absorption. But some drawbacks are still existing with semiconducting quantum dots such as toxicity, insolubility, low selectivity of ions, and reduced photo physical property due to capping agents Li *et al.* (2007).

Sensors based on graphene based materials like graphene oxide (GO), reduced graphene oxide (rGO) and carbon nanotubes are being proposed for the detection of heavy metals Anh *et al.* (2017); Lalwani *et al.* (2014); Li *et al.* (2014); Sun *et al.* (2008); Ting *et al.* (2015); Wang *et al.* (2015). Recently, GQDs are used in optical sensors due to its fascinating properties such as three dimensional confinement, edge effects, biocompatibility, superior surface grafting and less toxicity Chandra *et al.* (2014); Shen *et al.* (2012); Shi *et al.* (2016); Sun *et al.* (2013a). The few layer GQDs with quasi zero dimensional structure and adjustable bandgap provides stable and strong photoluminescence Chen *et al.* (2014); Khose *et al.* (2021); Qian *et al.* (2014). Also, graphene oxide (GO) and GQDs are used for various biomedical applications due to its nontoxic and biocompatible nature. Due to their nontoxic nature, they are widely applied in tissue engineering, bone replacement, and as antimicrobial agents J *et al.* (2020); Kumawat



*et al.* (2017); Venkataprasanna *et al.* (2020). Owing to their outstanding property, GQDs have become an ideal alternative to the existing semiconductor quantum dots and organic dyes for bioimaging and biosensing Guo *et al.* (2015); Kaewprom *et al.* (2019); Lee *et al.* (2021); Li and Zhu (2013); Liu *et al.* (2020a); Tam *et al.* (2021); Zhu *et al.* (2012).

Recently, Shtepliuk *et al.* has reported the heavy metal ion interaction with GQD functional groups and vacancy-type defects in GQDs Shtepliuk *et al.* (2017). Wang *et al.* has studied GQD and N-GQD for selective and rapid sensing of metal ions by fluorescent quenching effect Wang *et al.* (2018a). Xiaowen Zhu has reported the selective detection of  $Fe^{3+}$  by PL quenching of GQDs. The induced aggregation of metal ion is mainly attributed to PL quenching Zhu *et al.* (2017). Panxing yang *et al.* has used B/N doped GQDs for sensing  $Hg^{2+}$  and  $F^{-}$  ions (Yang *et al.*, 2019). Low water solubility is the main limitation in many fluorescent sensors for sensing metal ions. So there is a need to develop effective methods for toxic heavy metal ion sensing in real samples Kaewanan *et al.* (2017). Also, to date much work is not done on GQDs compared to functionalized graphene for sensing applications and so the sensing mechanism.

In this chapter oxygenated functional groups decorated GQDs were synthesized by facile hydrothermal method that shows good water solubility. The photoluminescence (PL) property of these intrinsic and label free GQDs has been employed to devise a sensor for toxic heavy metal ions detection in water. Photoluminescence spectra was analyzed by the Stern-Volmer (S-V) equation to study the fluorescent quenching mechanism of this system. The S-V analysis suggests the static and dynamic quenching mechanism between GQDs and different metal ions during PL quenching. Furthermore, this work indicates that, the biocompatible GQDs are a viable and high potential material which could be extended as an attractive sensing unit for real time detection of heavy metals in water with good sensitivity and cost-effective protocol.

## 6.2 Experimental method

GQDs were synthesized from GO Kumar *et al.* (2015); Pan *et al.* (2010); T. *et al.* (2021); Zhang *et al.* (2014). For the oxidation of GO, 250 mg of GO was sonicated in 50 ml

of concentrated  $H_2SO_4$  and 150 ml of  $HNO_3$  (volume ratio 1:3) for 8 hr. The above solution is diluted with water. It is then rinsed with water to remove acid. The filtered product was dried and dispersed again in 50 ml DI water with 1mg/ml concentration. The pH of this dispersion was maintained at 8 by adding appropriate amount of NaOH. The solution was heated at 200 °C for 10 h in hydrothermal setup. After cooling, 0.22  $\mu$ m micro-porous membrane was used to filter the solution which contains the GQDs. Aqueous solutions of  $Hg^{2+}$ ,  $Cd^{2+}$  and  $Pb^{2+}$  in various concentrations (1 ppm, 2 ppm, 5 ppm, 10 ppm, 20 ppm, 50 ppm and 100 ppm) were freshly prepared. To evaluate the sensitivity of the GQDs solution towards  $Hg^{2+}$ ,  $Cd^{2+}$  and  $Pb^{2+}$ , the above metal ion solutions of different concentration were mixed separately with 1 mg/ml of GQD aqueous dispersion at a volume ratio of 1:1. The resultant solution was incubated for 10 min under well stirring condition at room temperature. Then, the obtained solutions were characterized by photoluminescence (PL) spectrometer (Edinburgh, model F-900) at room temperature using an excitation wavelength of 320 nm. The structural analysis was done using high-resolution transmission electron microscopy (HRTEM).

### 6.3 Result and discussion

Figure 6.1 (a) and (b) show the TEM image of GQDs. The GQDs are highly crystalline in nature. They are monodispersed, spherical in shape and dispersed uniformly without much agglomeration. The lattice fringe image of GQD is given by high resolution TEM image (Fig 1b). It matches with the characteristic lattice plane (100) of carbon graphitic structure Ganganboina *et al.* (2018). The average diameter of GQDs is approximately 50 nm. The size of GQDs is relatively uniform. From the Fig 6.1 (a), it is observed that the GQDs have curved edges. GQDs with curved edges and monodispersed nature are expected to have notable improvement in the sensing behavior. Inset of Fig 6.1 b shows the FTIR spectrum of pristine GQDs. The band at  $1047\text{ cm}^{-1}$  corresponds to the vibrations of C-O bond. The band at  $1644\text{ cm}^{-1}$  is related to the stretching vibration of C=C and C=O group. The band at  $2979\text{ cm}^{-1}$  is due to the C-H stretching vibration. The absorption peak around  $3284\text{ cm}^{-1}$  is due to the presence and bending vibration of O-H bonds from the  $H_2O$  molecules present in the GQDs. And surface functional-

ized GQDs played a vital role in heavy metal detection by either making strong/weak bond or collisional interaction with the heavy metal atom followed by rearrangement of electronic states with non radiative decay and PL quenching.

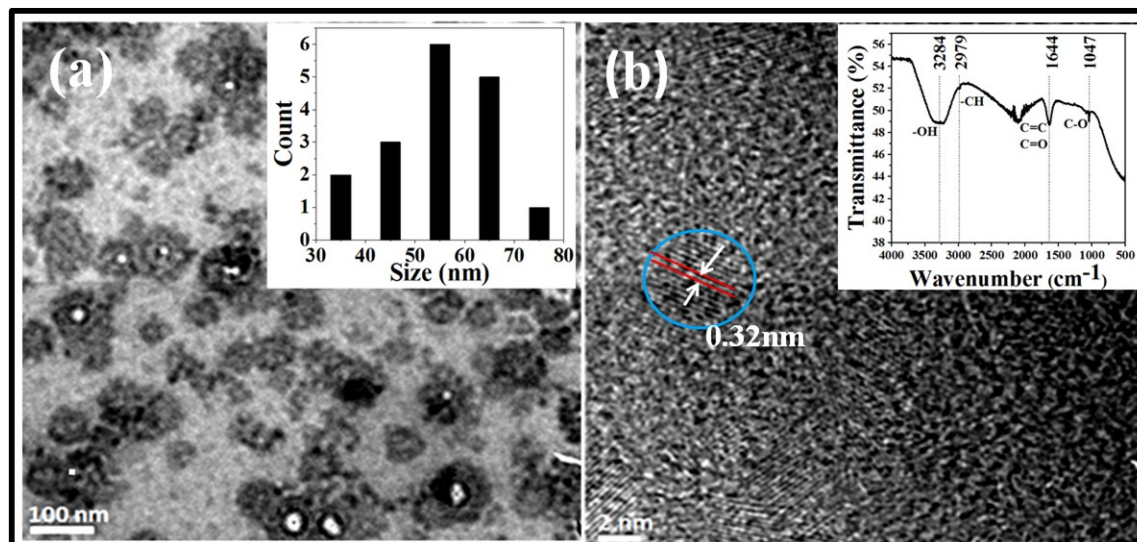


Fig. 6.1: (a) TEM image of GQDs (b) Lattice fringe image of as synthesized graphene quantum dots. Inset of 6.11(a) Size distribution of GQDs and inset of 6.1(b) FTIR spectra of GQDs.

The fluorescence in GQDs mainly arise due to the electronic state transition of charge carriers from highest occupied molecular orbital to (HOMO) to lower unoccupied molecular orbital (LUMO) upon illumination. Also, the PL emission wavelength of GQDs mainly depends upon the variation in energy gap due to particle size effect. GQDs with smaller size will have larger bandgap Shen *et al.* (2012). Different sized GQDs will show different excitation and emission spectrum. So the excitation depended fluorescent property of GQDs might be arising from the distinct particle size and different surface state existence due to the functional groups present on GQDs Zhang *et al.* (2016a). Also the surface functionalized GQDs with more hydrophilicity provides good water solubility and strong fluorescence Kumar *et al.* (2017); Shi *et al.* (2016). It mainly influences the sensing of metal ions ( $M^{2+}$  in water. Photoluminescence (PL) was taken at room temperature for pristine GQDs and GQDs with metal ion adsorbent with the excitation wavelength of 320 nm. The maximum PL intensity of pristine GQDs was observed at 440 nm. Interestingly, in compared to pristine GQDs, the maximum PL intensity of GQDs/ $(M^{2+})$  combination showed a large reduction in intensity.

The change in the intensity of fluorescence of GQDs/ $(M^{2+})$  was monitored by observing the intensity changes during the addition of different concentration of metal ions from 1 ppm, 2 ppm, 5 ppm, 10 ppm, 20 ppm, 50 ppm to 100 ppm. The sensitive response of GQDs with the addition of metal ions were analyzed by adding different metal ions such as mercury  $Hg^{2+}$ , Cadmium  $Cd^{2+}$ , and Lead  $Pb^{2+}$ . There is a gradual reduction in the PL intensity of GQDs with the increase in the  $Hg^{2+}$  concentration without any shift in peak position as shown in Fig 6.2 a. Similarly, other metal ions such as  $Cd^{2+}$ ,  $Pb^{2+}$  were also added individually to check the sensitivity of GQDs. In the presence of  $Cd^{2+}$ ,  $Pb^{2+}$  metal ions, a drastic decline in the fluorescence intensity of GQDs was observed as shown in Fig 6.2 b and c. This might be due to fluorescence quenching of GQDs. The PL intensity of GQDs was decreased with the increase in the metal ions concentration with different quenching percentage. This showed that GQDs exhibit different sensitivity towards diverse metal ions ( $M^{2+}$ ). Figure 6.2 d shows the schematic representation of turn off fluorescent quenching of GQDs by the addition of metal ions.

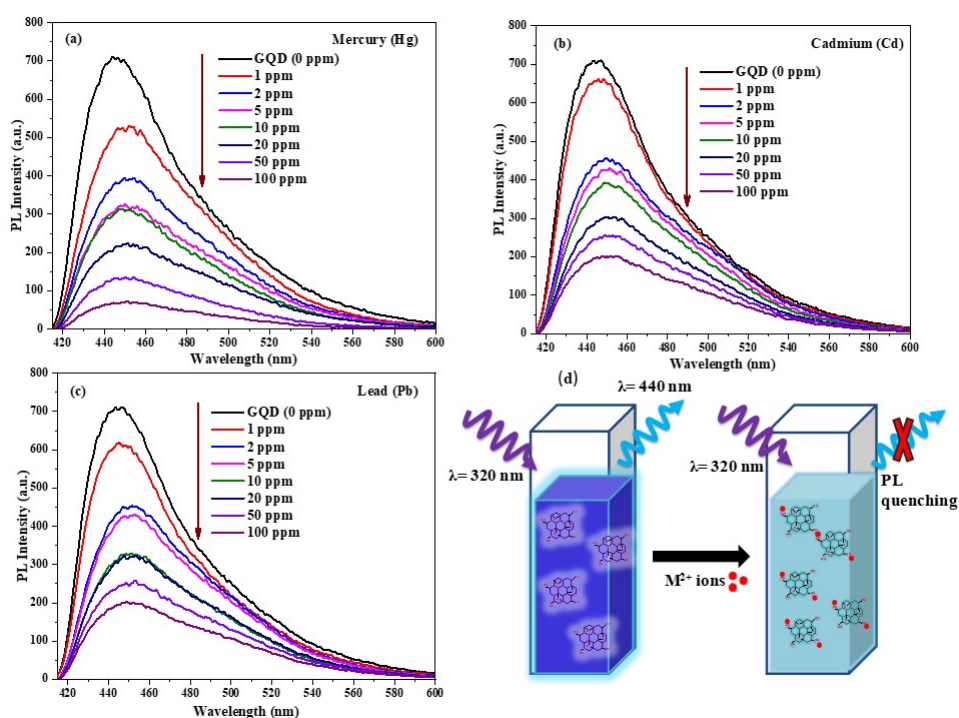


Fig. 6.2: Photoluminescence spectra of GQD in the presence of different concentration of (a)  $Hg^{2+}$  (b)  $Cd^{2+}$  (c)  $Pb^{2+}$  (d) shows the schematic of fluorescence quenching.

In order to demonstrate the sensitiveness of the proposed method and for the quantitative analysis of GQDs PL response towards ( $M^{2+}$ ), the analytical performance of the GQDs sensing system was carried out.

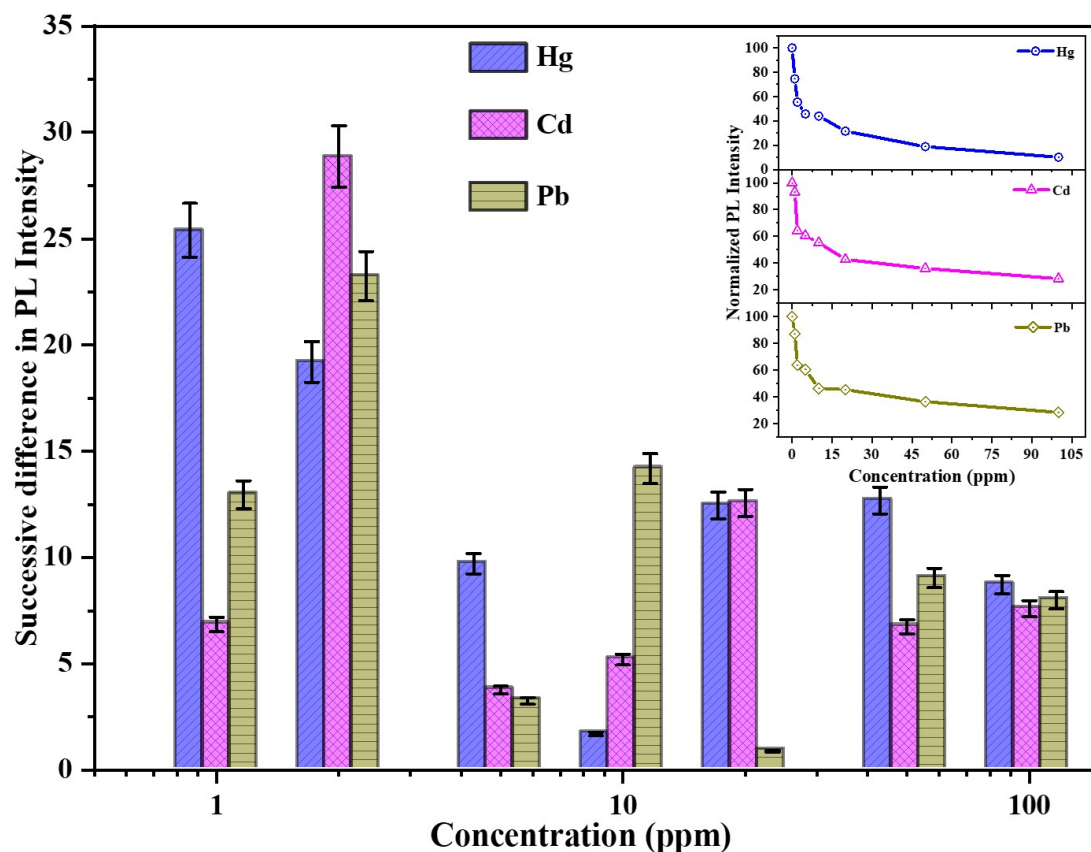


Fig. 6.3: Histogram shows the change in PL intensity with the increase of metal ion concentration for three different metal ions. Inset of the figure shows the PL intensity with different metal ion concentration.

Figure 6.3 shows the comparative study of change in PL intensity when GQDs bind with different metal ions. The quantitative variation in the PL intensity of GQDs/ $(M^{2+})$  was estimated. The PL intensity got reduced with increase in the concentration of ( $Hg^{2+}$ ,  $Cd^{2+}$  and  $Pb^{2+}$ ). The obtained histogram clearly confirms the PL changes of GQDs upon the addition of metal ions. For GQDs/ $Hg^{2+}$  combination, a maximum of 25% reduction in PL intensity is observed with the addition of 1ppm concentration of  $Hg^{2+}$  metal ion. By increasing the  $Hg^{2+}$  quencher ion concentration from 1 ppm to 2 ppm, the PL peak was quenched by 44% from the initial intensity. But the successive change in intensity from 1 to 2 ppm was only 19% from the absolute value. The GQDs interaction with 1ppm concentration of  $Cd^{2+}$  and  $Pb^{2+}$  metal ions, the obtained PL

spectrum shows only 6% and 12% decrease in PL intensity respectively. It is less than the quenching percentage of GQDs/ $Hg^{2+}$  combination. This confirms that the GQDs are more sensitive towards  $Hg^{2+}$  even with the very less level (1 ppm) quencher concentration. For,  $Cd^{2+}$  and  $Pb^{2+}$  metal ions, the maximum PL quenching with 28% and 23% reduction in PL intensity was happened with the addition of 2 ppm concentration. The increase in the concentration of quencher from 2 ppm to 5 ppm led to a successive PL intensity change of 9%, 3% and 3% respectively for  $Hg^{2+}$ ,  $Cd^{2+}$  and  $Pb^{2+}$  combinations with GQDs. Above 2 ppm for all the three metal ions the successive change in PL intensity drastically reduces. The PL quenching response becomes less sensitive when the metal ion concentration is above 2 ppm. It shows that there was only a little variation in the successive change of PL intensity with the higher concentration of metal ion. So, the maximum quenching was extremely possible with very less concentration of quencher ions. Insert of Fig 6.3 shows the plot of intensity vs. concentration of metal ions with GQDs. The intensity ratio( $I/I_0$ ) shows an inverse relationship with metal ion concentration. Apparently, it is noticed that the PL intensity is quenched linearly by  $Hg^{2+}$  until it attains 2ppm concentration. A similar quenching effect occurred in GQDs solution by the individual addition of  $Cd^{2+}$  and  $Pb^{2+}$  metal ions. The  $Hg^{2+}$ ,  $Cd^{2+}$  and  $Pb^{2+}$  metal ions showed turn-off fluorescence effect upon coordinating with the surface functionalities of GQDs. This is possibly due to strong interaction between the oxygenated functional groups such as carboxyl, carbonyl and hydroxyl and the metal ions lead to effective transfer of energy. This gives an unconventional sensing platform for metal ion detection.

The fluorescent quenching is explained by Stern-Volmer plot (S-V plot). It describes the dependency of fluorescence intensity on metal ion concentration. Basically, the quenching mechanism involves two processes, one is complexation (static quenching) and another one is collisional deactivation (dynamic quenching). The above process could be verified by the Stern-Volmer plot. The general form of Stern-Volmer equation is given in eqn 6.1 Zhang *et al.* (2016b).

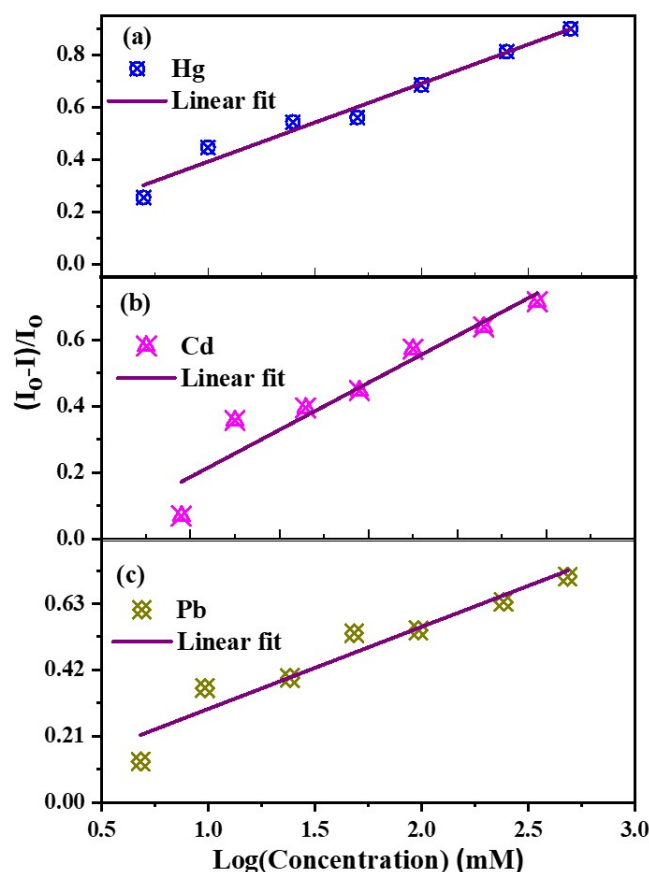


Fig. 6.4: Stern-Volmer plot for Intensity ratio with logarithmic concentration of GQDs with (a) Hg metal ion, (b) Cd metal ion and Pb metal ion. The open symbol represents the experimental point and solid line is the linear fit.

$$\frac{I_0}{I} = 1 + K_{sv}[Q] \quad (6.1)$$

Where,  $I_0$  and  $I$  are the fluorescence intensity of the GQDs before and after the presence of metal ions.  $K_{sv}$  is the Stern-Volmer constant and  $Q$  is the Quencher concentration in mMole/L.

So, the S-V plot has been drawn between the fluorescence response  $(I_0 - I)/I_0$  of GQDs/ $(M^{2+})$  and the logarithmic value of concentration of metal ions such as  $Hg^{2+}$ ,  $Cd^{2+}$  and  $Pb^{2+}$ . A lowest concentration that can be detected by the sensing unit is considered as an important parameter. From the plot, the limit of detection (LoD =  $3.3SD/m$  where,  $SD$  is the standard deviation of intercept,  $m$  is the slope of calibration curve) calculated for  $Hg^{2+}$  metal ion was  $1.171 \mu\text{M}$ . For  $Cd^{2+}$  and  $Pb^{2+}$  the LoD was  $2.455 \mu\text{M}$  and  $2.011 \mu\text{M}$  respectively.

Table 6.1: Comparison of limit of detection (LoD) of quantum dots based sensor for  $M^{2+}$  detection.

<b>Samples</b>	<b>Type of metal ion</b>	<b>LOD</b>	<b>Mechanism</b>	<b>Reference</b>
B&N Co-doped GQDs	$Hg^{2+}$	0.16 $\mu$ M	Turn-off fluorescent sensing	Yang <i>et al.</i> (2019)
N,S doped GQDs	$Hg^{2+}$	0.14 nM	Turn-off fluorescent sensing	Anh <i>et al.</i> (2017)
N doped CQD	$Hg^{2+}$	0.23 $\mu$ M	Turn-off fluorescent sensing	Zhang <i>et al.</i> (2014)
AgInZnS quantum dots	$Cd^{2+}$	37.8 nM	Turn-on fluorescent sensing	Liu <i>et al.</i> (2021)]
Gold nanoclusters/graphene oxide nanocomplex	$Cd^{2+}$	1.5 $\mu$ M	Turn-on fluorescent sensing	Ju <i>et al.</i> (2018)
N-doped GQD	$Cd^{2+}$	1.09 $\mu$ g/L	Turn-on fluorescent sensing	Naksen <i>et al.</i> (2022)
GQD with Gold nanoparticle	$Pb^{2+}$	16.7 nM	Turn-on fluorescent sensing	Niu <i>et al.</i> (2018)
S doped GQD	$Pb^{2+}$	0.03 $\mu$ M.	Turn-off fluorescent sensing	Bian <i>et al.</i> (2016)
Diethyl dithiocarbamate (DDTC) doped graphene quantum dots	$Pb^{2+}$	0.8 $\mu$ g/L	Resonant light scattering	Kaewanan <i>et al.</i> (2017)
GQD	$Hg^{2+}$	1.171 $\mu$ M	Turn-off fluorescent sensing	This work
GQD	$Cd^{2+}$	2.455 $\mu$ M	Turn-off fluorescent sensing	This work
GQD	$Pb^{2+}$	2.011 $\mu$ M	Turn-off fluorescent sensing	This work



It is worthy to point out that GQDs showed lesser LoD value for  $Hg^{2+}$  than  $Cd^{2+}$  and  $Pb^{2+}$  at the lowest concentration value of 1ppm. The limit of detection (LoD) obtained in this work in comparison to the previous reports of quantum dots based sensor for  $M^{2+}$  ( $Hg^{2+}$  than  $Cd^{2+}$  and  $Pb^{2+}$ ) detection in shown in table 6.1.

For all the three metal ions (Hg, Cd and Pb), the result shows both linear as well as nonlinear dependency between the intensity ratio and metal ion concentration shown in Fig 6.4 (a, b and c). It indicates that there was a possibility for both static and dynamic quenching. The linearity of S-V plot arises due to the effect of closer binding affinity between the GQDs and the metal ion. It enhances by the functional groups present on the basal and edges of the GQDs. The availability of ligands such as carboxyl and hydroxyl groups provide selective coordination site for the metal ions to diffuse and get adsorbed over the GQDs Brahim *et al.* (2015); Sun *et al.* (2013a). This will induce a reduction in the energy gap between GQDs and quencher due to the variation in charge transfer and change in local density of states and optical properties. This leads to static PL quenching without spectra shift Chen *et al.* (2008). On the other hand, the non-linearity of S-V plot might be due to the non-dynamic charge transfer mechanism between GQDs and quencher with more of collisional interaction without complexation followed by dynamic quenching. The information obtained from the S-V plots was not fitted with the standard Stern-Volmer equation which gave both the linear and nonlinear relationship activity of concentration with intensity. This suggested that the PL quenching process of GQDs with Hg, Cd and Pb metal ions contain both static and dynamic mechanisms Liu *et al.* (2014); Liu and Kim (2015); Sun *et al.* (2013a); Zhang *et al.* (2016b).

In Fig 6.5, plausible interpretation is proposed for the sensitive detection of metal ions via fluorescent quenching using GQDs/ $M^{2+}$ . The metal ion was attached on the surface of GQDs through functional groups with electrostatic attraction or non-covalent bonds during illumination. Upon the recognition of specific metal ions, there decrease the distance between the GQDs and  $M^{2+}$  strengthened GQDs/ $M^{2+}$  interaction, this significantly encourages the charge transfer between GQDs/ $M^{2+}$  and thus decrease the fluorescence of GQDs Sun *et al.* (2013b).

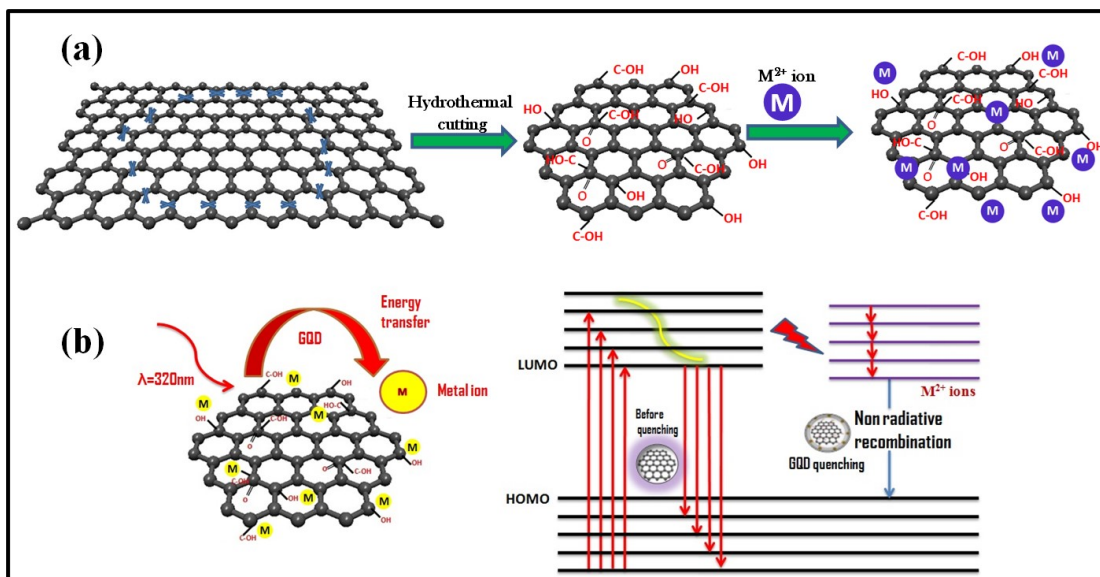


Fig. 6.5: Schematic illustration of (a) GQDs synthesis process and (b) fluorescent quenching mechanism of the GQDs in presence of the metal ions

This quenching effect arises due to the intrinsic emission effect of excited state electron transfer by the absorption of photons between the fluorophore and the metal ions which facilitates electron-hole pair recombination with a subsequent non radiative process shown in Fig 6.5. The PL quenching of GQDs also depends on the concentration of target analyte which leads to a sensitive detection of toxic metal ions. It has been already reported that fluorescence quenching of fluorophore with the presence of metal ions is possible in both bonded state and unbonded state until they are close to each other Liu *et al.* (2014) The high quenching efficiency of metal ions to the fluorescence of GQDs will provide a high sensitivity for charge transfer based sensing mechanism. Lesser the distance between the lowest unoccupied (LUMO) and highest occupied (HOMO) molecular orbital offers a greater probability of attaining nonradiative transition due to a smaller emission gap. And also, the emission gap becomes smaller than the absorption gap as a consequence of structural relaxation during photo excitation. Functional groups such as carboxyl, carbonyl and hydroxyl on the surface of the GQDs might highly facilitate the nonradiative transition through structural vibrations Chen *et al.* (2018).

## 6.4 Conclusion

In summary, the photoluminescence property of GQDs has been employed to devise an optical nanosensor for the detection of toxic heavy metal ions in aqueous media. The detection of  $Hg^{2+}$ ,  $Cd^{2+}$  and  $Pb^{2+}$  is based on the turn-off fluorescence sensing of GQDs. The fluorescent intensity of GQDs/ $M^{2+}$  system quenches with the increase in the concentration of metal ions. This is possibly due to strong interaction between the metal ion and the GQDs that enables effective energy transfer followed by the non radiative recombination of charge carriers improves the quenching process. The fluorescence quenching results and Stern-Volmer analysis shows that the quenching mechanism of GQDs with  $M^{2+}$  ions follows both the dynamic and static mechanism. The as synthesized GQDs are an efficient fluorescent probe for heavy metal ions viz.  $Hg^{2+}$ ,  $Cd^{2+}$  and  $Pb^{2+}$  with the limit of detection of 1.171  $\mu M$ , 2.455  $\mu M$  and 2.011  $\mu M$  respectively. Furthermore, these results indicate that GQDs are a viable and high potential material which could be extended as a rapid sensing unit for real time detection of heavy metals in water with good sensitivity and cost-effective protocol.

# CHAPTER 7

## CONCLUSIONS AND FUTURE SCOPE

### 7.1 Conclusion

In this thesis, the chemically exfoliated graphene oxide synthesized from the bulk graphite powder as a precursor for the fabrication of GO derivatives. The mass production of rGO with low reduction temperature, less annealing time, chemical free, ecofriendly and simple reaction environment (without inert and vacuum condition) has been achieved with the cost-effective method of thermal reduction at ambient condition.

During the reduction, an effective scalable method to synthesize PGN from rGO was achieved by optimizing the thermal reduction temperature. A detailed structural (microscopic and diffraction) studies establishes that PGN can be synthesized from the thermal reduction of GO by modifying the annealing temperature. The PGN was obtained from the reduction temperature of 300 °C. The SEM images clearly show the formation of PGN. Structural reconstruction is evidently observed from the Raman peak shift and the peak intensity ratio of the D and G peaks in GO and rGO samples using the Raman spectroscopy analysis. Furthermore, the as-obtained GO and rGO will be widely useful for various applications such as an electrode, transistors, storage devices and sensor due to the availability of larger binding sites.

The improved electrical conductance of rGO was achieved by simply controlling the degree of reduction. The two step reduction of rGO with recovered  $\pi$  conjugated graphene lattice was obtained with the removal of residual water molecules and ejection of oxygen functionalities from GO. The correlation between the electrical conductivity and the functional group of rGO was probed using FTIR spectroscopy. The increase in electrical conductivity of rGO films is correlated with improved charge transfer promoted by the elimination of hydroxyl, epoxy functional groups and recovery of native carbon bonds during reduction. It is obtained that the electrical conductance of rGO films can also be tuned by optimizing the reduction temperature.

The structural modification happened with the evolution of intermixed defects formed during the expulsion of carbon atoms creates point like defects and the conjugation of C-C bonds with the formation of new  $sp^2$  crystallites leads to line like defects simultaneously. The contribution of point and line defects on the structural reorientation of GO during oxidation and reduction was well understood by combining the theoretical and experimental analysis of first order Raman scattering. The integrated Raman peak area ( $A_D/A_G$ ) and G band spectral line width ( $\Gamma_G$ ) calculated experimentally was mapped in numerically calculated defect diagram to calculate the defect density. It is found that rGO sample reduced at 400 °C has large crystallite area ( $L_a^2$ ) of about 216  $nm^2$  and point defect density of  $\sigma = 0.00356 /nm^2$ . This shows that reduction temperature at 400 °C is optimum temperature under given conditions to synthesize good quality rGO sheets. The proposed method for the defect analysis of GO based 2D material system will be a suitable technique for the better understanding of the atomic structure during structural transformation. This will further helpful in the enhancement of material quality based on GO derivatives and integrating this material into the device.

The improved surface area and pore size of reduced GO structure was utilized to synthesis modified supercapacitor electrode material by incorporating the rGO with NiO nanoflakes. The electrochemical performance was improved with the increase of rGO percentage on NiO nanostructures. The higher specific capacitance of 417.52  $Fg^{-1}$  with the increased surface area of 1158.206  $m^2/g$  and the lowest  $R_{ct}$  value of 1.09  $\Omega$  obtained for the highest ratio of 20% rGO addition on the NiO flakes. This signifies the enhanced diffusion rate of ions in the electrolyte with the smaller diffusion resistance. So, the incorporation of rGO enhances the electrochemical performance by providing improved ion diffusion rate and higher surface area to the modified rGO/NiO electrode. The enhanced electrochemical performance of rGO/NiO nanocomposite modified electrode showed that it would be a appropriate materials for energy storage application

The photoluminescent characteristics of the hydrothermally synthesised GQD has been utilized as an optical nanosensor for the sensing of heavy metal ions in water. The turn off fluorescent quenching behaviour of GQD with the increase of metal ion concentration was observed on the basis of charge transfer sensing mechanism. The mechanism of GQD's fluorescent quenching with the existence of both static and dy-

dynamic behaviour was probed with the aid of S-V plot. The GQD without any surface grafting other than oxygen functionalities showed the limit of detection of 1.171  $\mu\text{M}$ , 2.455  $\mu\text{M}$  and 2.011  $\mu\text{M}$  for  $\text{Hg}^{2+}$ ,  $\text{Cd}^{2+}$  and  $\text{Pb}^{2+}$  metal ions.

## 7.2 Future Scope

The GO and rGO has great potential in distinct fields such as energy storage and sensor. The rGO, obtained by a simple thermal reduction can be utilized as a substitute to the existing semiconductors and metals in flexible electronics, energy storage, gas and biosensors. The method proposed in this thesis for the defect analysis of GO based 2D material system can be used for the better understanding of the atomic structure during structural transformation. The rGO can be made in to a composite with other nanostructural material will be a suitable material for energy storage, sensing, hydrogen evaluation, oxygen evaluation and water splitting application. [The as synthesized rGO based rGO/NiO nanocomposite can be surface modified and further used in the development of electrochemical sensors with high selectivity and sensitivity and in asymmetric supercapacitor device with higher energy and power density values. The visible challenges in achieving better performance like high energy density, power density and extended life cycle, can be further improved by optimizing the material characteristics such as surface area, electrochemical activity, porosity and active sites. The combination of hetero metal/metal oxide/polymer based rGO composites with unique features can accomplish the needs of small, huge and durable energy devices. This facile synthesis and development of rGO based materials with enhanced characteristics would contribute an extensive, durable and alternative solution to the current and future energy requirements.](#) Further the surface decorated GQD with improved active sites and surface area also can be used as an electrode material in energy storage applications. The GQD can be doped with appropriate dopants like nitrogen, sulphur, polymer and biomolecules and etc will modify the surface charge and can be used in optical sensors for the real time sensing of distinct heavy metal ions and other hazardous substances.

## REFERENCES

1. **Abdolmohammadi, S.** and **M. Afsharpour** (2021). An ultrasound assisted cyclocondensation reaction for the efficient synthesis of [1] benzopyranopyrido [d] pyrimidines using porous graphene/moo3. *Applied Organometallic Chemistry*, **35**(1), 6028.
2. **Abid, P. Sehrawat, S. S. Islam, P. Mishra,** and **S. Ahmad** (2018). Reduced graphene oxide (rGO) based wideband optical sensor and the role of Temperature, Defect States and Quantum Efficiency. *Scientific Reports*, **8**(1), 3537.
3. **Acik, M., G. Lee, C. Mattevi, A. Pirkle, R. M. Wallace, M. Chhowalla, K. Cho,** and **Y. Chabal** (2011). The role of oxygen during thermal reduction of graphene oxide studied by infrared absorption spectroscopy. *The Journal of Physical Chemistry C*, **115**(40), 19761–19781.
4. **Ahmad, W., Z. Ullah, N. I. Sonil,** and **K. Khan** (2021). Introduction, production, characterization and applications of defects in graphene. *Journal of Materials Science: Materials in Electronics*, **32**(15), 19991–20030.
5. **Akinwande, D., C. Huyghebaert, C.-H. Wang, M. I. Serna, S. Goossens, L.-J. Li, H.-S. P. Wong,** and **F. H. Koppens** (2019). Graphene and two-dimensional materials for silicon technology. *Nature*, **573**(7775), 507–518.
6. **Aliyev, E., V. Filiz, M. M. Khan, Y. J. Lee, C. Abetz,** and **V. Abetz** (2019). Structural Characterization of Graphene Oxide: Surface Functional Groups and Fractionated Oxidative Debris. *Nanomaterials*, **9**(8).
7. **Aminuddin Rosli, N. H., K. S. Lau, T. Winie, S. X. Chin,** and **C. H. Chia** (2021). Microwave-assisted reduction of graphene oxide for an electrochemical supercapacitor: Structural and capacitance behavior. *Materials Chemistry and Physics*, **262**, 124274.
8. **Anh, N. T. N., A. D. Chowdhury,** and **R.-a. Doong** (2017). Highly sensitive and selective detection of mercury ions using N, S-codoped graphene quantum dots and its paper strip based sensing application in wastewater. *Sensors and Actuators B: Chemical*, **252**, 1169–1178.
9. **Ansari, A. R., S. A. Ansari, N. Parveen, M. O. Ansari,** and **Z. Osman** (2022). Silver nanoparticle decorated on reduced graphene oxide-wrapped manganese oxide nanorods as electrode materials for high-performance electrochemical devices. *Crystals*, **12**(3), 389.
10. **Antink, W. H., Y. Choi, K.-d. Seong, J. M. Kim,** and **Y. Piao** (2018). Recent Progress in Porous Graphene and Reduced Graphene Oxide-Based Nanomaterials for Electrochemical Energy Storage Devices. *Advanced Materials Interfaces*, **5**(5), 1701212.

11. **Asen, P., M. Haghghi, S. Shahrokhian, and N. Taghavinia** (2019). One step synthesis of  $\text{SnS}_2\text{-SnO}_2$  nano-heterostructured as an electrode material for supercapacitor applications. *Journal of Alloys and Compounds*, **782**, 38–50.
12. **Asgar, H., K. Deen, U. Riaz, Z. U. Rahman, U. H. Shah, and W. Haider** (2018). Synthesis of graphene via ultra-sonic exfoliation of graphite oxide and its electrochemical characterization. *Materials Chemistry and Physics*, **206**, 7–11.
13. **Askari, M. B., P. Salarizadeh, M. Seifi, S. M. Rozati, and A. Beheshti-Marnani** (2020). Binary mixed molybdenum cobalt sulfide nanosheets decorated on rgo as a high-performance supercapacitor electrode. *Nanotechnology*, **31**(27), 275406.
14. **Atamny, F., O. Spillecke, and R. Schlögl** (1999). On the stm imaging contrast of graphite: towards a true atomic resolution. *Physical Chemistry Chemical Physics*, **1**(17), 4113–4118.
15. **Bagri, A., C. Mattevi, M. Acik, Y. J. Chabal, M. Chhowalla, and V. B. Shenoy** (2010). Structural evolution during the reduction of chemically derived graphene oxide. *Nature Chemistry*, **2**(7), 581–587.
16. **Baig, N., A. Waheed, M. Sajid, I. Khan, A.-N. Kawde, and M. Sohail** (2021). Porous graphene-based electrodes: Advances in electrochemical sensing of environmental contaminants. *Trends in Environmental Analytical Chemistry*, **30**, e00120.
17. **Banhart, F., J. Kotakoski, and A. V. Krasheninnikov** (2011). Structural defects in graphene. *ACS nano*, **5**(1), 26–41.
18. **Batista, R. M. F., E. Oliveira, S. P. G. Costa, C. Lodeiro, and M. M. M. Raposo** (2007). Synthesis and Ion Sensing Properties of New Colorimetric and Fluorimetric Chemosensors Based on Bithienyl-Imidazo-Anthraquinone Chromophores. *Organic Letters*, **9**(17), 3201–3204.
19. **Beams, R., L. G. Cançado, and L. Novotny** (2011). Low temperature raman study of the electron coherence length near graphene edges. *Nano Letters*, **11**(3), 1177–1181.
20. **Berger, C., Z. Song, X. Li, X. Wu, N. Brown, C. Naud, D. Mayou, T. Li, J. Hass, A. N. Marchenkov, et al.** (2006). Electronic confinement and coherence in patterned epitaxial graphene. *Science*, **312**(5777), 1191–1196.
21. **Bernal, M. M., M. Tortello, S. Colonna, G. Saracco, and A. Fina** (2017). Thermally and Electrically Conductive Nanopapers from Reduced Graphene Oxide: Effect of Nanoflakes Thermal Annealing on the Film Structure and Properties. *Nanomaterials*, **7**(12), 428.
22. **Bhaskaram, D. S. and G. Govindaraj** (2018). Carrier transport in reduced graphene oxide probed using raman spectroscopy. *The Journal of Physical Chemistry C*, **122**(19), 10303–10308.
23. **Bhattacharjee, Y., S. Biswas, and S. Bose** (2020). Thermoplastic polymer composites for emi shielding applications. *Materials for Potential EMI Shielding Applications*, 73–99.



24. **Bian, S., C. Shen, H. Hua, L. Zhou, H. Zhu, F. Xi, J. Liu, and X. Dong** (2016). One-pot synthesis of sulfur-doped graphene quantum dots as a novel fluorescent probe for highly selective and sensitive detection of lead(II). *RSC Advances*, **6**(74), 69977–69983.
25. **Bings, N. H., A. Bogaerts, and J. A. C. Broekaert** (2006). Atomic Spectroscopy. *Analytical Chemistry*, **78**(12), 3917–3946.
26. **Boas, C., B. Focassio, E. Marinho, D. Larrude, M. Salvadori, C. R. Leão, and D. J. Dos Santos** (2019). Characterization of nitrogen doped graphene bilayers synthesized by fast, low temperature microwave plasma-enhanced chemical vapour deposition. *Scientific reports*, **9**(1), 1–12.
27. **Brahim, N. B., N. B. H. Mohamed, M. Echabaane, M. Haouari, R. B. Chaâbane, M. Negrierie, and H. B. Ouada** (2015). Thioglycerol-functionalized CdSe quantum dots detecting cadmium ions. *Sensors and Actuators B: Chemical*, **220**, 1346–1353.
28. **Brisebois, P. and M. Sijaj** (2020). Harvesting graphene oxide—years 1859 to 2019: a review of its structure, synthesis, properties and exfoliation. *Journal of Materials Chemistry C*, **8**(5), 1517–1547.
29. **Brodie, B.** (1859). On the atomic weight of graphite. *J storage* 149: 249–259.
30. **Butler, O. T., J. M. Cook, C. F. Harrington, S. J. Hill, J. Rieuwerts, and D. L. Miles** (2006). Atomic spectrometry update. Environmental analysis. *J. Anal. At. Spectrom.*, **21**(2), 217–243.
31. **Cai, M., D. Thorpe, D. H. Adamson, and H. C. Schniepp** (2012). Methods of graphite exfoliation. *Journal of Materials Chemistry*, **22**(48), 24992–25002.
32. **Calizo, I., A. A. Balandin, W. Bao, F. Miao, and C. N. Lau** (2007). Temperature Dependence of the Raman Spectra of Graphene and Graphene Multilayers. *Nano Letters*, **7**(9), 2645–2649. ISSN 1530-6984.
33. **Cançado, L. G., A. Jorio, and M. A. Pimenta** (2007). Measuring the absolute Raman cross section of nanographites as a function of laser energy and crystallite size. *Physical Review B*, **76**(6), 064304.
34. **Cançado, L. G., M. A. Pimenta, B. R. A. Neves, M. S. S. Dantas, and A. Jorio** (2004). Influence of the Atomic Structure on the Raman Spectra of Graphite Edges. *Physical Review Letters*, **93**(24), 247401.
35. **Cançado, L., K. Takai, T. Enoki, M. Endo, Y. Kim, H. Mizusaki, A. Jorio, L. Coelho, R. Magalhães-Paniago, and M. Pimenta** (2006). General equation for the determination of the crystallite size  $l_a$  of nanographite by raman spectroscopy. *Applied Physics Letters*, **88**(16), 163106.
36. **Cançado, L. G., M. G. Da Silva, E. H. M. Ferreira, F. Hof, K. Kampioti, K. Huang, A. Pénicaud, C. A. Achete, R. B. Capaz, and A. Jorio** (2017). Disentangling contributions of point and line defects in the raman spectra of graphene-related materials. *2D Materials*, **4**(2), 025039.

37. **Cao, Y., Y. Cheng, and M. Sun** (2021). Graphene-based sers for sensor and catalysis. *Applied Spectroscopy Reviews*, 1–38.
38. **Carozo, V., C. M. Almeida, E. H. M. Ferreira, L. G. Cançado, C. A. Achete, and A. Jorio** (2011). Raman Signature of Graphene Superlattices. *Nano Letters*, **11**(11), 4527–4534.
39. **Carrera, C., J. M. González-Domnguez, F. J. Pascual, A. Ansón-Casaos, A. M. Benito, W. K. Maser, and E. García-Bordejé** (2020). Modification of Physico-chemical Properties and Boosting Electrical Conductivity of Reduced Graphene Oxide Aerogels by Postsynthesis Treatment. *The Journal of Physical Chemistry C*, **124**(25), 13739–13752.
40. **Casiraghi, C., A. Hartschuh, H. Qian, S. Piscanec, C. Georgi, A. Fasoli, K. S. Novoselov, D. M. Basko, and A. C. Ferrari** (2009). Raman Spectroscopy of Graphene Edges. *Nano Letters*, **9**(4), 1433–1441.
41. **Chandra, A., S. Deshpande, D. B. Shinde, V. K. Pillai, and N. Singh** (2014). Mitigating the Cytotoxicity of Graphene Quantum Dots and Enhancing Their Applications in Bioimaging and Drug Delivery. *ACS Macro Letters*, **3**(10), 1064–1068.
42. **Chen, C.-M., Q. Zhang, C.-H. Huang, X.-C. Zhao, B.-S. Zhang, Q.-Q. Kong, M.-Z. Wang, Y.-G. Yang, R. Cai, and D. S. Su** (2012). Macroporous bubble graphene film via template-directed ordered-assembly for high rate supercapacitors. *Chemical Communications*, **48**(57), 7149–7151.
43. **Chen, G., H. Guan, C. Dong, X. Xiao, and Y. Wang** (2016a). Effect of calcination temperatures on the electrochemical performances of nickel oxide/reduction graphene oxide (nio/rgo) composites synthesized by hydrothermal method. *Journal of Physics and Chemistry of Solids*, **98**, 209–219.
44. **Chen, J., Y. Gao, C. Guo, G. Wu, Y. Chen, and B. Lin** (2008). Facile synthesis of water-soluble and size-homogeneous cadmium selenide nanoparticles and their application as a long-wavelength fluorescent probe for detection of Hg(II) in aqueous solution. *Spectrochimica Acta Part A: Molecular and Biomolecular Spectroscopy*, **69**(2), 572–579.
45. **Chen, J., B. Yao, C. Li, and G. Shi** (2013). An improved hummers method for eco-friendly synthesis of graphene oxide. *Carbon*, **64**, 225–229.
46. **Chen, S., X. Hai, X.-W. Chen, and J.-H. Wang** (2014). In Situ Growth of Silver Nanoparticles on Graphene Quantum Dots for Ultrasensitive Colorimetric Detection of H<sub>2</sub>O<sub>2</sub> and Glucose. *Analytical Chemistry*, **86**(13), 6689–6694.
47. **Chen, S., N. Ullah, T. Wang, and R. Zhang** (2018). Tuning the optical properties of graphene quantum dots by selective oxidation: a theoretical perspective. *Journal of Materials Chemistry C*, **6**(25), 6875–6883.
48. **Chen, Y., K. Fu, S. Zhu, W. Luo, Y. Wang, Y. Li, E. Hitz, Y. Yao, J. Dai, J. Wan, and others** (2016b). Reduced graphene oxide films with ultrahigh conductivity as Li-ion

- battery current collectors. *Nano letters*, **16**(6), 3616–3623. Publisher: ACS Publications.
49. **Chen, Y. and Z. Rosenzweig** (2002). Luminescent CdS Quantum Dots as Selective Ion Probes. *Analytical Chemistry*, **74**(19), 5132–5138.
  50. **Chen, Z., W. Ren, L. Gao, B. Liu, S. Pei, and H.-M. Cheng** (2011). Three-dimensional flexible and conductive interconnected graphene networks grown by chemical vapour deposition. *Nature Materials*, **10**(6), 424–428.
  51. **Chisholm, M. F., G. Duscher, and W. Windl** (2012). Oxidation resistance of reactive atoms in graphene. *Nano letters*, **12**(9), 4651–4655.
  52. **Choi, B. G., M. Yang, W. H. Hong, J. W. Choi, and Y. S. Huh** (2012). 3D Macroporous Graphene Frameworks for Supercapacitors with High Energy and Power Densities. *ACS Nano*, **6**(5), 4020–4028.
  53. **Choo, S.-S., E.-S. Kang, I. Song, D. Lee, J.-W. Choi, and T.-H. Kim** (2017). Electrochemical detection of dopamine using 3D porous graphene oxide/gold nanoparticle composites. *Sensors*, **17**(4), 861. Publisher: Multidisciplinary Digital Publishing Institute.
  54. **Chowdhury, P. et al.** (2021). Functionalized cdte fluorescence nanosensor for the sensitive detection of water borne environmentally hazardous metal ions. *Optical Materials*, **111**, 110584.
  55. **Chua, C. K. and M. Pumera** (2012). Renewal of sp<sup>2</sup> bonds in graphene oxides via dehydrobromination. *Journal of Materials Chemistry*, **22**(43), 23227–23231.
  56. **Claramunt, S., A. Varea, D. López-Díaz, M. M. Velázquez, A. Cornet, and A. Cirera** (2015). The Importance of Interbands on the Interpretation of the Raman Spectrum of Graphene Oxide. *The Journal of Physical Chemistry C*, **119**(18), 10123–10129.
  57. **Costa-Fernández, J. M., R. Pereiro, and A. Sanz-Medel** (2006). The use of luminescent quantum dots for optical sensing. *TrAC Trends in Analytical Chemistry*, **25**(3), 207–218.
  58. **Daneshvar, F., A. Aziz, A. M. Abdelkader, T. Zhang, H.-J. Sue, and M. E. Welland** (2018). Porous sno<sub>2</sub>-cuxo nanocomposite thin film on carbon nanotubes as electrodes for high performance supercapacitors. *Nanotechnology*, **30**(1), 015401.
  59. **Dao, V.-D., N. D. Hoa, N. H. Vu, D. V. Quang, N. Van Hieu, T. T. N. Dung, N. X. Viet, C. M. Hung, and H.-S. Choi** (2019). A facile synthesis of ruthenium/reduced graphene oxide nanocomposite for effective electrochemical applications. *Solar Energy*, **191**, 420–426.
  60. **Ding, R., W. Li, X. Wang, T. Gui, B. Li, P. Han, H. Tian, A. Liu, X. Wang, X. Liu, et al.** (2018). A brief review of corrosion protective films and coatings based on graphene and graphene oxide. *Journal of Alloys and Compounds*, **764**, 1039–1055.

61. **Dolbin, A. V., M. V. Khlistuck, V. B. Esel'son, V. G. Gavrillo, N. A. Vinnikov, R. M. Basnukaeva, A. I. Prokhvatilov, I. V. Legchenkova, V. V. Meleshko, W. K. Maser, and A. M. Benito** (2017). The effect of the thermal reduction on the kinetics of low-temperature  $^4\text{He}$  sorption and the structural characteristics of graphene oxide. *Low Temperature Physics*, **43**(3), 383–389.
62. **Dreyer, D. R., S. Park, C. W. Bielawski, and R. S. Ruoff** (2009). The chemistry of graphene oxide. *Chemical Society Reviews*, **39**(1), 228–240.
63. **Duan, J., X. Jiang, S. Ni, M. Yang, and J. Zhan** (2011). Facile synthesis of n-acetyl-l-cysteine capped zns quantum dots as an eco-friendly fluorescence sensor for  $\text{Hg}^{2+}$ . *Talanta*, **85**(4), 1738–1743.
64. **Eckmann, A., A. Felten, A. Mishchenko, L. Britnell, R. Krupke, K. S. Novoselov, and C. Casiraghi** (2012). Probing the nature of defects in graphene by Raman spectroscopy. *Nano letters*, **12**(8), 3925–3930.
65. **Eda, G., C. Mattevi, H. Yamaguchi, H. Kim, and M. Chhowalla** (2009). Insulator to Semimetal Transition in Graphene Oxide. *The Journal of Physical Chemistry C*, **113**(35), 15768–15771.
66. **Eigler, S., C. Dotzer, and A. Hirsch** (2012). Visualization of defect densities in reduced graphene oxide. *Carbon*, **50**(10), 3666–3673.
67. **Eigler, S., S. Grimm, M. Enzelberger-Heim, P. Müller, and A. Hirsch** (2013). Graphene oxide: efficiency of reducing agents. *Chemical Communications*, **49**(67), 7391–7393.
68. **El-Hout, S. I., S. G. Mohamed, A. Gaber, S. Y. Attia, A. Shawky, and S. M. El-Sheikh** (2021). High electrochemical performance of rgo anchored cus nanospheres for supercapacitor applications. *Journal of Energy Storage*, **34**, 102001.
69. **Erickson, K., R. Erni, Z. Lee, N. Alem, W. Gannett, and A. Zettl** (2010). Determination of the local chemical structure of graphene oxide and reduced graphene oxide. *Advanced materials*, **22**(40), 4467–4472.
70. **ervenka, J. and C. F. J. Flipse** (2009). Structural and electronic properties of grain boundaries in graphite: Planes of periodically distributed point defects. *Physical Review B*, **79**(19), 195429.
71. **Fan, Z., Q. Zhao, T. Li, J. Yan, Y. Ren, J. Feng, and T. Wei** (2012). Easy synthesis of porous graphene nanosheets and their use in supercapacitors. *Carbon*, **50**(4), 1699–1703.
72. **Faucett, A. C., J. N. Flournoy, J. S. Mehta, and J. M. Mativetsky** (2017). Evolution, structure, and electrical performance of voltage-reduced graphene oxide. *FlatChem*, **1**, 42–51.
73. **Feicht, P. and S. Eigler** (2018). Defects in graphene oxide as structural motifs. *Chem-NanoMat*, **4**(3), 244–252.

74. **Ferrari, A. C.** (2007). Raman spectroscopy of graphene and graphite: Disorder, electron–phonon coupling, doping and nonadiabatic effects. *Solid state communications*, **143**(1-2), 47–57.
75. **Ferrari, A. C., J. C. Meyer, V. Scardaci, C. Casiraghi, M. Lazzeri, F. Mauri, S. Piscanec, D. Jiang, K. S. Novoselov, S. Roth, and A. K. Geim** (2006). Raman Spectrum of Graphene and Graphene Layers. *Physical Review Letters*, **97**(18), 187401.
76. **Ferrari, A. C. and J. Robertson** (2001). Resonant raman spectroscopy of disordered, amorphous, and diamondlike carbon. *Physical review B*, **64**(7), 075414.
77. **Frasco, M. and N. Chaniotakis** (2009). Semiconductor Quantum Dots in Chemical Sensors and Biosensors. *Sensors*, **9**(9), 7266–7286.
78. **Gajurel, P., M. Kim, Q. Wang, W. Dai, H. Liu, and C. Cen** (2017). Vacancy-controlled contact friction in graphene. *Advanced Functional Materials*, **27**(47), 1702832.
79. **Ganganboina, A. B., A. Dutta Chowdhury, and R.-a. Doong** (2018). N-Doped Graphene Quantum Dots-Decorated V2O5 Nanosheet for Fluorescence Turn Off/On Detection of Cysteine. *ACS Applied Materials & Interfaces*, **10**(1), 614–624.
80. **Gao, X., J. Jang, and S. Nagase** (2010). Hydrazine and Thermal Reduction of Graphene Oxide: Reaction Mechanisms, Product Structures, and Reaction Design. *The Journal of Physical Chemistry C*, **114**(2), 832–842.
81. **Ghosh, K. and S. K. Srivastava** (2020). Superior supercapacitor performance of bi 2 s 3 nanorod/reduced graphene oxide composites. *Dalton Transactions*, **49**(46), 16993–17004.
82. **Gómez-Navarro, C., J. C. Meyer, R. S. Sundaram, A. Chuvilin, S. Kurasch, M. Burghard, K. Kern, and U. Kaiser** (2010). Atomic Structure of Reduced Graphene Oxide. *Nano Letters*, **10**(4), 1144–1148.
83. **Gómez-Navarro, C., R. T. Weitz, A. M. Bittner, M. Scolari, A. Mews, M. Burghard, and K. Kern** (2009). Electronic Transport Properties of Individual Chemically Reduced Graphene Oxide Sheets. *Nano Letters*, **9**(5), 2206–2206.
84. **Gong, C., M. Acik, R. M. Abolfath, Y. Chabal, and K. Cho** (2012). Graphitization of Graphene Oxide with Ethanol during Thermal Reduction. *The Journal of Physical Chemistry C*, **116**(18), 9969–9979. ISSN 1932-7447.
85. **Govindarajan, D., V. Uma Shankar, and R. Gopalakrishnan** (2019). Supercapacitor behavior and characterization of rgo anchored v2o5 nanorods. *Journal of Materials Science: Materials in Electronics*, **30**(17), 16142–16155.
86. **Guex, L. G., B. Sacchi, K. F. Peuvot, R. L. Andersson, A. M. Pourrahimi, V. Ström, S. Farris, and R. T. Olsson** (2017). Experimental review: chemical reduction of graphene oxide (go) to reduced graphene oxide (rgo) by aqueous chemistry. *Nanoscale*, **9**(27), 9562–9571.

87. **Gui, J., J. Zhang, T. Liu, Y. Peng, and J. Chang** (2017). Two-step controllable preparation of nio nanocrystal anchored reduced graphene oxide sheets and their electrochemical performance as supercapacitors. *New Journal of Chemistry*, **41**(19), 10695–10702.
88. **Guo, C., Y. Cai, H. Zhao, D. Wang, Y. Hou, J. Lv, H. Qu, D. Dai, X. Cai, J. Lu, and J. Cai** (2019). Efficient synthesis of graphene oxide by Hummers method assisted with an electric field. *Materials Research Express*, **6**(5), 055602.
89. **Guo, R., S. Zhou, Y. Li, X. Li, L. Fan, and N. H. Voelcker** (2015). Rhodamine-Functionalized Graphene Quantum Dots for Detection of Fe<sup>3+</sup> in Cancer Stem Cells. *ACS Applied Materials & Interfaces*, **7**(43), 23958–23966.
90. **Gupta, B., N. Kumar, K. Panda, V. Kanan, S. Joshi, and I. Visoly-Fisher** (2017). Role of oxygen functional groups in reduced graphene oxide for lubrication. *Scientific reports*, **7**(1), 1–14.
91. **Haghighy, F., R. Salahandish, M. Hassani, and A. Sanati-Nezhad** (2022). Highly stable buffer-based zinc oxide/reduced graphene oxide nanosurface chemistry for rapid immunosensing of sars-cov-2 antigens. *ACS Applied Materials & Interfaces*, **14**(8), 10844–10855.
92. **Hu, Z., Y. Chen, Q. Hou, R. Yin, F. Liu, and H. Chen** (2012). Characterization of graphite oxide after heat treatment. *New Journal of Chemistry*, **36**(6), 1373–1377.
93. **Huang, H.-H., K. K. H. De Silva, G. Kumara, and M. Yoshimura** (2018). Structural evolution of hydrothermally derived reduced graphene oxide. *Scientific reports*, **8**(1), 1–9.
94. **Huang, X., K. Qian, J. Yang, J. Zhang, L. Li, C. Yu, and D. Zhao** (2012). Functional nanoporous graphene foams with controlled pore sizes. *Advanced materials*, **24**(32), 4419–4423.
95. **Hummers Jr, W. S. and R. E. Offeman** (1958). Preparation of graphitic oxide. *Journal of the american chemical society*, **80**(6), 1339–1339.
96. **Iqra, M., F. Anwar, R. Jan, and M. A. Mohammad** (2022). A flexible piezoresistive strain sensor based on laser scribed graphene oxide on polydimethylsiloxane. *Scientific Reports*, **12**(1), 1–11.
97. **Iskandar, F., U. Hikmah, E. Stavila, and A. H. Aimon** (2017). Microwave-assisted reduction method under nitrogen atmosphere for synthesis and electrical conductivity improvement of reduced graphene oxide (rGO). *RSC Advances*, **7**(83), 52391–52397.
98. **Ismail, Z.** (2019). Green reduction of graphene oxide by plant extracts: a short review. *Ceramics International*, **45**(18), 23857–23868.
99. **J, P., P. D, V. Ks, B. K, S. N, and V. Gd** (2020). Nanocomposite chitosan film containing graphene oxide/hydroxyapatite/gold for bone tissue engineering. *International Journal of Biological Macromolecules*, **154**, 62–71.

100. **Joseph, L., B.-M. Jun, J. R. V. Flora, C. M. Park, and Y. Yoon** (2019). Removal of heavy metals from water sources in the developing world using low-cost materials: A review. *Chemosphere*, **229**, 142–159.
101. **Joshi, S. R., A. Sharma, G.-H. Kim, and J. Jang** (2020). Low cost synthesis of reduced graphene oxide using biopolymer for influenza virus sensor. *Materials Science and Engineering: C*, **108**, 110465.
102. **Ju, C., X. Gong, W. Song, Y. Zhao, and R. Li** (2018). Turn-on fluorescent probe for Cd<sup>2+</sup> detection by gold nanoclusters/graphene oxide nanocomplex. *Micro & Nano Letters*, **13**(6), 804–806.
103. **Jung, I., D. A. Dikin, R. D. Piner, and R. S. Ruoff** (2008). Tunable Electrical Conductivity of Individual Graphene Oxide Sheets Reduced at Low Temperatures. *Nano Letters*, **8**(12), 4283–4287.
104. **Kaewanan, P., P. Sricharoen, N. Limchoowong, T. Sripakdee, P. Nuengmatcha, and S. Chanthai** (2017). A fluorescence switching sensor based on graphene quantum dots decorated with Hg<sup>2+</sup> and hydrolyzed thioacetamide for highly Ag<sup>+</sup>-sensitive and selective detection. *RSC Advances*, **7**(76), 48058–48067.
105. **Kaewprom, C., P. Sricharoen, N. Limchoowong, P. Nuengmatcha, and S. Chanthai** (2019). Resonance light scattering sensor of the metal complex nanoparticles using diethyl dithiocarbamate doped graphene quantum dots for highly Pb(II)-sensitive detection in water sample. *Acta Part A: Molecular and Biomolecular Spectroscopy*, **207**, 79–87.
106. **Kalkal, A., R. Pradhan, S. Kadian, G. Manik, and G. Packirisamy** (2020). Bio-functionalized Graphene Quantum Dots Based Fluorescent Biosensor toward Efficient Detection of Small Cell Lung Cancer. *ACS Applied Bio Materials*, **3**(8), 4922–4932.
107. **Kamat, A. M., Y. Pei, and A. G. Kottapalli** (2019). Bioinspired cilia sensors with graphene sensing elements fabricated using 3d printing and casting. *Nanomaterials*, **9**(7), 954.
108. **Kaniyoor, A., T. T. Baby, T. Arockiadoss, N. Rajalakshmi, and S. Ramaprabhu** (2011). Wrinkled Graphenes: A Study on the Effects of Synthesis Parameters on Exfoliation-Reduction of Graphite Oxide. *The Journal of Physical Chemistry C*, **115**(36), 17660–17669.
109. **Ke, Q. and J. Wang** (2016). Graphene-based materials for supercapacitor electrodes—a review. *Journal of Materiomics*, **2**(1), 37–54.
110. **Khaliha, S., T. D. Marforio, A. Kovtun, S. Mantovani, A. Bianchi, M. L. Navacchia, M. Zambianchi, L. Bocchi, N. Boulanger, A. Iakunkov, et al.** (2021). Defective graphene nanosheets for drinking water purification: Adsorption mechanism, performance, and recovery. *FlatChem*, **29**, 100283.
111. **Khose, R. V., G. Chakraborty, M. P. Bondarde, P. H. Wadekar, A. K. Ray, and S. Some** (2021). Red-fluorescent graphene quantum dots from guava leaf as a turn-off probe for sensing aqueous Hg(II). *New Journal of Chemistry*, **45**(10), 4617–4625.

112. **Kim, K. S., Y. Zhao, H. Jang, S. Y. Lee, J. M. Kim, K. S. Kim, J.-H. Ahn, P. Kim, J.-Y. Choi, and B. H. Hong** (2009). Large-scale pattern growth of graphene films for stretchable transparent electrodes. *nature*, **457**(7230), 706–710.
113. **King, A. A., B. R. Davies, N. Noorbehesht, P. Newman, T. L. Church, A. T. Harris, J. M. Razal, and A. I. Minett** (2016). A new raman metric for the characterisation of graphene oxide and its derivatives. *Scientific reports*, **6**(1), 1–6.
114. **Kumar, G., N. K. Mogha, M. Kumar, D. T. Masram, et al.** (2020). Nio nanocomposites/rgo as a heterogeneous catalyst for imidazole scaffolds with applications in inhibiting the dna binding activity. *Dalton Transactions*, **49**(6), 1963–1974.
115. **Kumar, V., V. Kumar, G. B. Reddy, and R. Pasricha** (2015). Thermal deoxygenation causes photoluminescence shift from UV to blue region in lyophilized graphene oxide. *RSC Advances*, **5**(91), 74342–74346.
116. **Kumar, V. V., T. Raman, and S. P. Anthony** (2017). Fluorescent carbon quantum dots chemosensor for selective turn-on sensing of Zn<sup>2+</sup> and turn-off sensing of Pb<sup>2+</sup> in aqueous medium and zebrafish eggs. *New Journal of Chemistry*, **41**(24), 15157–15164.
117. **Kumawat, M. K., M. Thakur, R. B. Gurung, and R. Srivastava** (2017). Graphene Quantum Dots for Cell Proliferation, Nucleus Imaging, and Photoluminescent Sensing Applications. *Scientific Reports*, **7**(1), 15858.
118. **Kurian, M.** (2021). Recent progress in the chemical reduction of graphene oxide by green reductants—a mini review. *Carbon Trends*, **5**, 100120.
119. **Lalwani, G., J. L. Sundararaj, K. Schaefer, T. Button, and B. Sitharaman** (2014). Synthesis, characterization, in vitro phantom imaging, and cytotoxicity of a novel graphene-based multimodal magnetic resonance imaging-X-ray computed tomography contrast agent. *J. Mater. Chem. B*, **2**(22), 3519–3530.
120. **Larciprete, R., S. Fabris, T. Sun, P. Lacovig, A. Baraldi, and S. Lizzit** (2011). Dual Path Mechanism in the Thermal Reduction of Graphene Oxide. *Journal of the American Chemical Society*, **133**(43), 17315–17321.
121. **Le, Q. B., T.-H. Nguyen, H. Fei, C. Bubulinca, L. Munster, N. Bugarova, M. Micusik, R. Kiefer, T. T. Dao, M. Omastova, et al.** (2022). Electrochemical performance of composite electrodes based on rgo, mn/cu metal–organic frameworks, and pani. *Scientific Reports*, **12**(1), 1–13.
122. **Lee, B. H., R. L. McKinney, M. T. Hasan, and A. V. Naumov** (2021). Graphene Quantum Dots as Intracellular Imaging-Based Temperature Sensors. *Materials*, **14**(3).
123. **Lee, C., X. Wei, J. W. Kysar, and J. Hone** (2008). Measurement of the elastic properties and intrinsic strength of monolayer graphene. *Science (New York, N.Y.)*, **321**(5887), 385–388.
124. **Lerf, A., H. He, M. Forster, and J. Klinowski** (1998). Structure of Graphite Oxide Revisited. *The Journal of Physical Chemistry B*, **102**(23), 4477–4482.



125. **Li, H., W. Lu, G. Zhao, B. Song, J. Zhou, W. Dong, and G. Han** (2020). Silver ion-doped cdte quantum dots as fluorescent probe for hg 2+ detection. *RSC Advances*, **10**(64), 38965–38973.
126. **Li, H., Y. Zhang, X. Wang, D. Xiong, and Y. Bai** (2007). Calixarene capped quantum dots as luminescent probes for Hg2+ ions. *Materials Letters*, **61**(7), 1474–1477.
127. **Li, J. and J.-J. Zhu** (2013). Quantum dots for fluorescent biosensing and bio-imaging applications. *The Analyst*, **138**(9), 2506.
128. **Li, J.-L., X.-L. Hou, H.-C. Bao, L. Sun, B. Tang, J.-F. Wang, X.-G. Wang, and M. Gu** (2014). Graphene oxide nanoparticles for enhanced photothermal cancer cell therapy under the irradiation of a femtosecond laser beam: Photothermal Cancer Cell Therapy. *Journal of Biomedical Materials Research Part A*, **102**(7), 2181–2188.
129. **Li, Q., Q. Wei, L. Xie, C. Chen, C. Lu, F.-Y. Su, and P. Zhou** (2016). Layered nio/reduced graphene oxide composites by heterogeneous assembly with enhanced performance as high-performance asymmetric supercapacitor cathode. *RSC advances*, **6**(52), 46548–46557.
130. **Li, X., C. Hao, B. Tang, Y. Wang, M. Liu, Y. Wang, Y. Zhu, C. Lu, and Z. Tang** (2017a). Supercapacitor electrode materials with hierarchically structured pores from carbonization of mwcnts and zif-8 composites. *Nanoscale*, **9**(6), 2178–2187.
131. **Li, X., J. Li, Y. Zhang, and P. Zhao** (2021). Synthesis of ni-mof derived nio/rgo composites as novel electrode materials for high performance supercapacitors. *Colloids and Surfaces A: Physicochemical and Engineering Aspects*, **622**, 126653.
132. **Li, X., L. Tao, Z. Chen, H. Fang, X. Li, X. Wang, J.-B. Xu, and H. Zhu** (2017b). Graphene and related two-dimensional materials: Structure-property relationships for electronics and optoelectronics. *Applied Physics Reviews*, **4**(2), 021306.
133. **Li, X., G. Wang, X. Ding, Y. Chen, Y. Gou, and Y. Lu** (2013). A turn-on fluorescent sensor for detection of Pb2+ based on graphene oxide and G-quadruplex DNA. *Physical Chemistry Chemical Physics*, **15**(31), 12800–.
134. **Li, Z., W. Zhang, Y. Liu, J. Guo, and B. Yang** (2018). 2d nickel oxide nanosheets with highly porous structure for high performance capacitive energy storage. *Journal of Physics D: Applied Physics*, **51**(4), 045302.
135. **Liu, L., L. Ding, X. Wu, F. Deng, R. Kang, and X. Luo** (2016). Enhancing the Hg(II) Removal Efficiency from Real Wastewater by Novel Thymine-Grafted Reduced Graphene Oxide Complexes. *Industrial & Engineering Chemistry Research*, **55**(24), 6845–6853.
136. **Liu, M., Jinand Notarianni, G. Will, V. T. Tiong, H. Wang, and N. Motta** (2013). Electrochemically exfoliated graphene for electrode films: effect of graphene flake thickness on the sheet resistance and capacitive properties. *Langmuir: the ACS journal of surfaces and colloids*, **29**(43), 13307–13314.

137. **Liu, Q., J. Sun, K. Gao, N. Chen, X. Sun, D. Ti, C. Bai, R. Cui, and L. Qu** (2020a). Graphene quantum dots for energy storage and conversion: from fabrication to applications. *Materials Chemistry Frontiers*, **4**(2), 421–436.
138. **Liu, T., L. Zhang, B. Cheng, X. Hu, and J. Yu** (2020b). Holey graphene for electrochemical energy storage. *Cell Reports Physical Science*, **1**(10), 100215.
139. **Liu, Y. and D. Y. Kim** (2015). Ultraviolet and blue emitting graphene quantum dots synthesized from carbon nano-onions and their comparison for metal ion sensing. *Chemical Communications*, **51**(20), 4176–4179.
140. **Liu, Y., W. Q. Loh, A. Ananthanarayanan, C. Yang, P. Chen, and C. Xu** (2014). Fluorescence quenching between unbonded graphene quantum dots and gold nanoparticles upon simple mixing. *RSC Advances*, **4**(67), 35673–35677.
141. **Liu, Y., X. Tang, M. Deng, T. Zhu, L. Edman, and J. Wang** (2021). Hydrophilic AgInZnS quantum dots as a fluorescent turn-on probe for Cd<sup>2+</sup> detection. *Journal of Alloys and Compounds*, **864**, 158109.
142. **Lou, Y., Y. Zhao, J. Chen, and J.-J. Zhu** (2014). Metal ions optical sensing by semiconductor quantum dots. *J. Mater. Chem. C*, **2**(4), 595–613.
143. **Lucchese, M. M., F. Stavale, E. M. Ferreira, C. Vilani, M. V. d. O. Moutinho, R. B. Capaz, C. A. Achete, and A. Jorio** (2010). Quantifying ion-induced defects and Raman relaxation length in graphene. *Carbon*, **48**(5), 1592–1597.
144. **Ma, B., R. D. Rodriguez, A. Ruban, S. Pavlov, and E. Sheremet** (2019a). The correlation between electrical conductivity and second-order Raman modes of laser-reduced graphene oxide. *Physical Chemistry Chemical Physics*, **21**(19), 10125–10134.
145. **Ma, J., M. Zhang, L. Dong, Y. Sun, Y. Su, Z. Xue, and Z. Di** (2019b). Gas sensor based on defective graphene/pristine graphene hybrid towards high sensitivity detection of NO<sub>2</sub>. *AIP Advances*, **9**(7), 075207.
146. **Mahmoud, W. E.** (2012). Functionalized ME-capped CdSe quantum dots based luminescence probe for detection of Ba<sup>2+</sup> ions. *Sensors and Actuators B: Chemical*, **164**(1), 76–81.
147. **Mao, S., H. Pu, and J. Chen** (2012). Graphene oxide and its reduction: modeling and experimental progress. *RSC Advances*, **2**(7), 2643–2662.
148. **Marcano, D. C., D. V. Kosynkin, J. M. Berlin, A. Sinitskii, Z. Sun, A. Slesarev, L. B. Alemany, W. Lu, and J. M. Tour** (2010). Improved synthesis of graphene oxide. *ACS nano*, **4**(8), 4806–4814.
149. **Marina, P. E., G. A. Ali, L. M. See, E. Y. L. Teo, E.-P. Ng, and K. F. Chong** (2019). In situ growth of redox-active iron-centered nanoparticles on graphene sheets for specific capacitance enhancement. *Arabian Journal of Chemistry*, **12**(8), 3883–3889.

150. **Marrani, A. G., V. Novelli, S. Sheehan, D. P. Dowling, and D. Dini** (2014). Probing the redox states at the surface of electroactive nanoporous nio thin films. *ACS applied materials & interfaces*, **6**(1), 143–152.
151. **Martins Ferreira, E. H., M. V. O. Moutinho, F. Stavale, M. M. Lucchese, R. B. Capaz, C. A. Achete, and A. Jorio** (2010). Evolution of the Raman spectra from single-, few-, and many-layer graphene with increasing disorder. *Physical Review B*, **82**(12), 125429. Publisher: American Physical Society.
152. **McAllister, M. J., J.-L. Li, D. H. Adamson, H. C. Schniepp, A. A. Abdala, J. Liu, M. Herrera-Alonso, D. L. Milius, R. Car, R. K. Prud'homme, and I. A. Aksay** (2007). Single Sheet Functionalized Graphene by Oxidation and Thermal Expansion of Graphite. *Chemistry of Materials*, **19**(18), 4396–4404.
153. **Meyer, J. C., C. Kisielowski, R. Erni, M. D. Rossell, M. Crommie, and A. Zettl** (2008). Direct imaging of lattice atoms and topological defects in graphene membranes. *Nano letters*, **8**(11), 3582–3586.
154. **Miniach, E. and G. Gryglewicz** (2018). Solvent-controlled morphology of bismuth sulfide for supercapacitor applications. *Journal of Materials Science*, **53**(24), 16511–16523.
155. **Muchharla, B., T. Narayanan, K. Balakrishnan, P. M. Ajayan, and S. Talapatra** (2014). Temperature dependent electrical transport of disordered reduced graphene oxide. *2D Materials*, **1**(1), 011008.
156. **Mungse, H. P. and O. P. Khatri** (2014). Chemically functionalized reduced graphene oxide as a novel material for reduction of friction and wear. *The Journal of Physical Chemistry C*, **118**(26), 14394–14402.
157. **Munief, W.-M., X. Lu, T. Teucke, J. Wilhelm, A. Britz, F. Hempel, R. Lanche, M. Schwartz, J. K. Y. Law, S. Grandthyll, F. Müller, J.-U. Neurohr, K. Jacobs, M. Schmitt, V. Pachauri, R. Hempelmann, and S. Ingebrandt** (2019). Reduced graphene oxide biosensor platform for the detection of NT-proBNP biomarker in its clinical range. *Biosensors and Bioelectronics*, **126**, 136–142.
158. **Murugadoss, V., J. Lin, H. Liu, X. Mai, T. Ding, Z. Guo, and S. Angaiah** (2019). Optimizing graphene content in a nise/graphene nanohybrid counter electrode to enhance the photovoltaic performance of dye-sensitized solar cells. *Nanoscale*, **11**(38), 17579–17589.
159. **Nagamuthu, S. and K.-S. Ryu** (2019). Synthesis of ag/nio honeycomb structured nanoarrays as the electrode material for high performance asymmetric supercapacitor devices. *Scientific reports*, **9**(1), 1–11.
160. **Naksen, P., S. Boonruang, N. Yuenyong, H. L. Lee, P. Ramachandran, W. Anutrasakda, M. Amatongchai, S. Pancharee, and P. Jarujamrus** (2022). Sensitive detection of trace level cd (ii) triggered by chelation enhanced fluorescence (chef)turn on: Nitrogen-doped graphene quantum dots (n-gqds) as fluorometric paper-based sensor. *Talanta*, **242**, 123305.

161. **Nandanapalli, K. R., D. Mudusu, and S. Lee** (2019). Functionalization of graphene layers and advancements in device applications. *Carbon*, **152**, 954–985.
162. **Niu, X., Y. Zhong, R. Chen, F. Wang, Y. Liu, and D. Luo** (2018). A turn-on fluorescence sensor for Pb<sup>2+</sup> detection based on graphene quantum dots and gold nanoparticles. *Sensors and Actuators B: Chemical*, **255**, 1577–1581.
163. **Nolan, E. M. and S. J. Lippard** (2008). Tools and Tactics for the Optical Detection of Mercuric Ion. *Chemical Reviews*, **108**(9), 3443–3480.
164. **Novoselov, K. S., A. K. Geim, S. V. Morozov, D. Jiang, Y. Zhang, S. V. Dubonos, I. V. Grigorieva, and A. A. Firsov** (2004). Electric field effect in atomically thin carbon films. *Science (New York, N.Y.)*, **306**(5696), 666–669.
165. **Novoselov, K. S., Z. Jiang, Y. Zhang, S. Morozov, H. L. Stormer, U. Zeitler, J. Maan, G. Boebinger, P. Kim, and A. K. Geim** (2007). Room-temperature quantum hall effect in graphene. *Science*, **315**(5817), 1379–1379.
166. **Okhay, O., G. Gonçalves, A. Tkach, C. Dias, J. Ventura, M. F. Ribeiro da Silva, L. M. Valente Gonçalves, and E. Titus** (2016). Thin film versus paper-like reduced graphene oxide: Comparative study of structural, electrical, and thermoelectrical properties. *Journal of Applied Physics*, **120**(5), 051706.
167. **Pan, D., J. Zhang, Z. Li, and M. Wu** (2010). Hydrothermal route for cutting graphene sheets into blue-luminescent graphene quantum dots. *Advanced Materials (Deerfield Beach, Fla.)*, **22**(6), 734–738.
168. **Paul, R., N. Humblot, S. E. Steinvall, E. Z. Stutz, S. S. Joglekar, J.-B. Leran, M. Zamani, C. Cayron, R. Loge, A. G. del Aguila, et al.** (2020). van der waals epitaxy of earth-abundant zn<sub>3</sub>p<sub>2</sub> on graphene for photovoltaics. *Crystal Growth & Design*, **20**(6), 3816–3825.
169. **Peres, N. M. R., F. Guinea, and A. H. Castro Neto** (2006). Electronic properties of disordered two-dimensional carbon. *Physical Review B*, **73**(12), 125411.
170. **Pham, V. P., A. Mishra, and G. Y. Yeom** (2017). The enhancement of Hall mobility and conductivity of CVD graphene through radical doping and vacuum annealing. *RSC Advances*, **7**(26), 16104–16108.
171. **Pimenta, M., G. Dresselhaus, M. S. Dresselhaus, L. Cancado, A. Jorio, and R. Saito** (2007). Studying disorder in graphite-based systems by raman spectroscopy. *Physical chemistry chemical physics*, **9**(11), 1276–1290.
172. **Puah, P. Y., P. Y. Moh, P. C. Lee, and S. E. How** (2018). Spin-coated graphene oxide as a biomaterial for Whartons Jelly derived mesenchymal stem cell growth: a preliminary study. *Materials Technology*, **33**(13), 835–843.
173. **Qian, L., A. R. Thiruppathi, J. van der Zalm, and A. Chen** (2021). Graphene oxide-based nanomaterials for the electrochemical sensing of isoniazid. *ACS Applied Nano Materials*, **4**(4), 3696–3706.

174. **Qian, Z. S., X. Y. Shan, L. J. Chai, J. R. Chen, and H. Feng** (2015). A fluorescent nanosensor based on graphene quantum dots aptamer probe and graphene oxide platform for detection of lead (II) ion. *Biosensors and Bioelectronics*, **68**, 225–231.
175. **Qian, Z. S., X. Y. Shan, L. J. Chai, J. J. Ma, J. R. Chen, and H. Feng** (2014). A universal fluorescence sensing strategy based on biocompatible graphene quantum dots and graphene oxide for the detection of DNA. *Nanoscale*, **6**(11), 5671–5674.
176. **Qin, H., V. Sorkin, Q.-X. Pei, Y. Liu, and Y.-W. Zhang** (2020). Failure in two-dimensional materials: Defect sensitivity and failure criteria. *Journal of Applied Mechanics*, **87**(3), 030802.
177. **Qiu, Y., F. Collin, R. H. Hurt, and I. Külaots** (2016). Thermochemistry and kinetics of graphite oxide exothermic decomposition for safety in large-scale storage and processing. *Carbon*, **96**, 20–28.
178. **Quezada-Renteria, J. A., C. O. Ania, L. F. Chazaro-Ruiz, and J. R. Rangel-Mendez** (2019). Influence of protons on reduction degree and defect formation in electrochemically reduced graphene oxide. *Carbon*, **149**, 722–732.
179. **Rakesh Kumar, T., C. Shilpa Chakra, S. Madhuri, E. Sai Ram, and K. Ravi** (2021). Microwave-irradiated novel mesoporous nickel oxide carbon nanocomposite electrodes for supercapacitor application. *Journal of Materials Science: Materials in Electronics*, **32**(15), 20374–20383.
180. **Ramesh, S., K. Karuppasamy, H.-S. Kim, H. S. Kim, and J.-H. Kim** (2018). Hierarchical flowerlike 3d nanostructure of  $\text{Co}_3\text{O}_4@ \text{MnO}_2/\text{n-doped graphene oxide (NGO)}$  hybrid composite for a high-performance supercapacitor. *Scientific reports*, **8**(1), 1–11.
181. **Ramesh, S., H. Yadav, Y.-J. Lee, G.-W. Hong, A. Kathalingam, A. Sivasamy, H.-S. Kim, H. S. Kim, and J.-H. Kim** (2019). Porous materials of nitrogen doped graphene oxide@  $\text{SnO}_2$  electrode for capable supercapacitor application. *Scientific Reports*, **9**(1), 1–10.
182. **Ramu, A., A. Umar, A. A. Ibrahim, H. Algadi, Y. S. Ibrahim, Y. Wang, M. M. Hanafiah, P. Shanmugam, and D. Choi** (2021). Synthesis of porous 2d layered nickel oxide-reduced graphene oxide (NIO-rGO) hybrid composite for the efficient electrochemical detection of epinephrine in biological fluid. *Environmental Research*, **200**, 111366.
183. **Rezvani Moghaddam, A., M. Kamkar, Z. Ranjbar, U. Sundararaj, A. Jannesari, and B. Ranjbar** (2019). Tuning the Network Structure of Graphene/Epoxy Nanocomposites by Controlling Edge/Basal Localization of Functional Groups. *Industrial & Engineering Chemistry Research*, **58**(47), 21431–21440.
184. **Ribeiro-Soares, J., M. E. Oliveros, C. Garin, M. V. David, L. G. P. Martins, C. A. Almeida, E. H. Martins-Ferreira, K. Takai, T. Enoki, R. Magalhães-Paniago, A. Malachias, A. Jorio, B. S. Archanjo, C. A. Achete, and L. G. Cançado** (2015). Structural analysis of polycrystalline graphene systems by Raman spectroscopy. *Carbon*, **95**, 646–652.

185. **Ryu, S., L. Liu, S. Berciaud, Y.-J. Yu, H. Liu, P. Kim, G. W. Flynn, and L. E. Brus** (2010). Atmospheric Oxygen Binding and Hole Doping in Deformed Graphene on a SiO<sub>2</sub> Substrate. *Nano Letters*, **10**(12), 4944–4951.
186. **Sachdeva, H.** (2020). Recent advances in the catalytic applications of GO/rGO for green organic synthesis. *Green Processing and Synthesis*, **9**(1).
187. **Sadezky, A., H. Muckenhuber, H. Grothe, R. Niessner, and U. Pöschl** (2005). Raman microspectroscopy of soot and related carbonaceous materials: Spectral analysis and structural information. *Carbon*, **43**(8), 1731–1742.
188. **Sang, M., J. Shin, K. Kim, and K. J. Yu** (2019). Electronic and thermal properties of graphene and recent advances in graphene based electronics applications. *Nanomaterials*, **9**(3), 374.
189. **Savchak, M., N. Borodinov, R. Burtovyy, M. Anayee, K. Hu, R. Ma, A. Grant, H. Li, D. B. Cutshall, Y. Wen, G. Koley, W. R. Harrell, G. Chumanov, V. Tsukruk, and I. Luzinov** (2018). Highly Conductive and Transparent Reduced Graphene Oxide Nanoscale Films via Thermal Conversion of Polymer-Encapsulated Graphene Oxide Sheets. *ACS applied materials & interfaces*, **10**(4), 3975–3985.
190. **Scharfenberg, S., D. Z. Rocklin, C. Chialvo, R. L. Weaver, P. M. Goldbart, and N. Mason** (2011). Probing the mechanical properties of graphene using a corrugated elastic substrate. *Applied Physics Letters*, **98**(9), 091908.
191. **Schniepp, H. C., J.-L. Li, M. J. McAllister, H. Sai, M. Herrera-Alonso, D. H. Adamson, R. K. Prud'homme, R. Car, D. A. Saville, and I. A. Aksay** (2006). Functionalized single graphene sheets derived from splitting graphite oxide. *The journal of physical chemistry B*, **110**(17), 8535–8539.
192. **Schweizer, P., C. Dolle, and E. Spiecker** (2018). In situ manipulation and switching of dislocations in bilayer graphene. *Science advances*, **4**(8), eaat4712.
193. **Schwierz, F.** (2010). Graphene transistors. *Nature nanotechnology*, **5**(7), 487–496.
194. **Sengupta, I., S. Chakraborty, M. Talukdar, S. K. Pal, and S. Chakraborty** (2018). Thermal reduction of graphene oxide: How temperature influences purity. *Journal of Materials Research*, **33**(23), 4113–4122.
195. **Seonwoo, H., H.-W. Choung, S. Park, K. S. Choi, K.-J. Jang, J. Kim, K.-T. Lim, Y. Kim, P. Garg, S. Pandey, et al.** (2022). Reduced graphene oxide-incorporated calcium phosphate cements with pulsed electromagnetic fields for bone regeneration. *RSC advances*, **12**(9), 5557–5570.
196. **Sethi, M., U. S. Shenoy, and D. K. Bhat** (2021). Simple solvothermal synthesis of porous graphene-nio nanocomposites with high cyclic stability for supercapacitor application. *Journal of Alloys and Compounds*, **854**, 157190.
197. **Shao, G., Y. Lu, F. Wu, C. Yang, F. Zeng, and Q. Wu** (2012). Graphene oxide: the mechanisms of oxidation and exfoliation. *Journal of materials science*, **47**(10), 4400–4409.

198. **Sharma, N., M. Arif, S. Monga, M. Shkir, Y. K. Mishra, and A. Singh** (2020). Investigation of bandgap alteration in graphene oxide with different reduction routes. *Applied Surface Science*, **513**, 145396.
199. **Sharma, N., V. Sharma, Y. Jain, M. Kumari, R. Gupta, S. K. Sharma, and K. Sachdev** (2017). Synthesis and Characterization of Graphene Oxide (GO) and Reduced Graphene Oxide (rGO) for Gas Sensing Application. *Macromolecular Symposia*, **376**(1), 1700006.
200. **Shen, B., D. Lu, W. Zhai, and W. Zheng** (2013a). Synthesis of graphene by low-temperature exfoliation and reduction of graphite oxide under ambient atmosphere. *Journal of Materials Chemistry C*, **1**(1), 50–53.
201. **Shen, J., Y. Zhu, X. Yang, and C. Li** (2012). Graphene quantum dots: emergent nanolights for bioimaging, sensors, catalysis and photovoltaic devices. *Chemical Communications (Cambridge, England)*, **48**(31), 3686–3699.
202. **Shen, Y., S. Yang, P. Zhou, Q. Sun, P. Wang, L. Wan, J. Li, L. Chen, X. Wang, S. Ding, and D. W. Zhang** (2013b). Evolution of the band-gap and optical properties of graphene oxide with controllable reduction level. *Carbon*, **62**, 157–164.
203. **Shi, F., Y. Zhang, W. Na, X. Zhang, Y. Li, and X. Su** (2016). Graphene quantum dots as selective fluorescence sensor for the detection of ascorbic acid and acid phosphatase via Cr(VI)/Cr(III)-modulated redox reaction. *Journal of Materials Chemistry B*, **4**(19), 3278–3285.
204. **Shi, H. H., S. Jang, and H. E. Naguib** (2019). Freestanding Laser-Assisted Reduced Graphene Oxide Microribbon Textile Electrode Fabricated on a Liquid Surface for Supercapacitors and Breath Sensors. *ACS Applied Materials & Interfaces*, **11**(30), 27183–27191.
205. **Shteplyuk, I., N. M. Caffrey, T. Iakimov, V. Khranovskyy, I. A. Abrikosov, and R. Yakimova** (2017). On the interaction of toxic heavy metals (cd, hg, pb) with graphene quantum dots and infinite graphene. *Scientific reports*, **7**(1), 1–17.
206. **Silipigni, L., G. Salvato, G. Di Marco, B. Fazio, A. Torrisi, M. Cutroneo, and L. Torrisi** (2019). Band-like transport in high vacuum thermal reduced graphene oxide films. *Vacuum*, **165**, 254–261.
207. **Sinclair, R. C. and P. V. Coveney** (2019). Modeling Nanostructure in Graphene Oxide: Inhomogeneity and the Percolation Threshold. *Journal of Chemical Information and Modeling*, **59**(6), 2741–2745.
208. **Singh, A., N. Sharma, M. Arif, and R. S. Katiyar** (2019). Electrically reduced graphene oxide for photovoltaic application. *Journal of Materials Research*, **34**(4), 652–660.
209. **Slobodian, O. M., P. M. Lytvyn, A. S. Nikolenko, V. M. Naseka, O. Y. Khyzhun, A. V. Vasin, S. V. Sevostianov, and A. N. Nazarov** (2018). Low-Temperature Reduction of Graphene Oxide: Electrical Conductance and Scanning Kelvin Probe Force Microscopy. *Nanoscale Research Letters*, **13**(1), 139.

210. **Smith, A. T., A. M. LaChance, S. Zeng, B. Liu, and L. Sun** (2019). Synthesis, properties, and applications of graphene oxide/reduced graphene oxide and their nanocomposites. *Nano Materials Science*, **1**(1), 31–47.
211. **Song, H., X. Zhang, Y. Liu, and Z. Su** (2019). Developing graphene-based nanohybrids for electrochemical sensing. *The Chemical Record*, **19**(2-3), 534–549.
212. **Soni, M., P. Kumar, J. Pandey, S. K. Sharma, and A. Soni** (2018). Scalable and site specific functionalization of reduced graphene oxide for circuit elements and flexible electronics. *Carbon*, **128**, 172–178.
213. **Sood, A. K., R. Gupta, and S. A. Asher** (2001). Origin of the unusual dependence of Raman D band on excitation wavelength in graphite-like materials. *Journal of Applied Physics*, **90**(9), 4494–4497.
214. **Souza, A. P. R. d., C. W. Foster, A. V. Kollopoulos, M. Bertotti, and C. E. Banks** (2015). Screen-printed back-to-back electroanalytical sensors: heavy metal ion sensing. *Analyst*, **140**(12), 4130–4136.
215. **Staudenmaier, L.** (1898). Procedure for representing the graphite acid. *Reports of the German Chemical Society*, **31**(2), 1481–1487.
216. **Sun, H., N. Gao, L. Wu, J. Ren, W. Wei, and X. Qu** (2013a). Highly Photoluminescent Amino-Functionalized Graphene Quantum Dots Used for Sensing Copper Ions. *Chemistry - A European Journal*, **19**(40), 13362–13368.
217. **Sun, H., L. Wu, W. Wei, and X. Qu** (2013b). Recent advances in graphene quantum dots for sensing. *Materials Today*, **16**(11), 433–442.
218. **Sun, X., Z. Liu, K. Welsher, J. T. Robinson, A. Goodwin, S. Zaric, and H. Dai** (2008). Nano-graphene oxide for cellular imaging and drug delivery. *Nano Research*, **1**(3), 203–212.
219. **Sylla, N. F., N. M. Ndiaye, B. Ngom, D. Momodu, M. Madito, B. Mutuma, and N. Manyala** (2019). Effect of porosity enhancing agents on the electrochemical performance of high-energy ultracapacitor electrodes derived from peanut shell waste. *Scientific reports*, **9**(1), 1–15.
220. **T., A., P. J., D. K. Pathak, K. Saxena, R. Kumar, and V. Kumar** (2021). Porous graphene network from graphene oxide: Facile self-assembly and temperature dependent structural evolution. *Materials Today Communications*, **26**, 101930.
221. **Tadyszak, K., J. K. Wychowaniec, and J. Litowczenko** (2018). Biomedical applications of graphene-based structures. *Nanomaterials*, **8**(11), 944.
222. **Tam, T. V., S. H. Hur, J. S. Chung, and W. M. Choi** (2021). Novel paper- and fiber optic-based fluorescent sensor for glucose detection using aniline-functionalized graphene quantum dots. *Sensors and Actuators B: Chemical*, **329**, 129250.
223. **Tang, B., H. Guoxin, and H. Gao** (2010). Raman Spectroscopic Characterization of Graphene. *Applied Spectroscopy Reviews*, **45**(5), 369–407.



224. **Tang, Q., Z. Zhou, and Z. Chen** (2013). Graphene-related nanomaterials: tuning properties by functionalization. *Nanoscale*, **5**(11), 4541–4583.
225. **Tegou, E., G. Pseiropoulos, M. K. Filippidou, and S. Chatzandroulis** (2016). Low-temperature thermal reduction of graphene oxide films in ambient atmosphere: Infra-red spectroscopic studies and gas sensing applications. *Microelectronic Engineering*, **159**, 146–150.
226. **Thangamuthu, M., K. Y. Hsieh, P. V. Kumar, and G.-Y. Chen** (2019). Graphene-and graphene oxide-based nanocomposite platforms for electrochemical biosensing applications. *International journal of molecular sciences*, **20**(12), 2975.
227. **Tian, W., W. Li, W. Yu, and X. Liu** (2017). A Review on Lattice Defects in Graphene: Types, Generation, Effects and Regulation. *Micromachines*, **8**(5), 163.
228. **Tian, Y., Z. Yu, L. Cao, X. L. Zhang, C. Sun, and D.-W. Wang** (2021). Graphene oxide: An emerging electromaterial for energy storage and conversion. *Journal of Energy Chemistry*, **55**, 323–344.
229. **Ting, S. L., S. J. Ee, A. Ananthanarayanan, K. C. Leong, and P. Chen** (2015). Graphene quantum dots functionalized gold nanoparticles for sensitive electrochemical detection of heavy metal ions. *Electrochimica Acta*, **172**, 7–11.
230. **Tu, N. D. K., J. Choi, C. R. Park, and H. Kim** (2015). Remarkable Conversion Between n- and p-Type Reduced Graphene Oxide on Varying the Thermal Annealing Temperature. *Chemistry of Materials*, **27**(21), 7362–7369.
231. **Tuinstra, F. and J. L. Koenig** (1970). Raman spectrum of graphite. *The Journal of chemical physics*, **53**(3), 1126–1130.
232. **Venkataprasanna, K. S., J. Prakash, S. Vignesh, G. Bharath, M. Venkatesan, F. Banat, S. Sahabudeen, S. Ramachandran, and G. Devanand Venkatasubbu** (2020). Fabrication of Chitosan/PVA/GO/CuO patch for potential wound healing application. **143**, 744–762.
233. **Vidano, R. and D. B. Fischbach** (1978). New lines in the raman spectra of carbons and graphite. *Journal of the American Ceramic Society*, **61**(1-2), 13–17.
234. **Vlad, A., N. Singh, S. Melinte, J.-F. Gohy, and P. Ajayan** (2016). Carbon redox-polymer-gel hybrid supercapacitors. *Scientific Reports*, **6**(1), 1–6.
235. **Voiry, D., J. Yang, J. Kupferberg, R. Fullon, C. Lee, H. Y. Jeong, H. S. Shin, and M. Chhowalla** (2016). High-quality graphene via microwave reduction of solution-exfoliated graphene oxide. *Science*, **353**(6306), 1413–1416.
236. **Vollebregt, S., R. Ishihara, F. D. Tichelaar, Y. Hou, and C. I. M. Beenakker** (2012). Influence of the growth temperature on the first and second-order Raman band ratios and widths of carbon nanotubes and fibers. *Carbon*, **50**(10), 3542–3554.

237. **Wang, B.** and **M.-L. Bocquet** (2011). Monolayer graphene and h-bn on metal substrates as versatile templates for metallic nanoclusters. *The Journal of Physical Chemistry Letters*, **2**(18), 2341–2345.
238. **Wang, C., Y. Sun, J. Jin, Z. Xiong, D. Li, J. Yao, and Y. Liu** (2018a). Highly selective, rapid-functioning and sensitive fluorescent test paper based on graphene quantum dots for on-line detection of metal ions. *Analytical Methods*, **10**(10), 1163–1171.
239. **Wang, D.-Y., D.-W. Wang, H.-A. Chen, T.-R. Chen, S.-S. Li, Y.-C. Yeh, T.-R. Kuo, J.-H. Liao, Y.-C. Chang, W.-T. Chen, S.-H. Wu, C.-C. Hu, C.-W. Chen, and C.-C. Chen** (2015). Photoluminescence quenching of graphene oxide by metal ions in aqueous media. *Carbon*, **82**, 24–30.
240. **Wang, F., Z. Gu, W. Lei, W. Wang, X. Xia, and Q. Hao** (2014). Graphene quantum dots as a fluorescent sensing platform for highly efficient detection of copper (ii) ions. *Sensors and Actuators B: Chemical*, **190**, 516–522.
241. **Wang, Y., Y. Chen, S. D. Lacey, L. Xu, H. Xie, T. Li, V. A. Danner, and L. Hu** (2018b). Reduced graphene oxide film with record-high conductivity and mobility. *Materials Today*, **21**(2), 186–192. ISSN 1369-7021.
242. **Wang, Y., M. Yang, W. Liu, L. Dong, D. Chen, and C. Peng** (2019). Gas sensors based on assembled porous graphene multilayer frameworks for DMMP detection. *Journal of Materials Chemistry C*, **7**(30), 9248–9256.
243. **Wei, N., L. Yu, Z. Sun, Y. Song, M. Wang, Z. Tian, Y. Xia, J. Cai, Y.-y. Li, L. Zhao, et al.** (2019). Scalable salt-templated synthesis of nitrogen-doped graphene nanosheets toward printable energy storage. *ACS nano*, **13**(7), 7517–7526.
244. **Wei, Z., D. Wang, S. Kim, S.-Y. Kim, Y. Hu, M. K. Yakes, A. R. Laracuente, Z. Dai, S. R. Marder, C. Berger, W. P. King, W. A. de Heer, P. E. Sheehan, and E. Riedo** (2010a). Nanoscale tunable reduction of graphene oxide for graphene electronics. *Science (New York, N.Y.)*, **328**(5984), 1373–1376.
245. **Wei, Z., D. Wang, S. Kim, S.-Y. Kim, Y. Hu, M. K. Yakes, A. R. Laracuente, Z. Dai, S. R. Marder, C. Berger, et al.** (2010b). Nanoscale tunable reduction of graphene oxide for graphene electronics. *Science*, **328**(5984), 1373–1376.
246. **Wen, J., Z. Sun, Y. Qiao, Y. Zhou, Y. Liu, Q. Zhang, Y. Liu, and S. Jiao** (2022). Ti<sub>3</sub>C<sub>2</sub> mxene-reduced graphene oxide composite polymer-based printable electrolyte for quasi-solid-state dye-sensitized solar cells. *ACS Applied Energy Materials*, **5**(3), 3329–3338.
247. **Whitby, R. L. D.** (2014). Chemical Control of Graphene Architecture: Tailoring Shape and Properties. *ACS Nano*, **8**(10), 9733–9754.
248. **Wu, H., J. Liang, and H. Han** (2008). A novel method for the determination of Pb<sup>2+</sup> based on the quenching of the fluorescence of CdTe quantum dots. *Microchimica Acta*, **161**(1-2), 81–86.

249. **Xu, J., L. Wu, Y. Liu, J. Zhang, J. Liu, S. Shu, X. Kang, Q. Song, D. Liu, F. Huang, et al.** (2020). Nio-rgo composite for supercapacitor electrode. *Surfaces and Interfaces*, **18**, 100420.
250. **Xu, X., Z. Zhang, and W. Yao** (2021). Mechanical properties of graphene oxide coupled by multi-physical field: Grain boundaries and functional groups. *Crystals*, **11**(1), 62.
251. **Xu, Y., L. Wang, P. Cao, C. Cai, Y. Fu, and X. Ma** (2016). Mesoporous composite nickel cobalt oxide/graphene oxide synthesized via a template-assistant co-precipitation route as electrode material for supercapacitors. *Journal of Power Sources*, **306**, 742–752.
252. **Yadav, P., A. Banerjee, S. Unni, J. Jog, S. Kurungot, and S. Ogale** (2012). A 3D Hexaporous Carbon Assembled from Single-Layer Graphene as High Performance Supercapacitor. *ChemSusChem*, **5**(11), 2159–2164.
253. **Yadav, S. and I. Kaur** (2016). Low temperature processed graphene thin film transparent electrodes for supercapacitor applications. *RSC Advances*, **6**(82), 78702–78713.
254. **Yalcin, S. E., C. Galande, R. Kappera, H. Yamaguchi, U. Martinez, K. A. Velizhanin, S. K. Doorn, A. M. Dattelbaum, M. Chhowalla, P. M. Ajayan, G. Gupta, and A. D. Mohite** (2015). Direct Imaging of Charge Transport in Progressively Reduced Graphene Oxide Using Electrostatic Force Microscopy. *ACS Nano*, **9**(3), 2981–2988.
255. **Yan, Z., W. Yao, L. Hu, D. Liu, C. Wang, and C.-S. Lee** (2015). Progress in the preparation and application of three-dimensional graphene-based porous nanocomposites. *Nanoscale*, **7**(13), 5563–5577.
256. **Yang, G., L. Li, W. B. Lee, and M. C. Ng** (2018). Structure of graphene and its disorders: a review. *Science and technology of advanced materials*, **19**(1), 613–648.
257. **Yang, H., X. Jin, G. Sun, Z. Li, J. Gao, B. Lu, C. Shao, X. Zhang, C. Dai, Z. Zhang, et al.** (2020). Retarding ostwald ripening to directly cast 3d porous graphene oxide bulks at open ambient conditions. *ACS nano*, **14**(5), 6249–6257.
258. **Yang, P., J. Su, R. Guo, F. Yao, and C. Yuan** (2019). B,N-Co-doped graphene quantum dots as fluorescence sensor for detection of Hg<sup>2+</sup> and F ions. *Analytical Methods*, **11**(14), 1879–1883.
259. **Yi, T. F., T. T. Wei, J. Mei, W. Zhang, Y. Zhu, Y. G. Liu, S. Luo, H. Liu, Y. Lu, and Z. Guo** (2020). Approaching high-performance supercapacitors via enhancing pseudocapacitive nickel oxide-based materials. *Advanced Sustainable Systems*, **4**(3), 1900137.
260. **Yu, W., L. Sisi, Y. Haiyan, and L. Jie** (2020). Progress in the functional modification of graphene/graphene oxide: A review. *RSC Advances*, **10**(26), 15328–15345.
261. **Zeng, W., X.-M. Tao, S. Lin, C. Lee, D. Shi, K.-h. Lam, B. Huang, Q. Wang, and Y. Zhao** (2018). Defect-engineered reduced graphene oxide sheets with high electric

- conductivity and controlled thermal conductivity for soft and flexible wearable thermoelectric generators. *Nano Energy*, **54**, 163–174.
262. **Zeng, Y., T. Li, Y. Yao, T. Li, L. Hu, and A. Marconnet** (2019). Thermally Conductive Reduced Graphene Oxide Thin Films for Extreme Temperature Sensors. *Advanced Functional Materials*, **29**(27), 1901388.
  263. **Zha, X., Z. Wu, Z. Cheng, W. Yang, J. Li, Y. Chen, L. He, E. Zhou, and Y. Yang** (2021). High performance energy storage electrodes based on 3d z-coo/rgo nanostructures for supercapacitor applications. *Energy*, **220**, 119696.
  264. **Zhang, F., F. Liu, C. Wang, X. Xin, J. Liu, S. Guo, and J. Zhang** (2016a). Effect of Lateral Size of Graphene Quantum Dots on Their Properties and Application. *ACS Applied Materials & Interfaces*, **8**(3), 2104–2110.
  265. **Zhang, H. and R. Lv** (2018). Defect engineering of two-dimensional materials for efficient electrocatalysis. *Journal of Materiomics*, **4**(2), 95–107.
  266. **Zhang, H.-B., J.-W. Wang, Q. Yan, W.-G. Zheng, C. Chen, and Z.-Z. Yu** (2011). Vacuum-assisted synthesis of graphene from thermal exfoliation and reduction of graphite oxide. *Journal of Materials Chemistry*, **21**(14), 5392–5397.
  267. **Zhang, J., L. Na, Y. Jiang, D. Lou, and L. Jin** (2016b). Graphene quantum dots as a fluorescence-quenching probe for quantitative analysis of Ponceau 4R solution. *Analytical Methods*, **8**(39), 7242–7246.
  268. **Zhang, L., Z.-Y. Zhang, R.-P. Liang, Y.-H. Li, and J.-D. Qiu** (2014). Boron-Doped Graphene Quantum Dots for Selective Glucose Sensing Based on the Abnormal Aggregation-Induced Photoluminescence Enhancement. *Analytical Chemistry*, **86**(9), 4423–4430.
  269. **Zhang, P., Z. Li, S. Zhang, and G. Shao** (2018). Recent Advances in Effective Reduction of Graphene Oxide for Highly Improved Performance Toward Electrochemical Energy Storage. *Energy & Environmental Materials*, **1**(1), 5–12.
  270. **Zhang, R. and W. Chen** (2014). Nitrogen-doped carbon quantum dots: Facile synthesis and application as a turn-off fluorescent probe for detection of Hg<sup>2+</sup> ions. *Biosensors and Bioelectronics*, **55**, 83–90.
  271. **Zhang, W., Z. Yin, A. Chun, J. Yoo, G. Diao, Y. S. Kim, and Y. Piao** (2016c). Rose rock-shaped nano cu<sub>2</sub>o anchored graphene for high-performance supercapacitors via solvothermal route. *Journal of Power Sources*, **318**, 66–75.
  272. **Zhou, E., C. Wang, X. Deng, and X. Xu** (2016). Ag nanoparticles anchored nio/go composites for enhanced capacitive performance. *Ceramics International*, **42**(11), 12644–12650.
  273. **Zhou, Y., Z. Huang, H. Liao, J. Li, H. Wang, and Y. Wang** (2020). 3d porous graphene/nico<sub>2</sub>o<sub>4</sub> hybrid film as an advanced electrode for supercapacitors. *Applied Surface Science*, **534**, 147598.

274. **Zhou, Y., L. Wen, K. Zhan, Y. Yan, and B. Zhao** (2018). Three-dimensional porous graphene/nickel cobalt mixed oxide composites for high-performance hybrid supercapacitor. *Ceramics International*, **44**(17), 21848–21854.
275. **Zhu, S., J. Zhang, S. Tang, C. Qiao, L. Wang, H. Wang, X. Liu, B. Li, Y. Li, W. Yu, X. Wang, H. Sun, and B. Yang** (2012). Surface Chemistry Routes to Modulate the Photoluminescence of Graphene Quantum Dots: From Fluorescence Mechanism to Up-Conversion Bioimaging Applications. *Advanced Functional Materials*, **22**(22), 4732–4740.
276. **Zhu, X., Z. Zhang, Z. Xue, C. Huang, Y. Shan, C. Liu, X. Qin, W. Yang, X. Chen, and T. Wang** (2017). Understanding the Selective Detection of Fe<sup>3+</sup> Based on Graphene Quantum Dots as Fluorescent Probes: The Ksp of a Metal Hydroxide-Assisted Mechanism. *Analytical Chemistry*, **89**(22), 12054–12058.
277. **Zhuo, Q., J. Tang, J. Sun, and C. Yan** (2018). High Efficient Reduction of Graphene Oxide via Nascent Hydrogen at Room Temperature. *Materials (Basel, Switzerland)*, **11**(3).

## CURRICULUM VITAE

1. **NAME** : T ANUSUYA

2. **DATE OF BIRTH** : 07 01 1984

3. **EDUCATIONAL QUALIFICATIONS**

**2004 Bachelor of Science (B. Sc.)**

Institution : Manonmaniam Sundaranar University

Specialization : Physics

**2007 Master of Science (M. Sc.)**

Institution : Manonmaniam Sundaranar University

Specialization : Physics

**2009 Master of Technology (M. Tech.)**

Institution : Anna University

Specialization : Nanoscience and Technology

**Doctor of Philosophy**

Institution : IIITDM Kancheepuram

Specialization : Physics

Registration Date : 23 July 2018

## **DOCTORAL COMMITTEE**

**CHAIRPERSON** : Dr. Tapas sil  
Associate Professor  
Department of Science and Humanities (Physics)

**GUIDE** : Dr. Vivek Kumar  
Assistant Professor  
Department of Science and Humanities (Physics)

**MEMBERS** : Dr. Anushree P Khandale  
Assistant Professor  
Department of Science and Humanities (Physics)

Dr. Jayachandra Bingi  
Assistant Professor  
School of interdisciplinary design and innovation

Dr. Gowthaman Swaminathan  
Assistant Professor  
Department of Mechanical Engineering